KATHOLIEKE UNIVERSITEIT
LEUVEN

Arenberg Doctoral School of Science, Engineering & Technology
Faculty of Science
Department of Mathematics

Numerical simulations in the afterglow phase of GRBs

Alkiviadis Vlasis

Dissertation presented in partial
fulfillment of the requirements for
the degree of Doctor
in Science

November 2012

Numerical simulations in the afterglow phase of GRBs

Alkiviadis Vlasis

Supervisor:
Prof. dr. R. Keppens
Co-supervisor:
dr. Z. Meliani
(Observatoire de Paris)
Jury:
Prof. dr. S. Poedts, chair
Prof. dr. ir. G. Lapenta
Prof. dr. C. Waelkens
dr. A.J. van Marle
Prof. dr. R.A.M.J. Wijers
(Anton Pannekoek Astronomical Institute)

Dissertation presented in partial fulfillment of the requirements for the degree of Doctor in Science

November 2012

D/2012/10.705/90
ISBN 978-90-8649-573-3

Preface

This book describes a collaborative effort which was made over the course of the last four years in the direction of understanding and explaining some of the physical processes which take place in the most violent events ever recorded in the Universe, the *Gamma-ray bursts* (GRBs). In the introductory chapter I tried, in a very generic way, to introduce all the different physical mechanisms that a reader needs to keep in mind while going through this book. It consists of the scientific research done in previous years from authors the work of which has been an inspiration and a guide through my PhD. The model we propose and the numerical simulations we performed are extensively described throughout chapters 2 to 5.

Carrying out this manuscript has been a long journey, and I would like here to present to the reader the people who helped along the way. Others with their fruitful advice and their scientific expertise and others who honored me with their friendship.

My sincerest gratitude goes to my supervisor, Rony Keppens who gave me the opportunity to work at the highest level in a very competitive group, travel around the world and meet some of the brightest minds in the area of astrophysics. For that and for always being ready to offer his valuable advice and deep knowledge of the field I will always be indebted to him.

Trying to explain the origin of the so called *afterglow* radiation of GRBs has been a very important part of this thesis. Hendrik van Eerten's assistance on understanding the nature of the underlying radiative processes and the numerical schemes which were used in order to describe them was invaluable and I would like here to express my gratitude for his continuous support and contribution to the work described in this book. I thank Prof. dr. R.A.M.J. Wijers for giving me the opportunity to exchange ideas with one of the pioneers in the field of GRBs during the early years of my PhD. His instructive suggestions eminently shaped the presented in this book results.

I owe a great debt of gratitude to Zakaria Meliani. Throughout the last four years he has been not only a great advisor, but also an unlimited source of information, to which I could always refer to when looking for answers. His comprehensive knowledge in the area of computational astrophysics has recently been rewarded with a well deserved position in the Observatory of Paris. But most importantly he has been a friend, and for that I sincerely want to thank him. I am truly indebted to Stefaan Poedts, Giovanni Lapenta, Christoffel Waelkens and Allard Jan van Marle. It was their insightful comments and suggestions during the preparatory work of this thesis which helped increase the overall quality of the scientific outcome.

I am very grateful for the friendly working environment that my colleagues and friends have offered so generously in the past four years in KU Leuven. For that I would like to thank Rémi Monceau-Baroux, Jan Deca, Peter Delmont, Alexander Soenen, Paula Copil, Michaël Moreels, Ed Lee, Maria Elena Innocenti, Andrey Divin, Tom van Doorselaere, Carla Jacobs, Katrien Bonte, Tom Hendrix, Alexander Vapirev, Patrick Antolin, Pierre Henri, Stefano Markidis, Arnaud Beck, Vyacheslav Olshevskyi, Kimberley Steed, Oliver Porth, Anna Lisa Restante, Xia Fang, Ludmila Carone and Soheil Vasheghani Farahani. Special thanks to Josee Pierre, Dominique De Mets and Joelke Vandoren for supervising all the administrative activities that have facilitated the smooth running of the department.

During the past few years I have been honored by the friendship of some people that have become a very important part of my life. Without them this journey would have never been completed and certainly I wouldn't have enjoyed it so much. My gratitude goes to Anouk, Anne, Marco, Claudio, Francesco, Leonardo, Marianna, Luna, Luisa, Joana, Pati, Laetitia, Omid, Elham, Dimitri, Evi, Niko, Christina, Thanasi, Antoni, Christo, Gianni, Katerina and Niko for the wonderful times we had together and for everything we shared.

Last but certainly not least I would like to express my appreciation to my family. Your unconditional love and support has always been and will always be the brightest light on my life's journey.

Alkiviadis Vlasis

Leuven, Belgium
November 2012

Abbreviations

SSA	Synchrotron Self-Absorption
SSC	Synchrotron Self-Compton
MD	molecular dynamics
BM	Blandford & McKee model
HD	Hydrodynamics
MHD	Magnetohydrodynamics
SRHD	Special relativistic hydrodynamics
GRB	Gamma-ray burst
LGRB	Long Gamma-ray burst
SGRB	Short Gamma-ray burst
IC	Inverse Compton scattering
BAT	Burst Alert Telescope
XRT	X-Ray Telescope
SN	Supernova
LAT	Large Area Telescope
NS	Neutron star
BH	Black hole
ST	Sedov-Taylor
AMR	Adaptive Mesh Refinement
MPI	Message Passing Interface
WR	Wolf-Rayet
BATSE	Burst and Transient Source Experiment
CGRO	Compton GRB Observatory
SGR	Soft Gamma Repeater
LAT	Large Aray Telescope
HETE	High-Energy Transient Explorer
NOT	Nordic Optical Telescope
EOS	Equation of state
ISM	Interstellar medium
ALMA	Atacama Large Millimeter Array

CD	Contact Discontinuity
FS	Forward Shock
RS	Reverse Shock
ES	External Shock
KH	Kelvin-Helmholtz
TVD	Total Variation Diminishing
TVDLF	Total Variation Diminishing Lax-Friedrich

List of Symbols

z	Redshift
Z	Metallicity
Γ	Lorentz factor
E_{iso}	Isotropic energy
E_p	Peak energy
θ_h	half opening angle
F	Fluence
σ_T	Thompson cross section
m_e	Electron mass
m_p	Proton mass
c	Speed of light
$\tau_{\gamma\gamma}$	Optical depth
M	Mach number
$M_\odot$	Solar mass
α_ν	Synchrotron self-absorption coefficient
ϵ_E	Fraction of the energy which accelerates the electrons
ϵ_B	Fraction of the energy which generates the magnetic field
j_ν	Emission coefficient
ν_m	Synchrotron peak frequency
ν_c	Cooling frequency
ν_{sa}	Self-absorption frequency
t_{obs}	Observer time
t_e	Emission time
Γ_p	Polytropic index
Γ_{eff}	Effective polytropic index
ω	Rotational frequency
ω_c	Critical rotational frequency
Ω	ω/ω_c
k	Power-law index of the density

Contents

List of Figures

List of Tables

Chapter 1

Introduction

1.1 Gamma-Ray bursts (GRBs)

Gamma-ray bursts (GRBs) are considered by many to be the most puzzling and fascinating events of the Universe. The enormous amount of energy which is released in a short interval, classifies them among the most violent events taking place at the observable Universe. At several events, the estimated amount of energy which is released during the explosion is equivalent to the rest mass energy of the sun being transformed into γ-rays within a few seconds. It is due to the intensity of these explosions that we are able to extract valuable information concerning the surrounding environment of the burst. GRBs are lately associated with the high redshift Universe and progenitors of these events are considered to be collapsing massive stars or a merger between two neutron stars. Hence, apart from the compelling questions arising solely from the event itself, GRBs can very efficiently act as probes in comprehending the high redshift Universe and answer long-lasting questions concerning the chemical evolution of their environment, the host galaxy ambient medium and dust evolution of the Universe. In addition, GRBs are strong candidates for gravitational waves and neutrino observation since they are both theoretically predicted to appear at binary mergers.

The first observational evidence of a GRB was given in the 1960s after the launching of the Vela military satellites. The necessity of reducing the constantly increasing number of nuclear tests during the 50s gave rise to a treaty signed between the US, USSR and Great Britain which banned nuclear testing in the atmosphere, in space and underwater. The Vela satellites, launched by the US

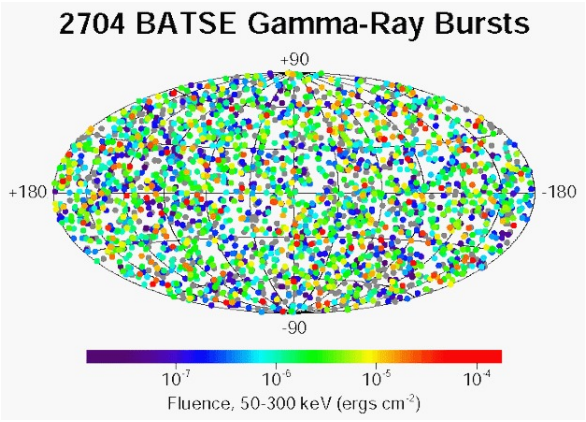

Figure 1.1: Isotropic distribution of GRBs detected from BATSE satellite. Figure courtesy of NASA/SCIENCE PHOTO LIBRARY.

Air Force in 1963, were equipped with x-ray, γ-ray and neutron detectors in order to monitor the compliance of the treaty. On July 2, 1967 Vela 3 and Vela 4 satellites recorded instant flashes of gamma-rays for which a terrestrial or atmospheric origin was immediately ruled out. From July 1969 until July 1972 16 similar bursts were recorded using the space satellites Vela 5 and 6. The results of this mission were published in 1973 in the work entitled "Observations of Gamma-Ray Bursts of cosmic origin" [46] initiating a since then continuously growing scientific interest on GRBs.

After the pioneering work of the Vela satellites, many space missions have been dedicated to the study of GRBs. In 1991 the Compton GRB Observatory (CGRO) was launched carrying on board the Burst and Transient Source Experiment (BATSE), see http://cossc.gsfc.nasa.gov/batse/ and [6] for details on the technical aspects of the mission. Among several exotic astrophysical objects, such as pulsars, black holes, Soft Gamma Repeaters (SGR), the primary objective of BATSE was to conduct full surveys of the sky and record any excess of gamma-rays above the background level. The provided data strongly indicated that the majority of the bursts appear isotropically in the sky (see Fig. 1.1 for a collection of bursts from the BATSE satellite) and originate from distant galaxies [62] and not from the Milky Way, thus increasing enormously the required amount of energy needed to power these events.

In understanding the origin of GRBs and determining their distance in the sky the contribution of the *BeppoSAX* satellite was of great significance [13]. The mission was a collaboration between the Italian Space Agency and the

Netherlands Agency of Aerospace Programs and was launched in the sky in 1997. Named after the Italian physicist Giuseppe "Beppo" Occhialini, the main characteristic of *BeppoSAX* was the wide spectral range, covering from 0.1 to over 200 keV. The breakthrough of the mission came soon after the launching of the satellite with the event of GRB970508. The spectrum of this event revealed high-redshift absorption lines in the optical afterglow, at a redshift of $z = 0.835$, indicating a distance of approximately 6 billion light-years from Earth, thus confirming the cosmological origin of GRBs and providing for the first time an estimated distance of the burst [68]. Furthermore, the simultaneous detection of GRB 980425 by *BeppoSAX* [105] and supernova SN 1998bw [112] provided the first observational link between these two phenomena. In 2003, the detection of GRB 030329 and the spectroscopic discovery of the associated supernova SN 2003dh from NASA's High-Energy Transient Explorer satellite *HETE-2* [19] provided the first direct spectroscopic confirmation of a GRB originating from a supernova [108]. The brightness of the burst allowed for extensive optical observations making GRB 030329 one of the best observed GRBs to date. The optical afterglow exhibited significant variation lasting from $1 - 10$ days after the burst indicating for the first time that an energy injection process might be taking place at the position of the external shock long after the burst has ended [9], [41].

Even though many details concerning the formations of GRB are still shrouded in mystery, our understanding on several aspects of them has greatly advanced during the last decades following the launching of the *Swift* satellite mission [31], [8], [77], [73]. Equipped with a panchromatic set of instruments, the *Swift* satellite has allowed for multiwavelength observation of both the prompt and afterglow emission of the burst in great detail. Launched in 2004 and still operational, *Swift* offers a rapid response ($\precsim$ 90 s) to any triggering event, thus providing us with more than 500 GRBs and afterglows so far. It consists of three major instruments, namely the Burst Alert Telescope (BAT), the X-Ray Telescope (XRT) and the Ultraviolet/Optical Telescope (UVOT). BAT is dedicated in detecting the prompt emission of the burst with energy range $15 - 150$ keV and computing its position on the sky with arc-minute positional accuracy. After the prompt emission has ended, follow-up observations from XRT and UVOT provide us with spectra and light curves from the X-ray, ultraviolet and optical afterglow allowing for a concurrent multiwavelength examination of each burst. The contribution of *Swift* in understanding the nature of GRBs has been crucial in many aspects. The discovery and precise positioning of short/hard GRBs in elliptical host galaxies with no longer star formation regions, suggested that this class of GRBs can be produced by a merging event of two neutron stars or a neutron star with a black hole [33], [12]. Moreover, several long/soft GRBs without an associated supernova have been discovered by *Swift* [22]. These events open the door for an unknown so

far third class of GRBs, which challenges the idea of collapsing massive stars and binary mergers being the only progenitors of GRBs and suggesting that the tidal disruption of a star by a black hole would be an ideal way to power a long duration GRB [54].

More recently, in 2008, the Fermi Gamma-ray Space Telescope was launched performing from low Earth orbit gamma-ray observations of the sky [5], [1], [2]. Equipped with the Gamma-ray Burst Monitor (GBM) and the Large Area Telescope (LAT) Fermi provides exceptional sensitivity to gamma-rays in the range between 20 MeV and 300 GeV and has greatly increased the number of high energy detected GRBs. Detected by Fermi telescope, GRB 080916C is the most energetic GRB discovered to date with a redshift $z = 4.35$ [3]. The observed gamma-ray variability together with the redshift measurements suggest a minimum Lorentz factor for the accompanying ultrarelativistic jet of $\Gamma = 1090$, unseen so far in the Universe.

1.2 GRB classification. Short-Long vs TypeI-TypeII

GRBs are isotropically distributed in the sky and present an average redshift of $z = 2.5$ (see review papers [86], [138], [32]). In the post-*Swift* era the continuous discovery of more distant events tends to constantly re-evaluate that number. The diversity and uniqueness of GRBs makes it difficult to sort them in categories. However, after studying the GRB sample collected by Burst And Transient Experiment (BATSE, see fig. 1.1) [7], Kouveliotou et al. managed to identify a classification of GRBs based on two criteria [49]. First, the duration of the burst and second the hardness of the spectrum. In that way, two distinct categories occurred separating short events that last for less than 2 seconds and longer ones that last for more than 2 seconds. At the same time an anti-correlation was observed between duration and hardness of the spectrum. Short lived bursts presented a hard spectrum while the longer ones were softer. This means that the total amount of energy released in the two cases is different suggesting that the physical mechanism behind the origin of the two kind of bursts is also different. Now, short GRBs are assumed to originate from the merger of two neutron stars or the merger of a neutron star with a black hole, while long GRBs are associated with the collapse of the iron core of a massive star before it explodes into a supernova (SN). Nevertheless, both short-hard and long-soft GRBs have isotropic although inhomogeneous spatial distribution.

In the absence of an associated supernova explosion, long GRB 060614 seems to question this classification scheme. As Zhang et al. demonstrate, one

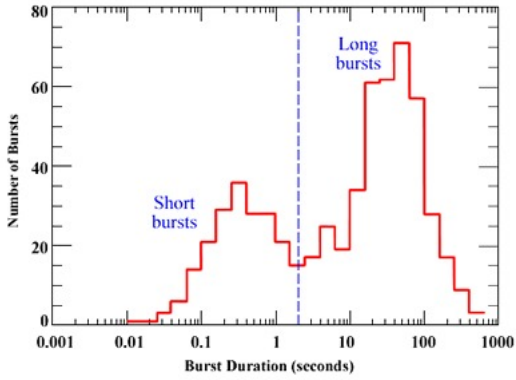

Figure 1.2: Long-short GRB number comparison. Figure courtesy of NASA/BATSE and NASA Gamma-Ray Astronomy group at National Spase Science and Technology Center (NSSTC) (http://gammaray.nsstc.nasa.gov/batse/)

can "construct" a short-hard "pseudoburst" from that long lived event, by only assuming validity of the Amati relation correlating the peak energy of the photons E_p, with the isotropic equivalent of the radiated energy E_{iso} ($E_p \propto E_{iso}^{1/2}$) [141]. Even though the duration of GRB 060614 is longer than 2 s, yet no other distinction separates it from the short-hard bursts suggesting that GRB 060614 is a more intense event from the classical short-hard GRB category. Similarly to the previous classification, Zhang proposes GRBs to be classified analogously to the supernova classification scheme. Therefore, Type I GRBs (similarly to Type Ia SNe) are associated with old stellar populations, are not connected with supernova explosions and most likely originate from compact star mergers. They are short lived bursts and generally present a hard spectrum, although a softer extended tail emission cannot be excluded. Type II GRBs (similar to Type II and Ib/c SNe) are associated with young stellar populations and originate from core collapse massive stars. They are usually long duration bursts and present a softer spectrum than Type I. Their host galaxies are essentially irregular dwarf galaxies.

1.3 GRB-SNe connection

Observations reveal that sometimes core-collapse supernovae (SNe) explosions are followed by long duration GRBs. Recent models (see Yoon et al. 2006 for

a detailed discussion [137]) predict a global GRB/SN ratio of 1/200. The link however between these two extremely violent events was not established until recently. At the early 90s it was a common belief that GRBs did not occur at cosmological distances and they were considered as the merger result between two neutron stars or a neutron star with a black hole occurring in mature galaxies. The energy of the explosion which was inferred from observations, required 10^3 times more energy than a SNe, thus making the link between the two events inconceivable. At the late 90s however, the first GRB redshift calculations revealed the cosmological origin of GRBs and together with corrections in the energy of the explosion due to relativistic effects shifted the scientific interest for the birth of GRBs towards the star forming regions of younger galaxies [81], [128]. The first step towards the GRB-SNe connection had been made.

Details concerning the progenitor of the burst are revealed after studying the host galaxies of GRBs. High resolution spectroscopy of bright afterglows gives in detail the metallicity of the GRB host galaxies. Studying the host galaxies of GRB 970508 and GRB 970828, Pazcynski [81] provided a connection between long GRBs and star-forming regions thus excluding the possibility of them being a result of merging neutron stars. Bloom et al. [11] verified that assumption by determining the observed offset distribution of 20 GRBs. The result was that they were incompatible with the offsets predicted by NS-NS (neutron star - neutron star) and NS-BH (neutron star - black hole) binary models and consistent with those predicted by the collapsar class. At the same time evidence arose that long duration GRBs are far more concentrated in the brightest regions of host galaxies than are the core-collapse supernovae [27]. This indicates that long GRBs should be associated with the most violent explosive events following the death of massive stars and restricted to low metallicity environments. Evidence suggest however that this may not always be the case. By performing spectroscopic observations and metallicity diagnostics for GRB 020819 Levesque et al. [53] demonstrated that this burst did not occur in a low metallicity region of the spiral host but the progenitor evolved in a rather chemically enriched environment of super-solar metallicity.

By now it is widely accepted that long GRB host galaxies share some common characteristics. More precisely long GRBs are usually found in low metallicity bright regions of faint irregular galaxies which are associated with concentrated populations of young massive stars (Wainwright et al 2007).

Though all long GRBs are accompanied by SNe not all SNe can create long GRBs. The collapsar model as introduced by MacFadyen and Woosley [57] provides us with the link between these violent events.

1.4 Prompt emission

The bright gamma-ray excess observed in the light curve is often referred to as the prompt emission of a GRB. It lasts for several seconds and it is characterised by intense time variability. It is nowadays widely accepted that a mechanism of rapid energy dissipation is responsible for the production of the gamma rays during that phase of the burst. The main theoretical challenge is to find the mechanism which converts, with high efficiency, the initial energy of the ejecta into gamma-rays. Although several models have been proposed this mechanism has not yet been identified.

The external collision hypothesis, suggests that the interaction of the external shock with the surrounding matter could be responsible for the prompt emission. Rees and Meszaros [89] suggested a model according to which a relativistic fireball with Lorentz factor $\Gamma \sim 10^3$ while decelerating in a typical extragalactic medium, can dissipate its energy into highly energetic photons of energy comparable to the initial ejecta ($\sim 10^{51}$ erg). They calculated the observed timescale of such an event and showed that it would be of the order of seconds as required from observations. Despite the success of this model in explaining two major difficulties of that time, the recovery of the kinetic energy of the expansion and the theoretical prediction of the observed timescale of the emission, the rapid variability of the prompt phase and the high Lorentz factor needed, argued against that idea. As Sari & Piran demonstrated such a variability can only be produced if an extremely narrow GRB jet of angular opening $\preceq 10^{-4}$ is taken into account, or if the emitting region is restricted to a very small percentage of the external shock and at the same time the jet is radiatively inefficient [99]. Dermer however, was able to explain succesfully the rapid X-ray decline and plateau phase which is observed in plenty GRBs in the *Swift* era by means of the external collision model [23].

Taking into account the difficulties that arise from the external collision model it is now believed that the prompt emission is most likely the result of an internal mechanism of energy dissipation in the fast flow of the explosion. This can take place in the form of internal shock collisions for the fireball model ([90], [48], [98]) or magnetic dissipation of the electromagnetic energy when the flow is regarded as Poynting-flux dominated [55], [24], [111].

In that direction the most popular model presented so far is the 1994 internal shock model by Rees and Meszaros [90]. Disconnecting from the governing idea that the gamma-rays were produced in the external shock while it encountered the circumburst medium, they proposed a model in which an internal shock occurs when a faster ejecta catches up with a slower one previously ejected from the source. To justify this choice they considered an unsteady spherically

symmetric wind from a newly formed pulsar, or the debris from the coalescence of a compact binary into a black hole and the formation of an accretion disk. Such time variations of the central source had been considered earlier that year by Paczynski and Xu [82] in order though not to explain the gamma-rays but to predict "neutrino bursts" from GRB sources as a result of baryon contaminated ejecta colliding with each other. Rees and Meszaros showed that an efficient ($\sim 20\%$) conversion of the kinetic energy of the flow to gamma-rays takes place internally within the fireball even if the baryon mass is not negligible as other models required. Furthermore, the extreme Lorentz factor (~ 1000) imperative for external shock models to work effectively, was reduced to ~ 100 with a fluctuation ~ 2 around that number.

1.4.1 The fireball model

The concept of a "fireball" of high energy photons was initially introduced in 1978 by Cavallo and Rees in order to explain the origin of what was at the time considered as soft spectra of GRBs [18]. The fireball model describes the chain of events following a sudden release of an extreme amount of energy from a relatively small volume and its transformation to high energy (MeV) photons. Assuming that these photons are produced from some energetic processes near the compact object, Cavallo and Rees suggested that due to pair production the fireball would be opaque to γ-rays. In that case a pair dominated flow would evolve as a perfect fluid thus providing the system with an extra cooling mechanism which lowers the temperature. When the temperature falls below the pair-production threshold the fireball becomes transparent and the γ-rays escape from the system.

In 1986, Pazcynski developed a fireball model consisting of a steady optically thick wind, rather than a transient burst, to show that GRBs are of cosmological origin [80]. In his model the wind is composed by radiation and electron-positron pairs but demonstrated a practically black body radiation spectrum which conflicted with observations. Goodman on the other hand proposed a model in which the explosion is abrupt and proved that if the energy density of the emitting region is high enough, the source will be optically thick to pair creation [35]. Despite the differences in the initial conditions of these two models the behavior of the two "fireballs" is very similar. Both of these models however describe pure radiation driven relativistic fireballs where the presence of baryonic matter is excluded. It was later regarded that a baryonic load, either present at the circumburst medium or directly induced from the central engine into the fireball, could account for a great part of the flow. In 1990, Shemi and Piran proved that in either case the energy of the fireball will eventually be transferred to kinetic energy of the baryons and no electromagnetic signal will be observed.

If the baryonic mass load is small then the flow will be accelerated to relativistic speeds, whereas if the mass is large, the net result will be a Newtonian flow [104] .

Nowadays, in its latest form (see [85] for a detailed review) the fireball model is widely recognized as one of the most adequate mechanisms describing GRBs from their initial acceleration phase to the deceleration of the jet in the circumburst medium. It incorporates the internal collision model ([90], [98]) in order to explain the gamma-ray prompt emission as well as an external shock collision model to describe the afterglow.

1.4.2 The compactness problem

One of the major drowbacks that had to be dealt within the fireball model was the "compactness problem". As argued by Ruderman [93] and Schmidt [102] both presenting models in favor of a non-cosmological origin for GRBs, the parameters of the central region implied from observations suggest that the emitting source can be opaque to the gamma rays. More precisely, the fast time variability δt observed in GRB light curves, $\delta t \sim 10^{-2}$ sec, implies that the size of the central region should be approximately $R_i \preceq c\delta t \simeq 3 \times 10^3$ km. Given an observed fluence F and distance from the source D, the total energy release, assuming that the source emits isotropically, is:

$$E = 4\pi D^2 F = 10^{50} ergs \left(\frac{D}{3000 Mpc}\right)^2 \left(\frac{F}{10^{-7} ergs/cm^2}\right). \qquad (1.1)$$

Now, two gamma rays of energy E_1 and E_2 annihilate and produce pairs via $\gamma\gamma \rightarrow e^+e^-$ when the condition $(E_1 E_2)^{1/2} > m_e c^2$ is satisfied. Assuming that the fraction of photons that satisfy this condition is f_p, the optical depth of this process is:

$$\tau_{\gamma\gamma} = \frac{f_p \sigma_T F D^2}{R_i^2 m_e c^2}, \qquad (1.2)$$

where σ_T is the Thompson cross-section. Given typical values for the observed fluence and distance of the central object, the optical depth becomes very large. The gamma-rays therefore, should have been absorbed long before they could reach the observer. The non-thermal spectrum of GRBs however, suggests otherwise. The reason for this inconsistency is that the above simplified calculation does not take into account the relativistic nature of the event. Assuming that the emission region moves with a bulk Lorentz factor Γ towards the observer, the optical depth of the pair-production process is affected in two ways. First, the emitted photons are blue-shifted due to the relative motion of the source which lowers their energy by a factor Γ. In other words, what we

observe as gamma rays is in fact X-rays in the frame of the expanding shell. In that way, the fraction of the photons that are above the pair-production threshold is decreased significantly by a factor $\Gamma^{2(a-1)}$, where $a \sim 2$ is the photon's spectral index. Second, the physical size of the emitting region is actually a lot larger than the one inferred by the observed variability of the source, $R \preceq \Gamma^2 c\delta t$. In total the correction after accounting for relativistic effects to the previous calculation of the optical depth is Γ^{2+2a}. That translates to a Lorentz factor $\Gamma \succeq 100$ in order for $\tau_{\gamma\gamma} < 1$. Such extreme relativistic bulk motion is the highest observed in any other galactic or extragalactic object making GRBs one of the most violent events of the universe.

1.4.3 Poynting-flux dominated flows

Although the fireball model provides an adequate discription for the majority of the observed properties of GRBs there is still discussion concerning the dynamical importance of magnetic fields during the evolution of the burst. In that direction two categories of models including magnetic fields have been proposed, the electromagnetic model developed by Usov in 1992 [114] and Lyutikov & Blandford in 2003 [56], and a relativistic MHD model by Vlahakis & Konigl [122], [123], which investigates the properties of Poynting-flux dominated flow.

Electromagnetic models depend upon the assumption that the energy powering the GRB comes from the rotational energy of a relativistic rotating stellar-mass central object. That can be a fastly rotating neutron star or a black-hole accretion disk system. In both cases a build-in magnetic field exists possibly originating from a local dynamo mechanism, creating a Poynting-flux dominated polar outflow (see [87] for a two dimensional simulation). As Usov proposes, a rapidly rotating neutron star of millisecond scale period, produced as the result of white dwarf merger, looses its rotational kinetic energy on a timescale of seconds or less [114]. A requirement for this is the presence of an extremely strong magnetic field of the order of 10^{15}G. According to Usov, gamma-rays are produced by particles which are accelerated to ultra-relativistic energies by a strong electric field which is induced near the surface of the neutron star. Part of the gamma-rays are then reabsorbed from the magnetic field producing electron positron pairs possibly accounting, according to Usov, for the observed variability of the flux.

Building on that, Lyutikov and Blandford proposed a model of a strong Poynting-flux dominated flow where the power is dominated by its electromagnetic component rather than the heat component of the fireball. According to this model the kinetic rotational energy of the central source is transformed into

magnetic energy in the same way as described by Usov. The strongly magnetized wind is now driven subsonically by the magnetic field to long distances from the source until the emitting regions of the jet. In that case the acceleration of particles producing the observed gamma-rays occurs due to magnetic dissipation processes (magnetic reconnection or other electromagnetic instability) and not due to internal shock collisions as described in the fireball model [56].

Vlahakis & Konigl proposed in 2003 an MHD model describing an outflow which evolves temporally from thermally accelerated to magnetically driven. They derived the exact radially self-similar solutions of an axisymmetric outflow from a strongly magnetized rotating central object and demonstrated that an efficient acceleration of the particles can be reached while Poynting-flux is converted into kinetic energy of the baryons. This model was applied by Vlahakis & Konigl in the case of a trans-Alfvénic GRB outflow. Although initially Poynting-flux dominated, the flow may also consist of a lepton/photonic component, baryonic matter and the electromagnetic field. At early stages the outflow is thermally accelerated, that is the enthalpy is transformed into kinetic energy and the field is force-free. Later on and after the crossing from the fast-magnetosonic point, the flow becomes magnetically driven, i.e. the Poynting flux is transformed into kinetic energy. At this stage the conversion efficiency of the total energy reaches 50%. That means half of the initially injected Poynting flux dominated energy is transformed into kinetic energy of the flow, result which is also consistent with the efficiency expected from the internal shock scenario for GRBs. We have to note however that in contrast to non-magnetized outflows where the sound speed of the ejecta is low and the shocked matter moves supersonically with respect to the unsocked shell, shock formation is greatly suppressed in Poynting flux dominated flows due to the high sound speed of the ejecta, behavior which casts doubts on the applicability of these models in GRBs where the existence of strong shocks is a binding condition.

1.5 The Afterglow

The bright prompt phase with the characteristic variability in gamma-ray is followed by an extended emission which lasts for several days after the burst. It spans a great part of the spectrum from X-ray to radio frequencies and often displays a strong time variability which up-to-date has been difficult to explain. While the prompt phase is characterized by timescales in the order of seconds, the afterglow may last from hours up to several days after the prompt emission has ended. This quality makes the afterglow light curves an ideal mechanism in order to study several aspects concerning the behavior of the GRB jet/ejecta.

Both prompt emission and the afterglow have been explained in terms of the internal-external shock model for GRBs. The prompt emission, as described earlier in section 1.4, is considered to be the radiative product of energy dissipation occuring during shock collisions in the interior of the jet when a fastly ejected relativistic shell catches up with a slower one. However, not all the energy of the relativistic shells is dissipated to radiation during the prompt emission. The remaining kinetic energy drives an external shock and is converted to radiation via the synchrotron mechanism while the external shock decelerates in the circumburst medium [99]. Small scale magnetic fields tangled in the region of the shock front are generated by the Weibel instability providing the necessary mechanism for synchrotron emission from electrons accelerated at the shock front. Despite the obvious dynamical dependency between the two, a direct mechanism correlating the γ-ray fluxes of the prompt emission and the x-ray or optical fluxes of the afterglow has not yet been identified.

The first afterglow was observed with *BeppoSAX* as the optical and X-ray counterpart of GRB 970228 and immediately caught the attention due to its power law behaviour which had already been predicted from the theory of expanding relativistic blast waves [129], [96], [29].

Achromatic breaks in afterglow light curves are commonly observed in recent multiwavelength observations. This observational property is in fact what comfirmed the idea that behind GRBs are well hidden extreme collimated jets dismissing the so far governing idea of a spherically evolving explosion. The reason for that is again hidden in the relativistic nature of GRBs. Let's assume the blast wave producing the afterglow emission is moving towards the observer with a speed very close to the speed of light. Then in the frame of reference of the shock front the emission will be spherically symmetric. At the observer's frame however, the radiation from the source will be collimated in a conical surface of half opening angle $\theta = 1/\Gamma$, where Γ is the Lorentz factor of the emitting region. Assuming that the emitting region has conical shape of half opening angle θ_0, then when the jet is significantly decelerated so that $1/\Gamma = \theta_0$ the edges of the emitting region will become visible. At that time and if there is no significant spreading of the jet in the sideways direction, a break in the lightcurve will appear as a result of the lack of photon flux arriving from that region.

1.5.1 Flares and rebrightenings

Understanding the evolution of GRB jets is of vital importance in order to explain the complicated structures appearing in GRB light curves and spectra. In recent years the Swift Gamma-Ray Burst mission (Gehrels et al. 2004)

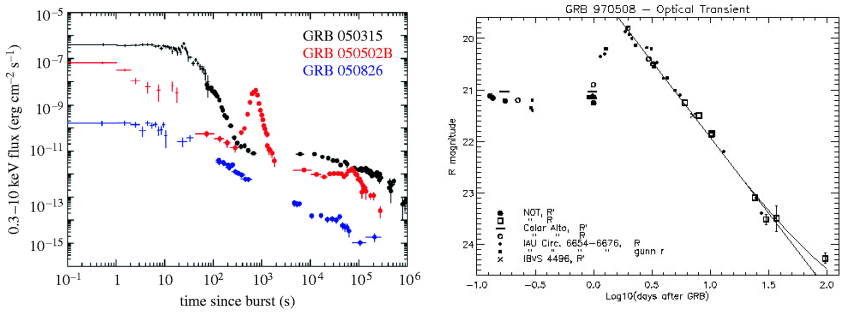

Figure 1.3: X-ray (left) and optical (right) flares, showing different characteristics in the pre and post flare slope, indicating that a different physical mechanism takes place in the two cases. An internal enery dissipation mechanism is considered for the first one, while an external collision mechanism is the most likely explanation for the latter one. The data of the left picture are collected by the *Swift* telescope. *BAT* data are shown as crosses, while *XRT* data as circles (From O'Brien et al. 2006 [78]). The *R* band light curve of GRB 970508 at the right picture is constructed from observations conducted at the Nordic Optical Telescope (*NOT*) and the German-Spanish Calar Alto observatory (*CAHA*). Courtesy of Neil Gehrels, http://rsta.royalsocietypublishing.org/ (left figure) and H. Pedersen, [83] (right figure).

has provided us with an enormous amount of data covering the prompt and afterglow emission of hundreds of GRBs unveiling details the comprehension of which require a further understanding of the GRB jet propagation properties.

More precisely, strong temporal variability is observed in afterglow light curves covering a broad range of frequencies and appearing eminently in the X-ray and optical. At the same time strong differences appear in the qualitative characteristics of this variability between various events, thus indicating that more than one physical mechanism is responsible for this occurence. Quite often a steep increase of the photon flux is observed in X-rays lasting for only a few seconds accompanied by a concurrent increase in the optical (see GRB 060607A in [72], GRB 060904B in [47] and and GRB 071031 in [50]). It is also commonly encountered that the X-ray and optical peak times coincide, see GRB 060418 in [72]. Some early X-ray bumps, referred in literature as X-ray flares, appear without corresponding optical features, [63] and [95], while similarly, but less frequently, optical flares are encountered without an X-ray counterpart, [4].

In Fig. 1.3 an example of bursts is demonstrated showing a canonic behaviour (GRB 050315) and strong flaring activity (GRB 050502B) [78]. The X-Ray flare noticed in the light curve of GRB 050502B shows a common slope for the

pre and post flare region indicative of internal mechanism of energy dissipation which creates the bump and seize to exist after the flaring activity is over. On the other hand the optical flare of GRB 970508 depicts an event for which the physical mechanism responsible for the flare has influenced the slope of the afterglow. In that case an external collision mechanism is assumed to be responsible for the generation of the flare since a mechanism which alters the properties of the forward shock has to take place.

In that direction several models were proposed in order to explain the multiwavelength variability detected in the majority of GRB afterglow light curves (Barthelmy et al. 2005; O'Brien et al. 2006; Burrows 2005;Falcone et al. 2006). It has been suggested that an inhomogeneous medium around the collapsing star can give rise to such variability (Lazzati et al. 2002). Several numerical models have tested that theory (Nakar & Granot 2006; van Eerten et al. 2009), concluding that it is possible to produce small rebrightenings of the afterglow when the blast wave of the explosion propagates through a "bumpy" medium. In order to reproduce stronger flares however, unrealistic density jumps were used. It has to be noted however, that so far numerical models have only accounted for spherical explosions in order to validate this model. It is in our belief that the more appropriate use of a collimated outflow, as it is now widely accepted that follows the collapse of a massive star, can give rise to sharp features in the light curves.

A second category of models, relies on the assumption of a long lived central engine which after the initial explosion producing the gamma rays has ended, continues to supply the system with consecutive ultra-relativistic shells. These models are classified into two main categories. The internal collision models (Rees & Meszaros 1994; Kobayashi et al. 1997), which explain the observed variability in terms of collisions of the shells in the interior of the jet, and the external collision models according to which the collision takes place at the external shock (Rees & Meszaros 1998). According to the first one, the shells are ejected with a varying Lorentz factor and therefore collide when a faster one catches up with a slower one. The dissipation of energy occurring during that phase gives sharp flares at the afterglow. According to the second one (hereafter external shock refreshment model) the shell will catch up with the external shock when the latter one is sufficiently decelerated. The energy injection during that phase is expected to produce a rebrightening of the afterglow. A schematic representation of the incorporation of these two models in one unified theory is shown in Fig. 1.4.

Afterglow light curves play a important role in deducing structural characteristics of the emitting region which would otherwise be concealed. Estimations of the opening angle of the jet can be made by studying the jet break time (see subsection in chapter 2 for more details) while the width and occuring time

of the flares insert constraints on the size of the internal source and the total energy of the explosion [60], [15]. Characteristics of the circumburst medium (as the ones examined in chapter 4) can be also deduced by studying the afterglow properties. The understanding of the connection between the various aspects of the afterglow and the dynamics of the underlying jet and emitting source requires a direct comparison between light curves from different bands of the spectrum.

1.6 Multiwavelength afterglow lightcurves

Our understanding of the emission mechanisms forming both the prompt and afterglow radiation, gravely increased after the *Swift* mission was launched in 2004. The afterglow emission during the deceleration of the jet in the circumburst medium is convincingly explained in terms of synchrotron emission from the accelerated electrons at the shock front. On the contrary the means in which the initial ejecta converts its mass energy into radiation during the prompt phase is not yet fully understood. The continuous supply of multiwavelength lightcurves and spectra has given the opportunity of thorough study in different bands of the spectrum. A detailed cross-study comparison between X-ray, optical and radio afterglow light curves is required in order to shed light on the physical mechanisms which shape the afterglow.

Prior to the launching of the *Swift* mission, a typical afterglow lightcurve would start several hours after the burst had ended, showing a rather smooth decay of the observed photon flux. The early afterglow however, starting immediately after the prompt emission, reveals great information about the structure and nature of the emitting region. Recently, significant progress has been made after studying the afterglow data collected by *XRT* and *BAT*. X-ray afterglow light curves present a canonical behavior similar to the one shown in Fig. 1.5 which consists of three distinct regions: (1) the initial very steep decay ($\propto t^{-a}$ with $3 \lesssim a_1 \lesssim 5$) followed by (2) a shallow decay phase, which often presents a strong flaring activity ($0.5 \lesssim a_2 \lesssim 1.0$) and (3) a subsequent moderate decay phase ($1.0 \lesssim a_3 \lesssim 1.5$).

1.6.1 Steep decay phase

Contrary to early assessments that this part of the light curve originates from the same regions on the jet that give rise to the afterglow radiation, nowadays the initial steep decay phase is considered to be part of the prompt emission of a GRB. As described extensively in literature (Fenimore 1996; Dermer 2004;

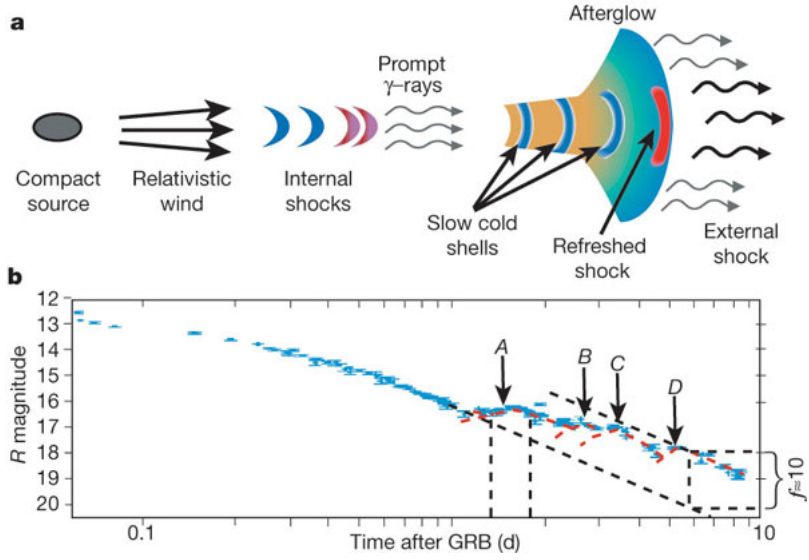

Figure 1.4: a. Cartoon model of the collision between ultrarelativistic shells within the evolution of a GRB jet. Internal collisions produce the γ-rays during the prompt emission phase, while at later times collisions due to a long lived central engine, produce a *refreshed* external shock during the afterglow. b. Optical light curve of GRB030329. The bumps at the afterglow phase can be interpreted as emission from a refreshed external shock (Granot Nature 2003).

Zhang 2006) this transitional phase is in fact *tail emission* from the prompt phase delaying to reach the observer due to the *curvature effect*.

As internal shocks within the GRB jet produce the gamma-rays, the region of the shock front at which most of the emission takes place, lies in angles higher than the observer's line of sight, thus delaying for $\Delta t \approx R\theta^2/2c$ until it reaches the observer. This interpretation however requires a smooth transition in the light curves between the prompt phase and the afterglow. O'Brien et al. 2006, analyzed 40 X-ray light curves collected by BAT and XRT for which the instruments were pointed at the burst within 10 minutes from the trigger thus providing the necessary temporal bridge between the two phases of the burst. The result was that a combination of high latitude emission, due to the *curvature effect* and an early afterglow component could account for the observed flux decay.

Nevertheless, since not all afterglow light curves present such a steep decay phase, albeit most of them do, or at some cases it appears to be shallower,

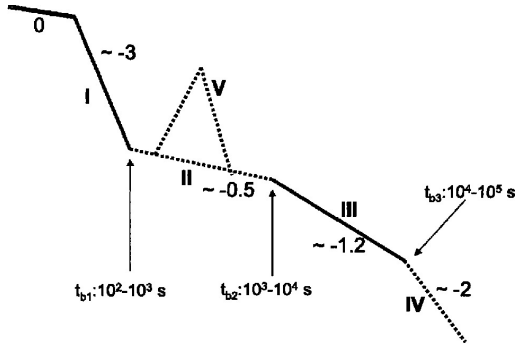

Figure 1.5: Synthetic X-Ray light curve as constructed from observational data collected from *Swift* satellite mission. The five characteristic phases of the afterglow (steep decay phase - segment I, shallow decay phase - segment II, normal decay phase - segment III, post jet brake phase - segment IV) are illustrated together with the prompt emission phase 0. Segment V represents the period where strong flaring activity is observed (figure courtesy of Zhang et al. 2006 [139]).

several other interpretations have been proposed. Kobayashi et al. (2005) proposed that the steep decay phase may result in some cases at least from the reverse shock propagation in a magnetized ejecta. Considering the synchrotron and synchrotron self inverse Compton emission mechanisms they demonstrate that in a low magnetization ejecta, the propagation of the reverse shock can induce a steep decay in the early X-Ray afterglow light curve provided the Compton parameter is low enough. Pe'er et al (2005), argued that a *cocoon*, composed by the shocked jet material that accumulates while the jet forces its way out of the stellar envelope, will continue to expand relativistically for a little longer after the break out of the jet. In that case, the steep decay phase is explained in terms of delayed arrival time of the X-ray photons due to multiple Compton scatterings inside the *cocoon*.

1.6.2 Shallow decay phase

One of the most striking features arising from early afterglow observations was the shallow decay phase. The change of the spectral index from the steep decay phase suggests that a different emitting region is responsible for the two phases. Several mechanisms which can produce such a change in the slope have been proposed. The most common interpretation for this phase requires an energy injection in the external shock (Nousek et al. 2006). This can take place in

mainly two forms. In the first one, the burst produces an ejecta in which the mass fraction ejected and the coresponding energy decrease as a power-law distribution of the Lorentz factor. In such a case, a smooth energy injection is expected at the external shock while faster material continuously catches up with the external shock. In the second approach the central engine remains active for a long time after the burst while continuously producing ejecta. In that scenario material with Lorentz factor Γ will catch up with the external shock when the Lorentz factor of the latter one drops below Γ.

Two-component jet models have also been proposed to explain the shallow decay phase. According to these models a GRB jet consists of a fast highly relativistic inner jet which produces the prompt emission and an outer slower component that decelerates at significant later times. In that view, the shallow decay phase is produced when the outer component starts decelerating at later times by transfering its energy to the external shock and thus contributing to the early afterglow contrary to its inner counterpart (Granot, Konigl & Piran 2006).

1.6.3 Normal decay phase

The second break in a typical afterglow light curve occurs when the energy injection at the external shock is finished. This transition can happen in two ways. Either when the Lorentz factor of the ejecta drops below the minimum Lorentz factor of that fraction of the matter that carries a significant amount of the initial energy, or when the internal engine simply becomes inactive. In both cases the energy injection in the afterglow ends, and the behavior of the external shock is now fully determined by its energy and the density of the circumburst medium. This canonical behavior represents the *moderately steep decay phase* which extends until the Lorentz factor of the jet drops below θ_j^{-1}.

1.6.4 Post jet break phase

When the Lorentz factor of the jet drops below θ_0^{-1} the physical boundaries of the jet becom visible to the observer. Subsequently, if the jet has not significantly expanded in the sideways direction, a break in the observed photon flux is expected from the lack of emission from the regions outside of the jet boundaries. This transition is referred to as the jet break during which the Lorentz factor of the jet is decreasing exponentially with the radius. Emission from this part of the flow is attributed to the forward shock.

1.7 Numerical simulations of the afterglow

In recent years several numerical efforts have been dedicated in studying the propagation of a GRB jet during its afterglow phase. The pioneering work in this direction was by Granot et al. (2001) and employed a GRB jet expanding into an ambient medium. This simulation showed that the analytical estimations by that time had overestimated the sideways expansion of the jet. Following this work, Cannizzo et al. [16] investigated in 3D the deceleration of the blob of gas associated with the GRB jet and studied the expansion of the jet during the transition from the relativistic to the Sedov-Taylor phase, a simulation though which suffered from low resolution. Both of these simulations envolved moderate values for the Lorentz factor, compatible however with the inferred values from observations. Meliani et al. [65] performed 2D simulations of the afterglow, adopting extreme physical properties for the jet, ($\Gamma = 100$ and $\theta_0 = 1^\circ$) verifying the previous inconsitency between numerical and analytical work. Employing extreme radial resolution, Meliani and Keppens [64] repeated these simulations, using more moderate values for the jet initial conditions and showed that a Vishniac type instability takes place at early stages of the jet propagation due to the extreme difference in pressure in the direction perpendicular to the shock. Recently, many numerical codes have become available calculating the radiation during the deceleration of a GRB jet, thus allowing for comparison with observations. Zhang and MacFadyen [142] produced light curves from a jet propagating into a constant medium and studied its evolution for a large time period. They showed that during the transition from the relativistic to the spherical Sedov-Taylor phase a flattening in the light curves is produced. De Colle et al. [21] studied the influence of a stratified external medium on the dynamical behaviour of the jet and the shape of the light curves. This simulation engaged extremely high resolution and a numerical code dedicated solely to the study of GRB jet propagation.

The extreme physical conditions in which a GRB is formed impose various numerical constraints which are necessary to be dealt with before realizing a simulation. The external shock which is set at the jet front, is extremely thin due to the ultra-relativistic nature of the explosion and propagates for a great distance of the scale of Mpc. In terms of the numerics, this translates to extremely high resolution essential for capturing all the details of the shock front. In addition, the opening angle of the jet as inferred from observations has to be extremely small ($\sim 2^\circ - 10^\circ$) which also imposes strong numerical challenges to the simulation.

1.8 Dynamical description of a decelerating blast wave. The relativistic and nonrelativistic regimes

In fluid dynamics a blast wave is considered as the result of a highly energetic explosion in a very small volume. Examples include nuclear explosions or astrophysical phenomena such as supernova explosions. The blast wave consists of the supersonic expanding fluid and a shock surface which separates it from the curcumburst medium. At its classical version this problem has been extensively analysed independently by Sedov and Taylor [103],[110] in the case of a supernova explosion and was generalized to the relativistic regime by Blandford and McKee [10]. Both of these models take adavantage of the principles of *self-similarity* which simplifies grately a rather complex mathematical problem. By this it is implied that the shape of density, pressure and velocity radial profiles are independent of time and one can reconstruct these profiles at any time, given a simple *scaling relation* between radius and time.

1.8.1 The Sedov-Taylor solution

In the Newtonian limit of classical velocities ($\ll$ than the speed of light) the properties of the dynamical parameters across a shock surface are given by the *Eulerian jump conditions*, also refered to as Rankine-Hugoniot relations. By measuring the strength of the shock with the *Mach number M*, defined as the speed of the upstream flow over the sound speed, $M \equiv u_1/c_1 = \sqrt{u_1^2\rho_1/\gamma p_1}$ we write the jump conditions in the following form,

$$\frac{\rho_1}{\rho_2} = \frac{u_2}{u_1} = \frac{\gamma-1}{\gamma+1} + \frac{2}{(\gamma+1)M^2}, \tag{1.3}$$

$$\frac{p_2}{p_1} \simeq \frac{2\gamma M^2}{\gamma+1}, \tag{1.4}$$

where ρ,p,u are the density, pressure and velocity of the flow in the upstream (denoted with index 1) and downstream (denoted with index 2) direction. By upstream and downstream we refer to the regions ahead and behind the shock front respectively.

In that case, one can easily reconstruct the self-similarity scaling factor by simple dimensional arguments. Assuming a spherical explosion of energy E, the swept up mass after time t where the shock front is at radius $R(t)$, will be $\sim \rho R^3$, where ρ is the density of the expanding fluid. The energy of the

explosion will consist mainly of the kinetic energy of the flow, $E_k \sim \rho R^5/t^2$ and the internal energy of the shocked medium. The latter one can be expressed in terms of the post-shock energy density, taking a pressure given by $\rho\dot{R}^2$, as $\epsilon \sim \rho\dot{R}^2 R^3$ which gives a similar dependency on ρ,R and t. Assuming therefore, a total energy E, the radius can be expressed as a function of time as

$$R = \left(\frac{E}{\kappa\rho}\right)^{1/5} t^{2/5}, \tag{1.5}$$

where κ is a constant of order unity. Given the characteristic scale of the blast wave radius, $R(t)$, it seems appropriate to choose the quantity

$$\xi \equiv r/R(t), \tag{1.6}$$

as a similarity variable and use the jump conditions to describe the density, pressure and velocity as a function of this variable. In that case we use equations (1.3) and (1.4) to get the value of the fluid parameters right behind the shock front

$$p = \frac{2}{\gamma+1}\rho_0\dot{R}^2\tilde{p}(\xi), \tag{1.7}$$

$$\rho = \frac{\gamma+1}{\gamma-1}\rho_0\tilde{\rho}(\xi), \tag{1.8}$$

$$u = \frac{2}{\gamma+1}\dot{R}\tilde{u}(\xi). \tag{1.9}$$

In these expressions , ρ_0 is the constant upstream density and $\tilde{p}$,$\tilde{\rho}$ and $\tilde{u}$ are scale profiles of order unity.

1.8.2 The Blandford & McKee solution

In many astrophysical events however, we come across violent phenomena of extreme energies and velocities that are comparable to the speed of light. When the energy of the explosion is so large that exceeds the rest mass energy of the ambient medium and the mass energy of the explosion products, the resulting shock wave will be relativistic. In that case the Sedov-Taylor model fails to properly describe the dynamics of the blast wave in which novel characteristics are introduced due to the relativistic nature of the explosion. Similarly as

before, the jump conditions across the shock surface in the relativistic case can be written in the following form ([10]),

$$\frac{e_2}{n_2} = \gamma_2 \frac{h_1}{n_1}, \tag{1.10}$$

$$\frac{n_2}{n_1} = \frac{\hat{\gamma}_2 \gamma_2 + 1}{\hat{\gamma}_2 - 1}, \tag{1.11}$$

$$\Gamma^2 = \frac{(\gamma_2 + 1)\left[\hat{\gamma}_2(\gamma_2 - 1) + 1\right]^2}{\hat{\gamma}_2(2 - \hat{\gamma}_2)(\gamma_2 - 1) + 2}, \tag{1.12}$$

where index 1 and 2 refer to the unshocked and shocked gas respectively. The quantities γ_i,h_i,n_i and e_i represent the Lorentz factor, enthalpy, density and energy density measured in the fluid frame. Γ is the Lorentz factor of the shock measured in the unshocked gas frame and $\hat{\gamma}$ is the specific heat ratio generally lying between the values 4/3 and 5/3 for the relativistic and nonrelativistic parts of the fluid. Considering the ultra-relativistic case ($\hat{\gamma} = 4/3$) and accounting for a strong shock ($\Gamma \gg 1$) equations (1.10) to (1.12) can be easily rewritten in the form

$$p_2 = \frac{1}{3} e_2 = \frac{2}{3} \Gamma^2 h_1, \tag{1.13}$$

$$n_2' = 2\Gamma^2 n_1, \tag{1.14}$$

$$\gamma_2^2 = \frac{1}{2}\Gamma^2, \tag{1.15}$$

where $n_2' = \gamma_2 n_2$ is the density measured in the frame of the unshocked gas.

In 1976 Blandford & McKee studied the dynamics of an ultra-relativistic spherically symmetric blast wave and introduced a self-similar solution in a generalization of the classical Sedov-Taylor model. In contrast to the latter one, a relativistic explosion by definition has a characteristic velocity which is the speed of light. Obtaining therefore a self-similar variable is not as straightforward as before. However, a closer look into the jump conditions can give information on the characteristic scale height in the shocked fluid region. From equation (1.14) we notice that the density of the shocked fluid exceeds that of the unshocked by a factor of Γ^2. That means that the thickness of the blast wave within which the largest amount of the shocked particles is gathered, is R/Γ^2. Similarly, from equation 1.15 we notice that a fluid element with Lorentz factor γ_2, will travel a distance R/Γ^2 by the time it takes for the shock radius

to double. These factors suggest that an appropriate choice of the self-similar variable is

$$\xi = \left(1 - \frac{r}{R}\right) \Gamma^2 \geqq 0. \tag{1.16}$$

Considering that the energy within the blast wave remains constant, the Lorentz factor of the shock front drops as $\Gamma^2 \propto t^{-m}$, with $m > -1$. It is straightforward therefore to calculate the radius of the shock which yields

$$R = t\left[1 - \left[2(m+1)\Gamma^2\right]^{-1}\right]. \tag{1.17}$$

The shape of that function allows to change the self-similar variable in a more convenient form to

$$\chi = 1 + 2(m+1)\xi = \left[1 + 2(m+1)\Gamma^2\right](1 - r/t), \tag{1.18}$$

and rewrite the properties of the shocked fluid directly behind the shock front as

$$p = \frac{2}{3} h_1 \Gamma^2 f(\chi), \tag{1.19}$$

$$\gamma^2 = \frac{1}{2}\Gamma^2 g(\chi), \tag{1.20}$$

$$n' = 2n_1\Gamma^2 h(\chi), \tag{1.21}$$

where $\chi \geq 1$ and $f(1) = g(1) = h(1) = 1$ since $\chi = 1$ is the shock location. For an "impulsive" injection of energy the three functions of the self-similar variable are obtained as simple power-laws, namely

$$f = \chi^{-17/12}, \tag{1.22}$$

$$g = \chi^{-1}, \tag{1.23}$$

$$h = \chi^{-7/4}. \tag{1.24}$$

Even though several self-similar models have been proposed to describe expanding relativistic blast waves, the BM self-similar solution continues to be a great approximation which explains the deceleration phase of a GRB and which due to its simplicity can easily be integrated in numerical schemes such as the ones we describe in the following chapters.

1.9 Radiative processes shaping the afterglow

It is still not clear which is the dominant radiation mechanism responsible for the generation of gamma-rays in GRBs. The two most likely candidates however, appear to be *synchrotron radiation* and *inverse Compton scattering* taking place during the internal shock collision as described earlier in section 1.5. On the other hand it is almost certain that the dominant mechanism creating the afterglow is *synchrotron radiation* from electrons accelerated at the external shock.

Synchrotron radiation is emitted when ultra-relativistic particles are accelerated by a magnetic field and it is the relativistic analogous of cyclotron radiation in classical physics. While in the rest frame of the particles this radiation is emitted isotropically, this is not the case for an observer moving with constant velocity in respect to that frame. In that case, when the Lorentz factor of the particles γ, is far greater than unity, the observer will see the emitted radiation confined in a cone of half opening angle $\theta \sim 1/\gamma$, while only very few photons will be emitted having $\theta >> 1/\gamma$. This is called the *beaming effect* and it is of paramount importance in modern GRB and afterglow theory.

Calculating the observed flux and thus constructing light curves for synchrotron radiation can be a complicated task given that one has to solve the radiative transfer equation along the jet

$$\frac{dI_\nu}{dz} = -\alpha_\nu I_\nu + j_\nu, \tag{1.25}$$

where α_ν and $j_\nu = d^2P_V/d\nu d\Omega$ is the absorption and emission coefficient respectively. I_ν is the specific intensity of the flux P_ν is the radiated power per unit volume and $d\Omega$ is the solid angle.

Using the emission theory for relativistic particles, we can calculate the emitted power for synchrotron radiation. From *Larmor's formula* for emission from a single charge q with acceleration $\mathbf{a}$, we have

$$P = \frac{2q^2}{3c^3}\gamma^4 \left(a_\perp^2 + \gamma^2 a_\parallel^2\right) \tag{1.26}$$

where $a_\perp$ and $a_\parallel$ are the perpendicular and parallel with respect to the magnetic field components of the acceleration vector and γ the lorentz factor of the accelerated particle. Thus, the emitted power can easily be calculated in any frame by computing $\mathbf{a}$ in that particular frame. For synchrotron radiation the particle is moving along the magnetic field lines and the above relation is written in the form

$$P = \frac{4}{3}\sigma_T c\beta^2\gamma^2 U_B \tag{1.27}$$

where $\sigma_T = 8\pi r_0^3/3$ is the Thompson cross section and $U_B = B^2/8\pi$ is the magnetic energy density. Here r_0 is the classical electron radius and β is the velocity of the particles normalized to the speed of light.

As in the case of any radiation process, similarly in *synchroton radiation*, emission is accompanied by absorption when emitted photons are absorbed by accelerated electrons. This process is called *synchrotron self absorption* and plays a crucial role in all astrophysical systems where radiation travels a long distance within the emitting region before reaching the observer. This process is quantified through the synchrotron self absorption coefficient, α_ν, given by

$$\alpha_\nu = -\frac{c^2}{8\pi\nu^2}\int dE P(\nu, E) E^2 \frac{\partial}{\partial E}\left[\frac{N(E)}{E^2}\right]. \tag{1.28}$$

Here the integral is taken over an energy range defined by the minimum and maximum Lorentz factor of the electrons distribution. Assuming that the distribution of the accelerated electrons by the shock is a power-law, $N(\gamma_e) = K\gamma_e^{-p}$ for $\gamma_e \geq \gamma_m$ and that the fraction of the accelerated electrons is ξ_N, one can estimate the minimum Lorentz factor of the accelerated electrons assuming that the energy of the electrons is everywhere a constant fraction ϵ_E of the thermal energy stored behind the shock, $\varepsilon'_e = \epsilon_E e'_{th}$. Note that primed quantities denote values in the rest frame. This gives,

$$\gamma'_m = \left(\frac{p-2}{p-1}\right)\frac{\epsilon_E e'_{th}}{\xi_N n' m_e c^2}, \tag{1.29}$$

where m_e is the electron mass and n' the number density in the comoving frame. Accordingly the synchrotron peak frequency ν'_m is related to the lower cut-off Lorentz factor via

$$\nu'_m = \frac{3q_e}{4\pi m_e c}\gamma'_m B', \tag{1.30}$$

and thus one can rewrite the synchrotron self-absorption coefficient from (1.28) to,

$$\alpha_\nu = -\frac{1}{8\pi m_e \nu'^2}\int_{\gamma'_m}^{\gamma'_M} \frac{dP'_e}{d'_\nu}\gamma'_e \frac{\partial}{\partial\gamma'_e}\left[\frac{N_e(\gamma_{e'})}{\gamma'^2_e}\right] d\gamma'_e. \tag{1.31}$$

When electron cooling does not play an important role on the system the received power can be quantified via

$$\frac{d^2P_V}{d\nu d\Omega} \propto \frac{\xi_N n B'}{\gamma^3(1-\beta\mu)^3} Q\left(\frac{\nu}{\nu_m}\right), \tag{1.32}$$

where $Q(\nu/\nu_m)$ is a dimensionless function defining the shape of the spectrum and $\mu = cos\theta$ is the cosine of the angle between the vector of the velocity and the line of sight.

Given the above quantities one can numerically solve the radiative transfer equation and obtain the observed photon flux for given distance of the observer. For more details and explicit expressions of the shape functions $Q(\nu/\nu_m)$ we refer to [118] and [115].

1.10 A numerical approach in relativistic hydrodynamics for a GRB jet propagation

In understanding the physical mechanisms behind highly energetic astrophysical phenomena, such as flows in accretion disks around compact objects, supernova explosions, binary mergers or jetted outflows, like it is in the case of a GRB jet formation and propagation, it is of vital importance to use numerical algorithms that solve the non-linear equations of relativistic (M)HD. In recent years, in the absence of analytical solutions, the exploitation of numerical simulations has become a necessity in studying such complex phenomena. This led to the assembly of highly sophisticated numerical codes such as MPI-AMRVAC [43], ATHENA [109], ENZO [79], FLASH [28], PLUTO [69], RAM [143], which offer a great variety of physical implementations and numerical schemes for a more realistic representation of the physical conditions of the case in study. In this thesis, we use the MPI-AMRVAC throughout.

1.10.1 MPI-AMRVAC

MPI-AMRVAC is a numerical code, developed in Fortran 90 parallelized with the Message Passing Interface (MPI) (Keppens et al. 2012). It aims in solving any system of hyperbolic partial differential equations and emphasizes on the versatility of shock capturing methods applicable in hydrodynamics, special relativistic hydrodynamics (srhd) and magnetohydrodynamics (srmhd). The code exploits an adaptive mesh refinement (AMR) strategy to generate pure octree, block-based oriented data structures. The efficiency gain and accuracy preservations of AMR computations compared to uniform grid calculations, relies mainly on the refinement and coarsening operations of the code. In MPI-AMRVAC this process consists of the following steps. First, for each level of refinement the code estimates the error at each gridpoint in a given grid block. Then, if that error exceeds a user-set error limit, the refinement of that block is triggered. If the error is smaller than the user-set value, the block

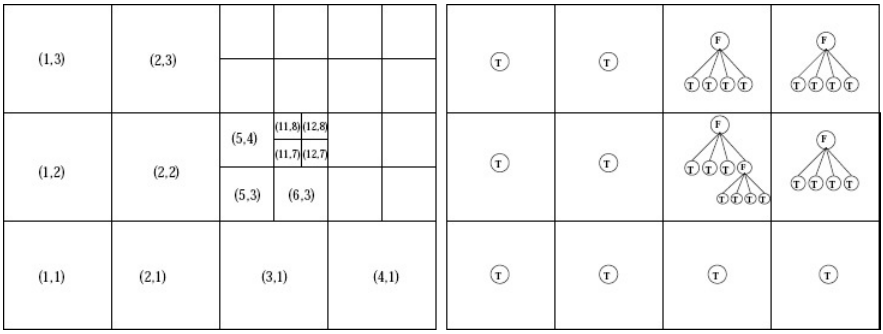

Figure 1.6: For the hypothetical cartesian grid exploiting 4×3 grid blocks at level $l = 1$, the left panel shows the global grid indices while the tree representation is given at the right panel. From Keppens et al. 2012 [43]

.

is coarsened. When a block is identified for refinement, a block-tree grid is generated. A schematic representation of the octree grid arrangement is given in figure 1.6 for a 2D case. It also includes various prescriptions for handling the equation of state (EOS) making the code ideal in dealing with complex relativistic astrophysical phenomena where Newtonian and ultra-relativistic flows have to be treated at the same time.

1.10.2 Relativistic hydrodynamics

For all the performed simulations in the following chapters we have assumed a fluid approximation for the description of the plasma dynamics. At first this choice might seem inapropriate due to the collisionless nature of the astrophysical plasma in GRBs. The mean free path for Coulomb collisions in GRBs is larger than the size of the fireball. However, the randomly oriented magnetic field which is generated due to Weibel instability and is tangled at the shock front, provides with an efficient number of collisions due to pitch-angle scattering of the particles thus justifying the use of a fluid description (see Medvedev and Loeb 1999 [61] for a detailed description of this mechanism). Furthermore, accepting the idea that emission from GRBs comes from a small scale magnetic field allows us to use the special relativistic hydrodynamic (SRHD) set of equations to describe the overall dynamics and neglect effects arising from large scale magnetic fields.

The MPI-AMRVAC code solves any set of (conservation) equations which are written in the following vector form

$$\partial_t \mathbf{U} + \nabla \cdot \mathbf{F}(\mathbf{U}) = \mathbf{S_{phys}}(\mathbf{U}, \partial_t \mathbf{U}, \partial_i \partial_j \mathbf{U}, \mathbf{x}, \mathbf{t}), \tag{1.33}$$

where $\mathbf{U}$ denotes the set of (conserved) variables and $\mathbf{F}(\mathbf{U})$ the corresponding fluxes. The presence of a physical source term $\mathbf{S}$ often breaks the conservation and is used to describe various physical conditions which are commonly encountered in astrophysical problems. In Minkowski spacetime and for an arbitrary coordinate system SRHD is described by equations (1.33) and in the absence of a source term, the conserved variables $\mathbf{U}$ and the corresponding fluxes $\mathbf{F}$ are given by

$$\mathbf{U} = (D, \mathbf{S}, \tau)^T, \tag{1.34}$$

$$\mathbf{F} = \left(D\mathbf{v}, \mathbf{S}\mathbf{v} + \mathbf{I}p, \mathbf{S} - D\mathbf{v}\right), \tag{1.35}$$

where the five conserved quantities D,$\mathbf{S}$ and τ are all measured in the lab frame and correspond to the mass density, the three components of the momentum density and the energy density (measured relative to the rest mass energy density), respectively and v^i, ρ, p correspond to the three-vector velocity, density and pressure at the local rest frame of the fluid. Lab frame quantities relate to those in the rest frame of the fluid through the relations

$$D = \rho\Gamma, \tag{1.36}$$

$$S^i = \rho h \Gamma^2 v^i, \quad i = 1, 2, 3, \tag{1.37}$$

$$\tau = \rho h \Gamma^2 - p - D. \tag{1.38}$$

In this case, h is the specific enthalpy of the fluid, given by

$$h = 1 + \varepsilon + \frac{p}{\rho}, \tag{1.39}$$

where ϵ is the specific internal energy. The system of equations (1.33) together with equations (1.34)-(1.36) is closed by means of a polytropic equation between p and ρ usually given in the form $p = p(\rho, \epsilon)$. As mentioned above, the importance of studying at the same time Newtonian and relativistic parts of the fluid demands the use of a generic equation of state, applicable in both cases. In the following chapters we exploit the Mathews equation of state [59] defined as

$$1 + \varepsilon = \frac{p}{(\gamma - 1)\rho} + \sqrt{\left(\frac{p}{(\gamma - 1)\rho}\right)^2 + 1}, \tag{1.40}$$

which is a perfect approximation from a Newtonian fluid at the limit $\gamma = 5/3$ and can be used to describe ultra-relativistic flows at the limit $\gamma = 4/3$. In fact, it boils down to an effective polytropic index which varies from 5/3 to 4/3 where needed.

1.11 Summary of the thesis

In order to confirm the external shock refreshment scenario we recently performed 1D numerical simulations of an ultra-relativistic shell catching up with the external shock during its deceleration phase (Vlasis et al. 2011). We constructed light curves in the optical and radio band assuming two different scenarios of a spherical explosion and a jetted outflow. We consider the emission mechanism to be synchrotron radiation from the electrons which are accelerated at the shock fronts. In our calculations the synchrotron self-absorption (ssa) mechanism was included which we found to strongly influence the shape of the light curves. We examined cases of different Lorentz factor and energy for the second shell in order to investigate the effects on the light curve due to different properties of the shell and found that strong rebrightenings occur when the Lorentz factor and energy of the second shell are higher. The rebrightening appears to be smooth when the explosion is considered spherically symmetric while it becomes very sharp when a jetted outflow of 2 degrees half opening angle is taken into account. The reason for that is that the effect on the light curve arising from the energy injection of the second shell is smeared out from emission originating from high angles on the jet. Therefore for a 2 degree half opening angle jet this effect is found to be more pronounced. In addition, a time delay between the optical and radio flare is observed which is explained in terms of the ssa mechanism. The jet is optically thin for optical emission while below the self-absorption frequency the jet becomes optically thick. Therefore, while the collision between the two shells is apparent in the optical as soon as the forward shock of the second shell is created, in the radio the result of the collision becomes visible only after the merger has completed.

The validity of the constructed light curves, assuming the jetted outflow scenario, from a 1D dynamical model requires the assumption that the lateral spreading during the deceleration phase of the external shock is insignificant. In our recent work (Vlasis et al. 2012 submitted for publication in MNRAS), which is described in Chapter 3 we tested that assumption. For that we performed a 2D simulation of a GRB jet of 2 degrees half opening angle propagating in a uniform external medium while a second shell catches up. Previous numerical simulations of one shell decelerating in a uniform external medium, have shown that the spreading of the jet is a very slow process as long as the jet is still

relativistic (Zhang & MacFadyen 2009 [143]; Meliani & Keppens 2009 [64]; Wygoda, Waxman & Fril 2011 [134]). In agreement to that although some novel characteristics are introduced to the problem, no significant alteration of the spreading of the jet is observed due to the presence of the second shell. We notice however an angular variation of the properties of the system, due to the extraction of energy at the position of the external shock due to a rarefaction wave that propagates in the transverse direction. That has an influence on the collision time between the forward shock of the second shell and the external shock. At higher angles on the jet, the external shock decelerates faster compared to on-axis and therefore collides sooner with the forward shock of the second shell. In terms of synchrotron emission from the jet, we predict that the light curve from such a system will be affected in two ways. First, albeit small, the expansion of the jet will cause a moderate flattening of the flare compared to the one constructed from the 1D model. Second, due to the angular dependency of the collision, strong differences are expected between on-axis and off-axis light curves.

Out progress towards a more complete description of a GRB jet propagation is presented in Chapter 4. Following the assumption that massive stars are the most likely progenitors for GRBs, we simulate the evolution of the circumstellar medium around a fast rotating massive star in a two-dimensional hydrodynamic model. The product of this simulation is used afterwards as the initial conditions for the GRB jet propagation. This is done in a one-dimensional long run simulation, where the transition of the jet from the termination shock of the bubble is approached from a dynamical and a radiation point of view, as well as in two dimensions where we present our preliminary dynamical results of a high-resolution simulation. We find that moderate rebrightening of the light curves is obtained during the crossing of the jet from the termination shock while a flaring event is taking place during the merger of the two shells. In 2D we notice the development of an instability in the transverse direction during the early highly relativistic stages of the propagation of the external shock and compare it with previous findings. Conclusions and an outlook to future work is given in chapter 5.

Chapter 2

Two-shell collisions in the GRB afterglow phase

2.1 Preface

Strong optical and radio flares often appear in the afterglow phase of Gamma-Ray Bursts (GRBs). It has been proposed that colliding ultra-relativistic shells can produce these flares. Such consecutive shells can be formed due to the variability in the central source of a GRB. We perform high resolution 1D numerical simulations of late collisions between two ultra-relativistic shells in order to explore these events. We examine the case where a cold uniform shell collides with a self-similar Blandford and McKee shell in a constant density environment and consider cases with different Lorentz factor and energy for the uniform shell. We produce the corresponding on-axis light curves and emission images for the afterglow phase and examine the occurrence of optical and radio flares assuming a spherical explosion and a hard-edged jet scenario. For our simulations we use the Adaptive Mesh Refinement version of the Versatile Advection Code (MPI-AMRVAC) coupled to a linear radiative transfer code to calculate synchrotron emission. We find steeply rising flare like behavior for small jet opening angles and more gradual rebrightenings for large opening angles. Synchrotron self-absorption is found to strongly influence the onset and shape of the radio flare.

2.2 Introduction

The internal shock collisions version of the fireball model provides an adequate description of the origin of GRBs [90]. A collapsing massive star [130], [131] or a binary merger [75] followed by a strong relativistic explosion are considered to be the progenitors of these violent events. Internal collisions inside the fireball of relativistic shells departing from the progenitor with different velocities, give rise to the GRB [86]. The same model attributes the afterglow emission to synchrotron radiation which is emitted during the deceleration of the external shock in the interstellar medium (ISM) [101], [140]. This behaviour can last for several days or even months after the burst covering a wide range of the spectrum. As afterglow observations improved, however, certain questions were raised that could not be answered with the standard model (see [138] for a detailed discussion). Recent observations in the optical [107], radio as well as the X-ray band [15], [76], show a strong variability in the afterglow phase for a large proportion of the bursts, which can not be reproduced by the standard external shock model.

It has been proposed that a bump in the afterglow light curve may result when the forward shock propagating in the ISM encounters a density jump, caused by an inhomogeneity of the surrounding medium generated by interstellar turbulence or by anisotropy in a precursor wind from the GRB progenitor [126], [52]. However, numerical simulations of a spherical explosion exhibit a rather canonical behaviour and even for a sharp and large increase in the external density this model does not produce sharp features in the light curve and cannot account for significant temporal variability in GRB afterglows [74], [116]. It has been suggested that a late activity of the central engine could explain the observed variability [26], [139], [92], [42].

In the late activity scenario, the central engine produces consecutive explosions after the initial burst which collide when a slow shell is followed by a faster one. This late activity of the source could be explained from a two-stage collapse in the central object. As proposed by King et al. [45] a collapsing core which has enough angular momentum to fragment will leave behind a second compact "star" in the form of a self-gravitating neutron lump. The fallback of this "star" at later times on the initial compact object can restart the central engine. Other theories suggest that the viscous hyperaccreting accretion disk around a black hole which fragments at large radii becomes dynamically unstable on different timescales and thus collapses at different times [84]. It is proposed that the region at the vicinity of the accretor can play an important role in determining the accretion rate and therefore the energy output of the explosion [88].

According to late activity models the second blast wave continuously supplies the

system with energy while colliding with the initially ejected material, producing in that way the rebrightening observed in the afterglow.

The role of magnetic fields in GRBs is still arguable. In the fireball model the presence of a magnetic field is not dynamically important for the evolution of the flow but plays an important role for the emission during the interaction of the flow with the external medium. Although the early afterglow emission strongly depends on the magnetization of the flow, in the late stages of the afterglow where the shells experience strong deceleration, the evolution of strongly magnetized shells resembles that of hydrodynamic shells and can be described by the self-similar Blandford-Mckee (BM) [10] approximation [71]. At this stage of the afterglow the emission no longer contains information about the initial magnetization of the flow.

In section 2.3 we describe the high resolution numerical simulations we performed of late collisions of two ultra-relativistic shells during the afterglow phase. We claim that differences in the flow must have an impact on the resulting light curves and perform four simulations with varying Lorentz factor and energy content of the second shell in order to investigate the effect of these parameters. The adaptive mesh refinement (AMR) technique enables us to use high resolution in long term, 1D relativistic hydro simulations, in order to capture the forward and reverse shock formation on the second shell and study in detail the stages before, during and after the merger of the two shells.

The effects of the collision between the two shells in the light curves is described in section 2.4. We study both spherical explosions as well as a hard-edged jet scenario where no lateral spreading has occured (numerical simulations in two dimensions have shown that only very modest lateral spreading occurs while the jet is relativistic [142], [36], [64]). Optical and radio on-axis light curves are calculated for different opening angles and the strength of the occuring flare or rebrightening is found to depend on this opening angle. We also note a clear difference in the shape between optical and radio light curves as well as a difference in the time of the appearance of the flare between the two frequencies. We explain this chromatic behaviour in terms of the synchrotron self-absorption mechanism and the different main contributing regions of the jet to the emission. We construct emission images for the different stages of the merger and connect the dynamical characteristics of the flow at each stage of the collision to the features in the light curves. We will discuss and summarize our results in section 2.5.

For the dynamical simulations we are using the Adaptive Mesh Refinement version of the Versatile Advection Code (MPI-AMRVAC) [44], [65] and for the light curves and emission images calculations the radiation code of van Eerten & Wijers [118].

2.3 Modeling of the multi-shell dynamics

When the initially ultra-relativistic shell ejected from the central source starts to decelerate in the interstellar medium, a forward shock is created separating the shocked ISM from the ambient ISM. As mass is swept up, the kinetic energy of the shell is transformed into kinetic and thermal energy of the shocked matter. At the same time a reverse shock is formed which crosses the shell leading to conversion of the shell's kinetic energy into thermal. The resulting shocked ISM matter ultimately follows the self-similar BM analytical solution [65]. The afterglow is nowadays widely recognized as synchrotron radiation emitted during this phase of the propagation of the shell [67].

In our model we consider that the central engine remains active even after the initial ejection of the first shell resulting in a delayed second explosion. The produced blast wave will now travel with a steady velocity into an empty medium, since most of the matter has been swept up, until it reaches the termination shock of the first shell. In this chapter we reproduce the collision process of these two shells and claim that for small opening angles the heating of the matter that happens during this phase is responsible for the appearance of the flares observed in the light curves.

2.3.1 Special relativistic hydrodynamic equations

We perform the dynamical simulations using the 1D special relativistic hydrodynamic equations in spherical coordinates and the code AMRVAC. The equations describing the motion of a relativistic fluid are given by the five conservation laws

$$(\rho u^{\mu})_{;\mu} = 0, \qquad (T^{\mu\nu})_{;\nu} = 0 \tag{2.1}$$

where $\mu, \nu = 0, 1, 2, 3$ are the indices running over the 4-dimensional spacetime, ρ is the proper rest mass density of the fluid, u^{μ} is the four-velocity and $T^{\mu\nu}$ is the stress-energy tensor given by $T^{\mu\nu} = \rho h u^{\mu} u^{\nu} + p g^{\mu\nu}$. Here with p we denote the fluid rest frame pressure, while $g^{\mu\nu}$ is the Minkowski metric tensor, as we will consider a flat spacetime at distances far from the central engine. The specific enthalpy h of the fluid is given by $h = 1 + \varepsilon + p/\rho$ where ε is the specific internal energy. Rewriting the conservation equations in vector form we have in a familiar 3+1 split the conservation laws

$$\frac{\partial U}{\partial t} + \frac{\partial F^{i}(U)}{\partial x^{i}} = 0, \quad \text{with} \quad i = 1, 2, 3. \tag{2.2}$$

The vector U is defined by the conserved variables as

$$\mathbf{U} = [D = \rho\gamma, \mathbf{S} = \rho h\gamma^2\mathbf{v}, \tau = \rho h\gamma^2 - p - D]^T, \tag{2.3}$$

and the fluxes are given by

$$\mathbf{F} = [\rho\gamma\mathbf{v}, \rho h\gamma^2\mathbf{v}\mathbf{v} + p\mathbf{I}, \rho h\gamma^2\mathbf{v} - \rho\gamma\mathbf{v}]^T, \tag{2.4}$$

where $\mathbf{v}$ is the three-velocity and $\mathbf{I}$ is the 3×3 identity matrix. The system of equations is closed by using the equation of state

$$p = (\Gamma_p - 1)\rho\varepsilon. \tag{2.5}$$

In our simulations we choose the polytropic index to be $\Gamma_p = 4/3$. This is a good approximation since most of the shocks in the cases described below are mainly relativistic or near-relativistic.

2.3.2 Initial setting

For the dynamics of the first shell we consider that the reverse shock has already crossed the shell which now decelerates in the external medium. For the purpose of this simulation we will use the Blandford & McKee (BM) approximation to describe this phase. This is a self-similar solution of a relativistic blast wave expanding in a uniform or radially varying medium. We consider the case where the explosion is assumed to be spherically symmetric and adiabatic.

In the BM model the density of the circumburst medium scales as a power law with distance $\rho_1(r) \propto r^{-k}$. For all the simulations in the present paper we will consider that the density of the circumburst medium is constant ($k = 0$), with particle number density $n_1 = 1\,\mathrm{cm}^{-3}$ and cold, with the pressure given by $p_1 = 10^{-5} n_1 m_p c^2$ chosen such that it does not dynamically affect the system. We set the Lorentz factor of the BM shock at $\Gamma_0 = 23$ at the start of the simulation placed in distance $R_0 \simeq 2.04 \times 10^{17}$ cm. Considering the decelerating radius of the BM shock $R_{dec} = (3E_0/(4\pi n_0 m_p c^2 \Gamma^2))^{1/3}$, after which the Lorentz factor of the shock starts decreasing with distance as a power law, the initial distance R_0 of the shock corresponds to a distance 3.7 times greater than the deceleration radius R_{dec} of a jet with initial Lorentz factor 100 and 7.8 times greater than the deceleration radius of a jet with initial Lorentz factor 300. The energy content of the shell is $E = 10^{52}\,\mathrm{erg}$. According to the BM model in the ultra-relativistic case the jump conditions at the BM shock are given by

$$p_2 = \frac{2}{3}\Gamma^2\rho_1, \tag{2.6}$$

$$n_2 = \frac{2\Gamma^2}{\gamma_2} n_1, \tag{2.7}$$

$$\gamma_2^2 = \frac{1}{2}\Gamma^2, \tag{2.8}$$

where index 2 denotes the shocked medium and Γ is the Lorentz factor of the shock. According to the BM model in the ultra-relativistic case, the radius of the shock at time t is given up to order $O(\Gamma^{-2})$ by

$$R(t) = ct\left(1 - \frac{1}{8\Gamma^2}\right). \tag{2.9}$$

From the jump conditions and by choosing the similarity variable to be $\chi = \left[1 + 8\Gamma^2\right](1 - r/t)$, we obtain the properties of the shocked medium

$$p_2(r,t) = \frac{2}{3}\rho_1\Gamma^2\left[\left(1 + 8\Gamma^2\right)\left(1 - \frac{r}{t}\right)\right]^{-17/12}, \tag{2.10}$$

$$\gamma_2(r,t) = \frac{1}{2}\Gamma^2\left[\left(1 + 8\Gamma^2\right)\left(1 - \frac{r}{t}\right)\right]^{-1}, \tag{2.11}$$

$$\rho_2(r,t) = \frac{2\rho_1\Gamma^2}{\gamma_2}\left[\left(1 + 8\Gamma^2\right)\left(1 - \frac{r}{t}\right)\right]^{-7/4}. \tag{2.12}$$

The total energy is then given by $E = 8\pi\rho_1\Gamma_0^2 c^5 t_0^3/17$. If the initial Lorentz factor of the simulation is fixed at Γ_0, the duration t_0 of the shock so far then follows from this equation. The initial pressure and density jumps between the BM shell and the ISM at the position of the shock are $p_2/p_1 = 10^7$ and $\rho_2/\rho_1 = 10^2$.

The second shell is uniform, cold and ultra-relativistic and placed at distance $\Delta R = 10^{14}$ cm behind the BM shell. It is therefore assumed that the shell has moved freely up to this point. Considering a duration of the second ejection event of $\Delta t = 1000$ s, the initial thickness of the shell will be $\delta = c\Delta t = 3 \times 10^{13}$ cm. The energy of the second shell is given by

$$E_{sh} = 4\pi\Gamma_{sh}^2 R_{in}^2 \delta\rho_{sh} c^2, \tag{2.13}$$

where R_{in} denotes the initial distance of the shell and ρ_{sh} and Γ_{sh} the initial density and Lorentz factor. The initial pressure is chosen as $p_{sh} = 5 \times 10^{-2}\rho_{sh}$. In our initial conditions, we vary from case to case the given parameters Γ_{sh}

Table 2.1: Properties of the second shell for each case. $\Gamma = 23$ and $E = 10^{52}$ ergs are the Lorentz factor and energy of the BM shell.

case 1	case 2	case 3	case 4
$\Gamma/\sqrt{2}$	$2\Gamma/\sqrt{2}$	$\Gamma/\sqrt{2}$	$2\Gamma/\sqrt{2}$
E	E	$2E$	$2E$

and E_{sh} which then serve to specify the shell density ρ_{sh}. The energy provided here refers to the isotropic-equivalent energy. For all cases described in this chapter we consider emission along the rotation axis of the system and that the two ejecta have the same opening angle. We also neglect the effects of lateral spreading in both dynamical and radiation calculations. As shown in [142], sideways expansion can be a very slow process and definitely negligible for times under consideration here.

We perform four simulations with varying Lorentz factor and energy for the second shell. In this simulation we are using a domain of size $[0.01, 10] \times 10^{18}$ cm and 240 cells at the coarsest level of refinement. The physical properties of the afterglow shock collision model require a large domain and a very thin second shell which demands very high resolution in order to be resolved. The maximum level of refinement is 22, leading to an effective resolution of 5.03316×10^8 cells. We force the front and the back of the uniform shell to be refined in order to avoid numerical diffusion which would cause an artificial spreading of the shell. A summary of the simulation parameters can be found in Table 1. The top left figures in Figs. 2.1 and 2.2 show the initial conditions of case 1 and 4 respectively.

2.3.3 Interaction between two shells

Jump conditions

The evolution of the two-shell system is shown in figures 2.1 and 2.2 for case 1 and case 4 respectively. In case 1 the two shells initially have the same energy and Lorentz factor. As the BM shell decelerates in the interstellar medium the second shell catches up. While the matter from the BM shell is swept up by the second shell, a forward shock is created separating the shocked matter from the unshocked. At the same time a reverse shock crosses the second shell and a contact discontinuity appears in between both shocks. At this stage the front of the second shell has split into four regions. In region 1 there is the BM matter. In region 2 there is the BM matter which has been heated by the forward shock. In region 3 there is the matter of the uniform shell that has been heated from

the propagation of the reverse shock and in region 4 there is the unshocked matter of the second shell. This is also shown for all 4 cases in Fig. 2.3 where a close-up of the second shell at early times is given.

The jump conditions at the second shell as given by [10] for an arbitrary strong shock ($p_2/n_2 \gg p_1/n_1$) are

$$e_2 = \overline{\gamma}_2 \frac{n_2}{n_1} h_1, \qquad \frac{n_2}{n_1} = 4\overline{\gamma}_2 + 3, \tag{2.14}$$

$$\frac{e_3}{n_3 m_p c^2} = \overline{\gamma}_3 - 1, \quad \frac{n_3}{n_4} = 4\overline{\gamma}_3 + 3, \tag{2.15}$$

where $\overline{\gamma}_2$ is the Lorentz factor of the fluid in region 2 relative to region 1 and $\overline{\gamma}_3$ is the Lorentz factor of the fluid in region 3 relative to region 4. The primitive variables n_i, p_i as well as the internal energy density e_i and enthalpy h_i, are measured in the fluid frame, while the Lorentz factors of the several regions, $\overline{\gamma}_i$, are measured in respect to the ISM which is considered to be at rest. In our case the forward shock of the second shell is moving in a hot medium which has already been heated by the BM shock. Therefore $h_1 = e_1 + p_1 \simeq 4p_1$, assuming the ultra-relativistic equation of state $e_1 \simeq 3p_1$.

Dynamics of the different cases

After the initial explosion and acceleration of the uniform shell, the swept up BM matter starts playing an effective role in the deceleration of this shell. In Fig. 2.3 we show snapshots of all 4 simulations taken at emission time $t_e = 6.98 \times 10^6$ s after the explosion when the forward shock, the contact discontinuity and the reverse shock are fully developed. At this time the BM matter is continuously heated by the forward shock resulting in an increase in the density of the shocked matter, $n_2/n_1 \simeq 7.10$ (case 1). The relative Lorentz factor is given by $\overline{\gamma}_2 = \gamma_2\gamma_1(1 - \sqrt{(1-\gamma_2^{-2})(1-\gamma_1^{-2})}) \sim 1.46$. A small inconsistency is observed between the simulation results and the jump conditions which derives from the fact that in all our simulations the random kinetic energy per particle at the two sides of the shock is $p_2/n_2 > p_1/n_1$ rather than $p_2/n_2 \gg p_1/n_1$. Similarly the propagation of the forward shock results in an increase of the internal energy of the shocked matter which now is $e_2 \simeq 0.61 \sim \overline{\gamma}_2 w_1 n_2/n_1$. At the same time the reverse shock crosses the shell while heating the uniform shell matter and transforming the kinetic energy of the shell into thermal. The contact discontinuity separating the two regions appears as a density jump between the two shocked fluids, $n_3/n_2 \simeq 10^2$ while the Lorentz factor and pressure remain continuous, $\gamma_2 = \gamma_3$ and $p_2 = p_3$. The efficiency of this energy transformation

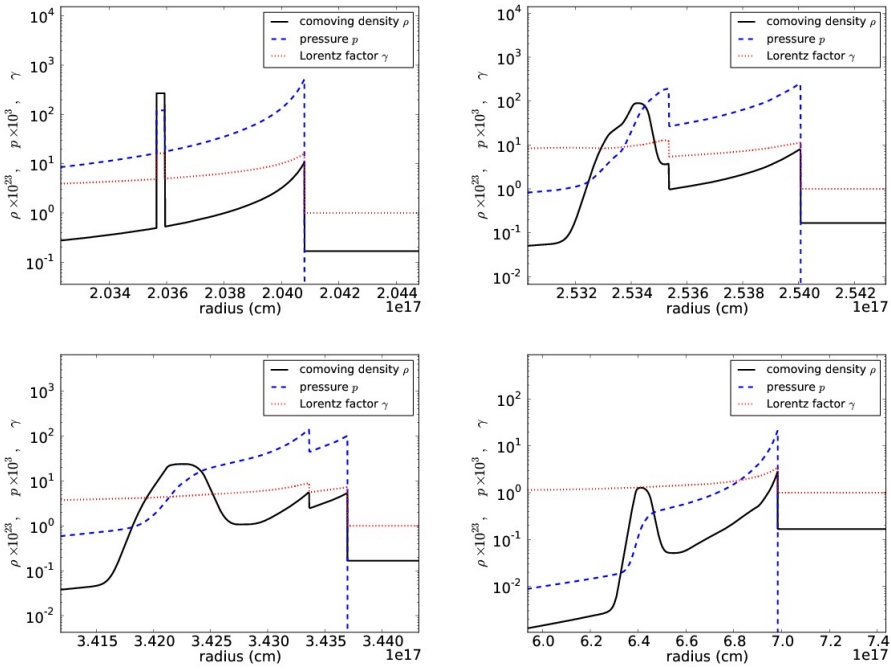

Figure 2.1: Snapshots of the dynamics for case 1, taken at local emission times $t_e = 6.81 \times 10^6$ s, $t_e = 8.48 \times 10^6$ s, $t_e = 1.15 \times 10^7$ s and $t_e = 2.35 \times 10^7$ s after the initial explosion (top left - bottom right). Lorentz factor, density and pressure are indicated as the dotted, solid, and dashed line. The top-left figure indicates the initial setting of our simulation.

mechanism is highly dependent on the reverse shock itself. According to Sari & Piran (1995) the reverse shock depends only on two parameters, the Lorentz factor of the unshocked shell material relative to the BM unshocked matter, $\overline{\gamma}_4$, and the density jump, n_4/n_1. For $\overline{\gamma}_4^2 \gg n_4/n_1$ the reverse shock will be relativistic, $\overline{\gamma}_3 \gg 1$. For case 1, at emission time $t_e = 6.98 \times 10^6$ s. (Fig. 2.3), the reverse shock remains Newtonian ($\overline{\gamma}_3 = 1.00484$) while propagating into the shell and thus insufficient to heat the shell effectively. Following this behaviour, by the time the reverse shock reaches the back of the shell, the shell is still dominated by its kinetic energy although significantly decelerated (see also Fig. 2.1).

We follow the same analysis for case 2 in which we double the Lorentz factor of the second shell compared to case 1. Since we choose to maintain constant the

energy and the thickness of the second shell, the change in the Lorentz factor affects the density of the second shell, which is now smaller by a factor of 4 compared to case 1 (eq. 2.13). Comparing the properties of the flow for the two cases at similar times after the explosion we notice that the forward shock is stronger in case 2. Specifically at emission time $t_e = 6.98 \times 10^6$ s after the explosion the forward shock has a Lorentz factor relative to the BM matter $\overline{\gamma}_2 = 1.99$ and the number density satisfies $n_2/n_1 \simeq 7.67$. That shows that the forward shock is more efficient in the second case as it compresses the matter of the BM shell to a higher degree and to higher Lorentz factor than in case 1. At the same time the reverse shock is stronger than in case 1, $\overline{\gamma}_3 = 1.16$ and although it is not ultrarelativistic it is more efficient in converting the kinetic energy of the second shell into thermal. That appears clearly as a difference in the pressure between the shocked and unshocked shell matter, $p_3/p_4 = 12.27$ for case 2 compared to $p_3/p_4 = 1.78$ for case 1.

In case 3 we double the energy of the second shell. The relevant Lorentz factor between the shocked and unshocked BM matter is $\overline{\gamma}_2 \simeq 1.75$ and the density jump satisfies $n_2/n_1 \simeq 6.69$. Compared to case 1 the reverse shock for this case remains very weak, $\overline{\gamma}_3 \simeq 1.00013$, while propagating in the uniform shell since it has to traverse a denser medium than before, leading to a compression ratio between the shocked and the unshocked shell matter $p_3/p_4 = 1.09$. In case 4 we double both the energy and Lorentz factor of the second shell. The initially very fast shell leads to a strong forward shock, $\overline{\gamma}_2 \simeq 2.26$. The reverse shock is now stronger compared to case 3, $\overline{\gamma}_3 \simeq 1.15$, compressing the shocked shell matter to higher pressure, $p_3/p_4 = 7.98$.

In figure 2.3 we plot the thermal to mass energy ratio together with Lorentz factor, density and pressure for fixed early time for all cases. We observe that as matter from the BM shell is swept up from the forward shock of the second shell, the thermal energy of the fluid increases compared to the mass energy (which appears as a small bump in the thermal to mass energy curve at the position of the forward shock). While the shell gets traversed by the reverse shock, part of the kinetic energy of the shell is transformed into thermal as a result of the propagation of the reverse shock. We notice that the relativistic reverse shock in case 2 is a lot more efficient in raising the thermal energy component than in case 1. In case 3 and 4 a similar behaviour is observed. By increasing the energy in case 3 and with the Lorentz factor being the same as in case 1, the density becomes higher in the shell as seen from equation 2.13. As a result the reverse shock is very weak and highly inefficient in thermalizing the cold shell. In case 4 both the energy and the Lorentz factor of the second shell have twice the value compared to case 1. In this case the reverse shock is propagating in a less dense medium compared to case 3 and is now more efficient in transforming the kinetic energy of the second shell into thermal (Fig. 2.3). The Lorentz

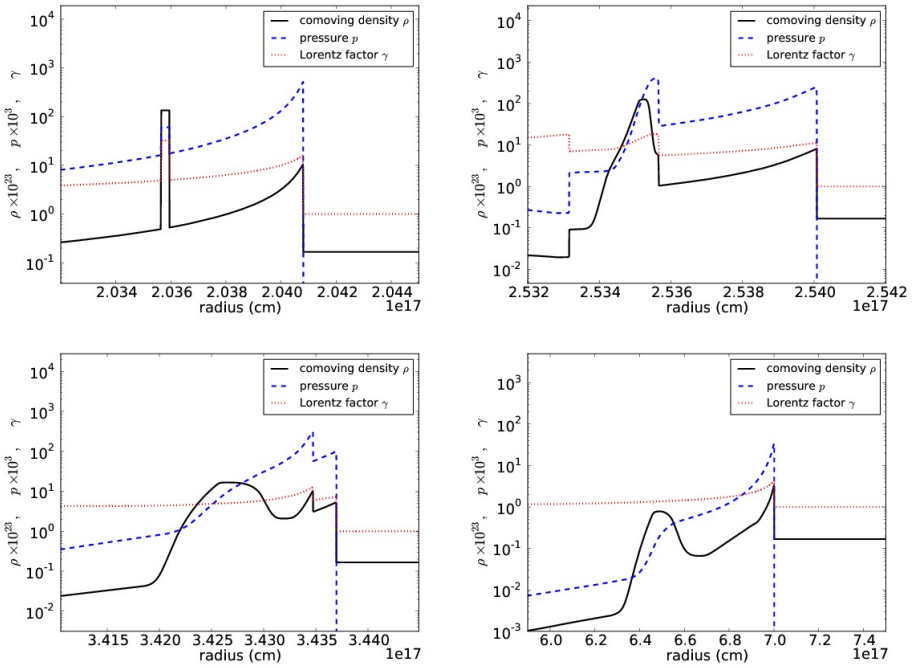

Figure 2.2: Snapshots of the dynamics for case 4, taken at local emission times $t_e = 6.81 \times 10^6$ s, $t_e = 8.48 \times 10^6$ s, $t_e = 1.15 \times 10^7$ s and $t_e = 2.35 \times 10^7$ s after the initial explosion (top left - bottom right). Lorentz factor, density and pressure are indicated as the dotted, solid, and dashed line. The top-left figure indicates the initial setting of our simulation.

factor of the reverse shock is slightly overestimated as a result of our use of a fixed adiabatic index of 4/3 throughout the domain. Nevertheless, as we see from Fig. 2.3, the fluid is highly relativistic from the contact discontinuity of the second shell onward and therefore the regions that mostly contribute to the observed flux (see next section) are appropriately described by a fixed adiabatic index.

Later, at emission time $t_e = 1.513 \times 10^7$ s (see Figs. 2.1 and 2.2), the forward shock will catch up and overcome the BM shell as the latter one decelerates in the ISM. As the forward shocks merge and the reverse shock has crossed the back of the shell, a dense but slow and underpressured region is left behind unable to follow the forward shock as it has lost almost all of its kinetic energy reaching a near-equilibrium state with the surrounding matter.

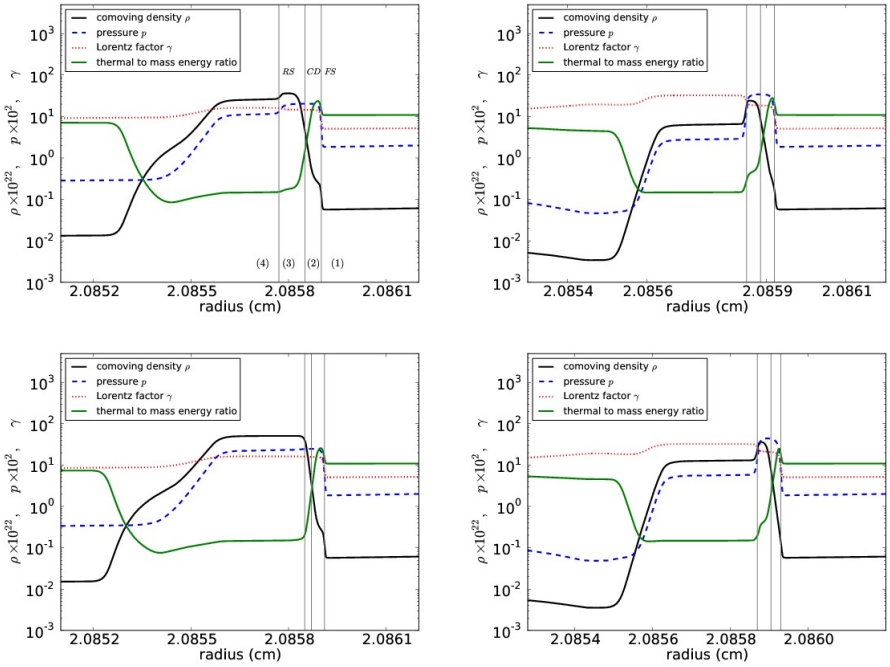

Figure 2.3: Ratio of thermal to mass energy ($E_{th}/(\rho c^2)$) and normalized Lorentz factor, density and pressure for case 1 to case 4 (top left to bottom right) for the second shell at emission time $t_e = 6.98 \times 10^6$ s. Distance is normalized to 10^{17} cm. For cases 1 and 2 the transformation from thermal to kinetic energy is clear at the forward shock as well as the kinetic to thermal energy transformation at the position of the reverse shock. The ratio depends strongly on the properties of the second shell. The four regions of interaction between the two shells are indicated on the figure for case 1. Region (1) consists of the unshocked BM matter, region (2) of the shocked BM matter, region (3) of the shocked uniform shell matter and region (4) of the unshocked uniform shell matter. We focus on the front of the second shell, the dynamical evolution of which plays an important role on the light curves.

2.4 Radiation calculations

In this section we describe the numerical calculations we performed in order to construct the light curves at the afterglow phase. The following calculations were carried out with the radiation code introduced in [118] and [115]. The main process contributing to the afterglow is synchrotron radiation. In both external and internal shock collision models, a magnetic field is required in order to fit the observational data. This magnetic field is most likely generated by instabilities forming in the shock such as the relativistic two-stream instability or the Weibel instability [61], [127]. In this case a fraction of the total thermal energy behind the shock goes to particle acceleration and another one to the generation of the magnetic field. Assuming that the fractions of the thermal energy density e_{th}, contributing to the magnetic energy density, ϵ_B, and electron energy density, ϵ_E, have a fixed value, we can calculate the afterglow emission. In our calculations we neglect the effect of the magnetic fields and radiative losses on the dynamics and do not take into account the effects of Compton scattering and electron cooling (that play a negligible role at times and frequencies under consideration). We do however include the effect of synchrotron self-absorption (ssa) due to the re-absorption of the radiation from the synchrotron electrons by solving simultaneously the linear radiative transfer equations for a large number of rays through the evolving fluid. An analytical formula for obtaining the self-absorption frequency ν_{sa} can be found in [39].

The radiation code is specifically written to include the snapshots produced by the dynamical simulations performed with MPI-AMRVAC. In all our calculations the values of ϵ_B and ϵ_E are fixed to 0.01 and 0.1 respectively and we assume a power law distribution for the accelerated electrons with $p = 2.5$. We also fix the fraction of the electrons accelerated to this power law distribution ξ_N equal to 0.1. Assuming isotropic radiation in the comoving frame, the observer's flux calculated by the radiation code is given by

$$F_\nu = \frac{1+z}{d_L^2} \int \frac{d^2 P_V}{d\nu d\Omega}(1-\beta\mu) c dA dt_e, \tag{2.16}$$

in the optically thin limit, where for the purpose of our simulations the redshift z is chosen to be zero. Here d_L denotes the observer luminosity distance, β the fluid velocity in units of c, $d^2P_V/d\nu d\Omega$ is the received power per unit volume, frequency and solid angle and $\mu = \cos\theta$, with θ being the angle between the fluid velocity and the line of sight. The surface element dA corresponds to an equidistant surface A, which is a surface intersecting the fluid grid from which the radiation arrives at the observer at time t_{obs}. Each surface corresponds

to a specific emission time t_e. For a photon emitted from a location (r,θ) at emission time t_e, the observer time is given by

$$t_{obs} = t_e - \frac{r\mu}{c}. \tag{2.17}$$

When electron cooling does not play a role, the shape of the observed spectrum follows directly from the dimensionless function $Q(\nu/\nu_m)$ which has the limiting behaviour $Q \propto (\nu/\nu_m)^{1/3}$ for small (ν/ν_m) and $Q \propto (\nu/\nu_m)^{(1-p)/2}$ for large (ν/ν_m). The received power depends on this shape and on the local fluid quantities via

$$\frac{d^2P_V}{d\nu d\Omega} \propto \frac{\xi_N n B'}{\gamma^3(1-\beta\mu)^3} Q\left(\frac{\nu}{\nu_m}\right), \tag{2.18}$$

where n is the lab frame number density of the electrons and B' is the comoving magnetic field strength. The synchrotron peak frequency ν_m corresponds to the Lorentz factor of the lower cut-off of the accelerated electron's power-law distribution γ_m, assuming that the Lorentz factor for the upper cut-off goes to infinity. Then the lower cut-off for the electrons will relate to the comoving number density n' and thermal energy density e'_{th} via

$$\gamma_m \propto \left(\frac{p-2}{p-1}\right) \frac{\epsilon_E e'_{th}}{\xi_N n'}. \tag{2.19}$$

The particle distribution and its lower cut-off are set at the shock front. However, subsequent evolution of γ_m is dictated by adiabatic expansion of the fluid rather than synchrotron radiative losses. Therefore, in a relativistic fluid, eq. (2.19) also holds further from the shock front with the same value of ϵ_E.

The temporal behaviour of several GRBs contradicts the spherical explosion senario. A rapidly decaying afterglow emission suggests that the flow must be collimated rather than spherical. This is vital for the GRB mechanism since a spherical expansion would require a total energy budget $\sim 10^{54}$ ergs which is hard to produce from a stellar mass progenitor, while a jet shaped explosion can have the same result with less energy, $\sim 10^{51} - 10^{52}$ ergs. This model suggests that when the jet decelerates to Lorentz factors such that $\gamma \sim \theta_0^{-1}$ is satisfied, with θ_0 being the half jet opening angle, the flux that the observer receives will start decreasing resulting to a break in the afterglow light curves. In contrast to AGN jets that can be directly observed, GRB jets are only implicitly assumed from this break.

In our simulations we construct optical and radio light curves and emission images at various times for the 4 cases described above. We try different opening

angles of the jet and associate the flare characteristics with the jet opening angle.

The main characteristic of our approach is the separation of the dynamics from the radiation simulation. The outputs from the dynamical simulations are used as an input to the radiation code in order to calculate synchrotron emission. When absorption plays a role, the code solves a series of linear radiative transfer equations (rather than equation 2.16 directly) along the light rays starting from the back of the jet and passing through the jet towards the observer. For given emission time t_e a surface on the radiative volume of the jet exists from which emission arrives at the observer at time t_{obs}. A summation over the light rays along this *equidistant surface*, and an integration over all the *equidistant surfaces* is applied in order to calculate the contribution to the emission of every part of the jet. The observed flux is obtained by summing over the rays emerging from the jet. When the rays are not summed over, a spatially resolved emission image of the two shell system is obtained. An adaptive procedure similar to the one used in MPI-AMRVAC is employed when more rays need to be calculated in order to adequately capture the emission from the underlying fluid profile. More details on the radiation code algorithmic strategy can be found in [118],[115].

2.4.1 Early afterglow and jet break estimation

The dynamical simulations cover a timescale starting from 0.072 days and ending 10 days after the initial explosion in the observer's time frame. In order to include the initial stages of the afterglow in our simulation we assume that prior to the simulation the outer shock has evolved according to BM and the second has moved with a constant velocity while retaining its initial shape. In this way the deceleration of the initial explosion is taken into account resulting in the appearance of the jet break in the light curve.

Due to relativistic beaming the emission that reaches the observer is limited to emission angles $\theta < \gamma^{-1}$. During the afterglow phase however the flow is significantly decelerated and thus larger emission angles can be observed. When the Lorentz factor becomes small enough so that the condition $\theta_0 \sim \gamma^{-1}$ is satisfied, where θ_0 is the half opening angle of the jet, the observation cone becomes big enough for the edges of the jet to become visible to the observer. When there is no significant spreading of the matter at the edges only part of the visible region is occupied by the jet and thus from this point after the flux will start decaying faster. This transition to the faster decaying part of the light curve is often referred to as the jet break.

Table 2.2: Observer time estimation of the jet break (estimation made in days after the explosion) for the four simulated cases assuming two hard-edged jet scenarios.

Jet break estimation				
	case 1	case 2	case 3	case 4
$2\theta_0 = 2$	0.0028	0.0028	0.0035	0.0035
$2\theta_0 = 5$	0.032	0.032	0.041	0.041

An analytical formula given in [117] gives an estimation of the observed jet break time, $t_{obs,br}$ depending on the total energy of the explosion E, the half opening angle θ_0 of the jet, the circumburst density n_0 and profile k. The contributing area to the emission in this case is not only the shock front itself but also the area behind the shock. For that purpose the radial profile from the BM model has been used, and the formula reads

$$t_{obs,br} = \theta_0^{2+2/(3-k)} \left(\frac{A_1}{2(1+2(4-k))} \right)^{1/(3-k)} \times \left(\frac{1}{2} + \frac{1}{2(1+2(4-k))} + \frac{1}{2(4-k)2(1+2(4-k))} \right) \tag{2.20}$$

where k corresponds to the parameter defining the power-law of the circumburst medium density, which for our case is always set to 0, and A_1 a parameter of the fluid depending on the energy E of the explosion and the number density at the position of the shock, $A_1 = E(17-4k)/(8\pi m_p n_0 R_0^k c^{5-k})$ with n_0 being the proton number density at distance R_0.

The jet break observer time estimation $t_{obs,br}$, is presented in Table 2.2 for all the cases we simulate and for two different opening angles of the jet. As expected, when the total energy of the explosion remains the same, the jet break time remains the same even if the Lorentz factor of the second shell is different. For larger opening angles of the jet the jet break is observed at later observer times as it takes longer for the shell to decelerate to Lorentz factors such that $\theta_0 \sim \gamma^{-1}$ condition is satisfied. We discuss the jet break characteristics further in subsection 2.4.4.

In our model the interaction between the two shells starts happening after the jet break has occured, leading to a rebrightening of the afterglow and a sudden increase in the flux. The shape of the light curve and the characteristics of the

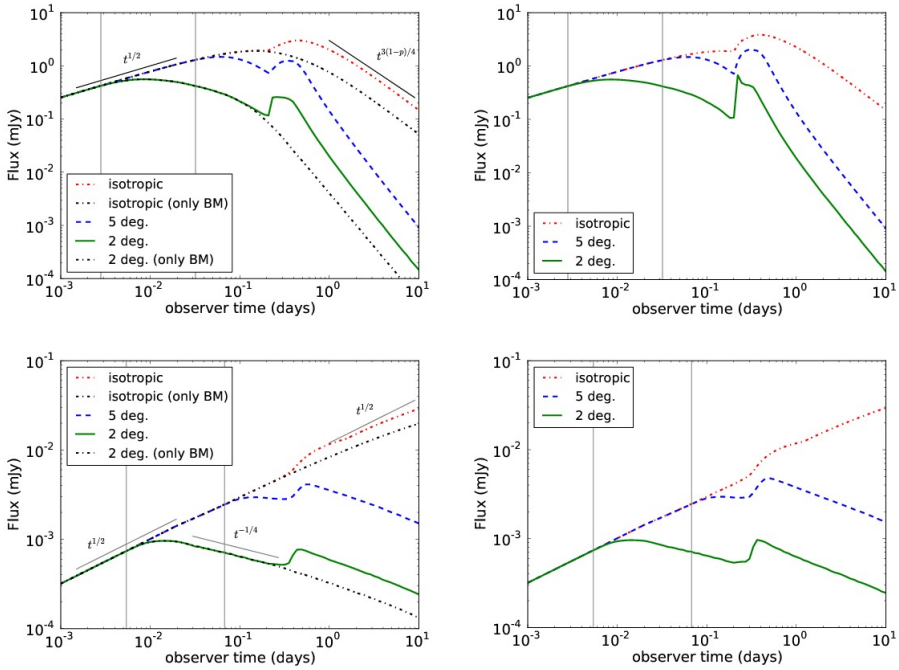

Figure 2.4: Optical (top) and radio (bottom) light curves for case 1 (left) and case 2 (right) for different values of the jet opening angle $2\theta_0$. In all cases an increase of the flux due to energy injection from the second shell is observed. For small opening angles a flare appears in all four simulated cases which differs in shape according to the frequency. The peak flux is greater the higher the Lorentz factor and energy of the second shell are. The jet break estimation is denoted with a vertical line for both 2 and 5 degree jets. For case 1 we overplot the light curves produced for a single BM shell for a spherical explosion and a 2 degrees hard-edged jet. The analytical estimation of the slope is shown above the optical and radio light curves.

emission are subjected to the dynamics of the flow and present qualitative and quantitative differences from case to case.

2.4.2 Optical and radio light curves

For the four cases described in section 2.3 we produce optical and radio light curves. We examine each case assuming different opening angles of the jet. In

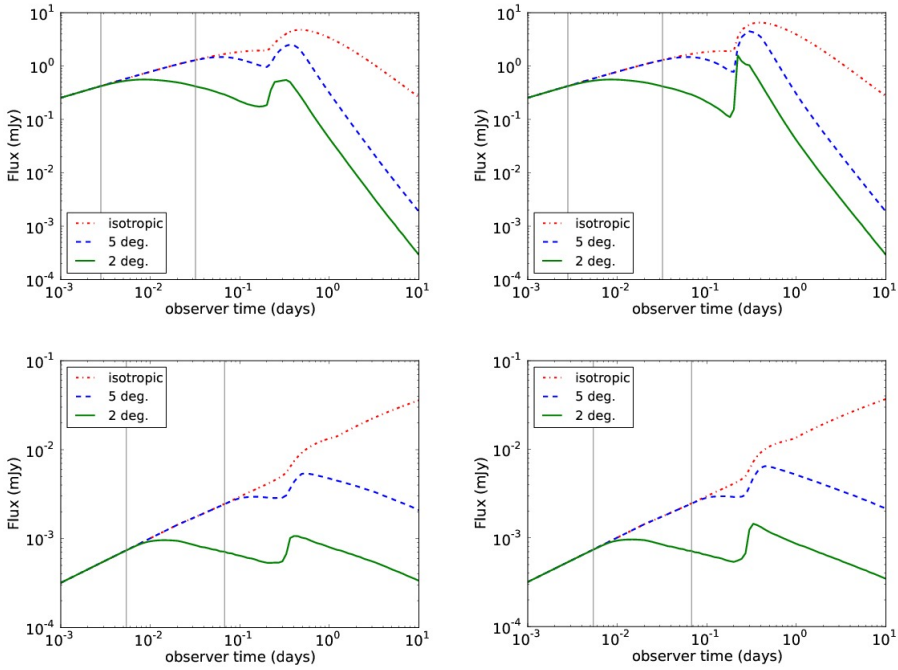

Figure 2.5: Optical (top) and radio (bottom) light curves for case 3 (left) and case 4 (right) for different values of the jet opening angle $2\theta_0$. In all cases an increase of the flux due to energy injection from the second shell is observed. For small opening angles a flare appears in all four simulated cases which differs in shape according to the frequency. The peak flux is greater the higher the Lorentz factor and energy of the second shell are. The jet break estimation is denoted with a vertical line for both 2 and 5 degree jets.

Figure 2.4 and 2.5 we present the light curves produced by the radiation code for spherical and collimated expansion of the two colliding shells.

A rebrightening of the optical light curve is observed for $t_{obs} = 0.2$ days for the spherical explosion in case 1 (Fig. 2.4), which is attributed to the interaction of the two shells when the second one reaches the back of the BM shell. We find that the smaller the opening angle of the jet, the steeper the rise of the flare. This can be understood from the fact that for a jet with small opening angle there is, at a given observer time, less emission still arriving from earlier emission times and higher emission angles. As we show in section 3.5 (Figures 2.9, 2.10) early emission time contribution comes from high emission angles on

the jet, thus the features of the light curve are less smeared out for a collimated outflow.

This can also explain the difference we observe in the decreasing rate of the flux at late observer times. Since there is no contribution from early emission times, the flux for a jetted outflow will decline faster compared to a spherical explosion. We also observe that the flare is sharper in case 2 compared to case 1 and in case 4 compared to all four cases (Fig. 2.4 and 2.5). This confirms our hypothesis that the flare is strongly dependent on the dynamical properties of the collision. For case 2, where the forward and reverse shock of the second shell are significantly stronger compared to case 1 (Fig. 2.3), the change in the flux during the collision of the two shells appears substantially stronger. In cases 3 and 4 we observe the same behaviour in the light curves. In case 4, the higher Lorentz factor together with the higher energy imposed in the second shell, lead to a flare clearly stronger compared to all the other cases for a 2 degrees opening angle of the jet. In that case the timescale of the variation for the flare is $\Delta T/T = 1.08$ days for the optical and $\Delta T/T = 1.90$ days for the radio, where ΔT is calculated as the full width at half maximum of the flare and T is the observer time of the peak. The relative flux increase with respect to the underlying afterglow is $\Delta F/F = 3.95$ for the optical and $\Delta F/F = 1.04$ for the radio which is significantly reduced due to ssa mechanism. Although extensive comparison to observational data is beyond the scope of this work, we note that this case resembles the afterglow of GRB 060206 which shows an increase in brightness by ~ 1 mag 1 hr after the burst, followed by a typical broken power-law decay [107], [133].

Before and after the flares the resulting light curves follow the analytically predicted slopes for a single forward shock as shown in Fig 2.4. The light curves at a given frequency depend on the temporal evolution of the characteristic frequencies of the system, that is in our case the synchrotron peak frequency ν_m and the self-absorption frequency ν_{sa}. As described in [40] these slopes read $t^{1/2}$ for times before the break frequency ν_m, crosses the observed frequency ν and $t^{3(1-p)/4}$ for the time after. In addition to this behaviour the slope of the light curve steepens by $t^{-3/4}$ after the jet break, in both optical and radio frequency, for small opening angles of the jet. This steepening appears clearer in the radio ($t_{obs,br} = 0.0054$ days for 2 degree jet and $t_{obs,br} = 0.068$ days for 5 degree jet) where the emission comes from late emission times and lower emission angles close to the jet axis. In the optical, where earlier emission times also contribute to the observed flux (as discussed in section 2.4.5 and shown in Fig. 2.9 and 2.10), this steepening is delayed and appears at $t_{obs} = 0.075$ days almost at the same time as the break frequency ν_m crosses the optical band.

Throughout our calculations and for all cases the critical frequencies satisfy $\nu_c > \nu_{obs}$, $\nu_c > \nu_m$ and $\nu_c \gg \nu_{sa}$ at the BM shock and the forward shock

of the second shell, where ν_c is the cooling frequency (all critical frequencies are calculated using the formulas found in Table 2 of [40] for a BM solution. Between t_{obs} of 0.001 and 10 days, ν_c decreases from 10^{20} Hz to 10^{17} Hz, while ν_m decreases from 10^{16} Hz to 10^{10} Hz for the BM shock of case 1). Hence, for the frequencies discussed in the present work we are always in the slow cooling regime. In addition to the fact that the shock regions forming at the second shell are a lot thinner than a typical BM profile, this allows us to neglect, with small error, the effect of synchrotron cooling on the electron distribution for the times under consideration and consequently any changes on the self-absorption coefficient.

Furthermore our assumption that inverse Compton (IC) doesn't influence the observed spectrum is confirmed as follows. There are two ways in which IC scattering can change the overall synchrotron spectral component. First by producing an additional emission component at high frequencies and second by dominating the electron cooling and thus reducing the available energy for synchrotron radiation. As discussed in [97], the first is estimated by considering the ratio of specific fluxes measured at the peak of the respective flux components, f_{max} for the synchrotron and f_{max}^{IC} for the IC respectively. Then this ratio is $f_{max}^{IC}/f_{max} \sim 1/3\sigma_T nR$, where σ_T is the Thompson cross-section and n the electron density at distance R. This ratio remains well below unity for all the shock surfaces in all four simulations which are taken into consideration. The second factor can be estimated directly from the ratio $\eta\epsilon_E/\epsilon_B$. As shown by Sari & Esin [97], the IC cooling rate will be unimportant compared to synchrotron if $\eta\epsilon_E/\epsilon_B \ll 1$, where $\eta = (\gamma_c/\gamma_m)^{2-p} = (\nu_c/\nu_m)^{-(p-2)/2}$. In our case this ratio is close to unity for the early afterglow but decreases rapidly and remains below unity during our simulation covering the pre and post flaring activity period.

2.4.3 The shape of the optical flare

The flaring activity as observed in the optical follows three stages. At the first stage the Lorentz factor and the thermal energy of the BM matter in front of the second shell increase due to the propagation of the forward shock leading to the sudden rise of the flux. The flare observed in Fig. 2.4 and 2.5, is attributed to that increase. This behaviour continues until $t_{obs} = 0.23$ days when the reverse shock crosses the back of the second shell. At that time the forward shock starts decelerating and that can be seen as a reduction of the flux, after the initial peak, in the optical light curves. At time $t_{obs} = 0.25$ days the shocked BM matter has separated from the shell and now propagates in the BM shell while constantly heating the swept up matter. The flux for that stage of the motion remains almost constant in the optical light curve as the density in front of the forward shock continuously increases and the heated matter compensates

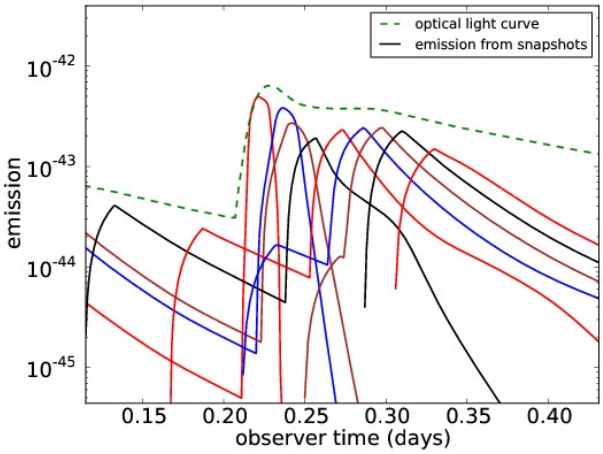

Figure 2.6: Optical light curve and single emission images for several snapshots of the two shell system for case 4. The emission time of the snapshots range from $t_e = 7.64 \times 10^6$ s for snapshot 50 to $t_e = 1.26 \times 10^7$ s for snapshot 350.

in the flux for the deceleration of the forward shock. This remains until the forward shock of the second shell and the BM shell merge at time $t_{obs} = 0.31$ days. At that time the optical light curve presents a change in the slope and the flux starts decreasing as the emission now originates from the merged shell while propagating into the ISM.

In figure 2.6 we plot the optical light curve for case 4 considering a hard-edged jet with opening angle $2\theta_h = 2$ during the period of the flare and the emission from several snapshots before, after and during the collision of the two shells. The emission from each snapshot consists of a BM shell contribution which peaks at early observer times and the contribution from the second shell which peaks during the flare and at later times. A comparison between the light curve and the emission snapshots shows that immediately after the forward shock of the second shell is created the flare is observed ($t_e = 7.64 \times 10^6$ s). The stage of the forward shock deceleration and the flux reduction can be seen from $t_e = 7.64 \times 10^6$ to $t_e = 1.01 \times 10^7$ s. As soon as the forward shock separates from the second shell, the shape of the emission arising from the forward shock becomes sharper ($t_e = 1.05 \times 10^7$ s). The third stage of the flare where the forward shock propagates inside the BM matter shapes the plateau which is observed from $t_{obs} = 0.25$ to $t_{obs} = 0.31$ days and can be seen from $t_e = 1.05 \times 10^7$ to $t_e = 1.26 \times 10^7$ s. At that emission time the merger of the two shells has almost completed and the flux starts decaying.

2.4.4 Time delay observed between optical and radio flares

Comparing the optical to the radio light curves, we notice that the flaring activity occurs with a distinct time delay (approximately 0.1 days) for the latter ones (Fig. 2.7). The reason for this is the ssa mechanism. For optical emission the jet is optically thin and the contribution from the second shell is obtained as soon as the forward shock is created while propagating in the BM shell. Below the self-absorption frequency though the jet behaves differently. In the radio the jet is optically thick due to ssa mechanism and the merger becomes visible only after the collision has nearly completed. This results in observing the plateau at the second stage of the optical flare and a sharp peak in the radio flare. This highlights the significance of taking into account ssa when calculating radio light curves. In fact any variability resulting from changes in the fluid conditions may manifest in a chromatic fashion [117]. For that reason the jet break is significantly postponed in the radio light curves (Figs. 2.4 and 2.5).

2.4.5 Emission images

By directly plotting the relative contributions to the light curve from different parts of the fluid, the reasons for the differences between radio and optical light curves become even more obvious. The flux at a given observer time is obtained by solving the linear radiative transfer equation through the evolving fluid for a large set of rays. By separately storing the local contributions to the emerging rays, we have created emission images showing exactly the relative contributions of different parts of the jet. We produce emission images for different observer time and opening angle, for optical (5×10^{14} Hz) and radio (10^8 Hz) frequencies covering the time before, during and after the flaring activity is observed. In all the images the jet axis is aligned to the horizontal direction and the observer is at the right end of the horizontal axis. Which area of the jet is the main contributing area to the emission is strongly frequency dependent. When the frequency of observation lies well above the self absorption frequency, the system is optically thin and the main contribution to the emission is from early emission times and from high emission angles on the jet. For lower frequencies the system becomes optically thick due to self absorption, hence the main contribution to the emission is from later emission times and the emitting region shifts to lower emission angles closer to the jet axis. This behaviour is observed throughout the figures 2.8-2.10, where we plot the ring-integrated, absorption-corrected local emission coefficients, as a difference in the contrast between optical and radio emission. The emission coefficient j_ν is defined as the power per unit frequency and solid angle, $j_\nu \equiv d^2P_V/d\nu d\Omega$ (see eq. 2.18). In these figures j_ν is

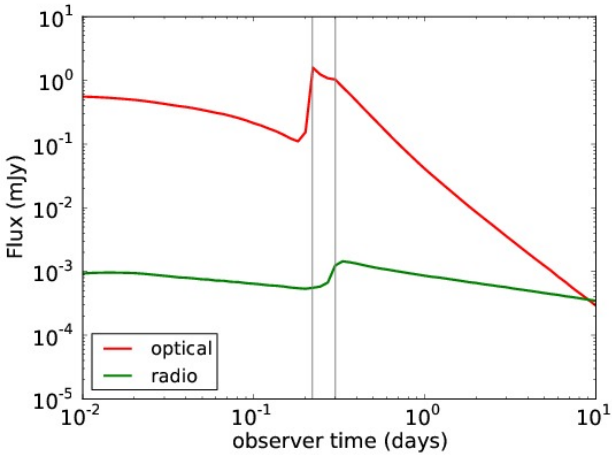

Figure 2.7: Optical and radio light curve comparison for case 4, assuming a jet opening angle $2\theta_h = 2$. The optical flare precedes the radio one by 0.1 days. The three different stages of the flare evolution can be seen on the optical flare.

corrected for optical depth (τ) and multiplied by $2\pi h$ (where h is the distance to the jet axis) in order to show more clearly the relative contributions from different angles, so the plotted quantity is $j_\nu 2\pi h e^{-\tau}$.

In Fig. 2.8 we plot the optical and radio emission images at observer time $t_{obs} = 10$ days, long after the merger has completed, for case 4 for a spherical explosion and for a hard-edged jet of opening angle $2\theta_h = 2$. We observe that different parts of the merged shell contribute to different parts of the spectrum. The optical contribution emerges mainly from high emission angles of the merged shell whereas radio emission comes mainly from lower emission angles close to the jet axis. This behaviour is also encountered in the emission images derived for the hard-edged jet. In this case, high emission angles are excluded from the calculation of the emission, which affects the optical more strongly than the radio emission. A contribution from the remainder of the second shell is observed at the radio emission image of the spherical explosion. Although significantly reduced due to ssa and almost two orders of magnitude less than the emission originating from the merged shell, this contribution owes its existence to the traverse of the reverse shock (Fig. 2.8). As the reverse shock crosses the second shell the Lorentz factor decreases, and by time $t_{obs} = 10$ days, when the shell has been significantly decelerated, the peak frequency of the synchrotron spectrum originating from that region is shifted to lower frequencies. The stronger the reverse shock the stronger the deceleration of the

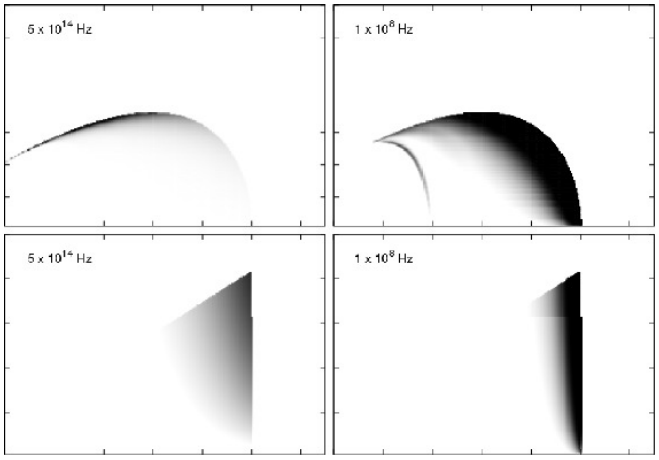

Figure 2.8: Optical 5×10^{14} Hz, (left) and radio 10^8 Hz (right) emission image in case 4 at time $t_{obs} = 10$ days. The upper pictures correspond to a spherical explosion and the lower ones to a jet with opening angle $2\theta_h = 2$. The horizontal axis scales from 2×10^{17} to 1.5×10^{18} cm and the vertical from 5×10^{15} to 3.5×10^{16} cm. The main contribution area for the optical image comes from higher emission angles while for the radio image lower emission angles contribute the most. For a hard-edged jet (lower graphs) the radio image appears stronger, since the main contribution area to the optical at the back of the jet is not taken into account. The remainder of the second shell significantly heated after the traverse of the reverse shock reveals its contribution to the radio image.

shell. The contribution of the second shell is therefore expected to be higher.

In Fig. 2.9 we show the evolution of the two shells before, during and after the collision phase for case 2, for both radio and optical frequencies assuming opening angles of the jet 2 and 20 degrees (rather than 5, to better capture high-angle emission and illustrate the contrast between narrow and wide jets). The collision appears between observer times $t_{obs} = 0.28$ and $t_{obs} = 0.35$ days which verifies that the break in the light curves occurs at the same time as the collision of the two shells. From the emission images it becomes clear that the smearing out of the flare from early emission time contribution becomes less the smaller the opening angle of the jet is. Comparing the two different cases in figure 2.9 (case 2) and figure 2.10 (case 4) it is evident that in the optical case and for large opening angles, early time contribution dominates the emission and drowns out the flaring activity. For small opening angles this effect is suppressed revealing this way the contribution of the second shell while it collides with the BM shell. In the radio emission images, where the main

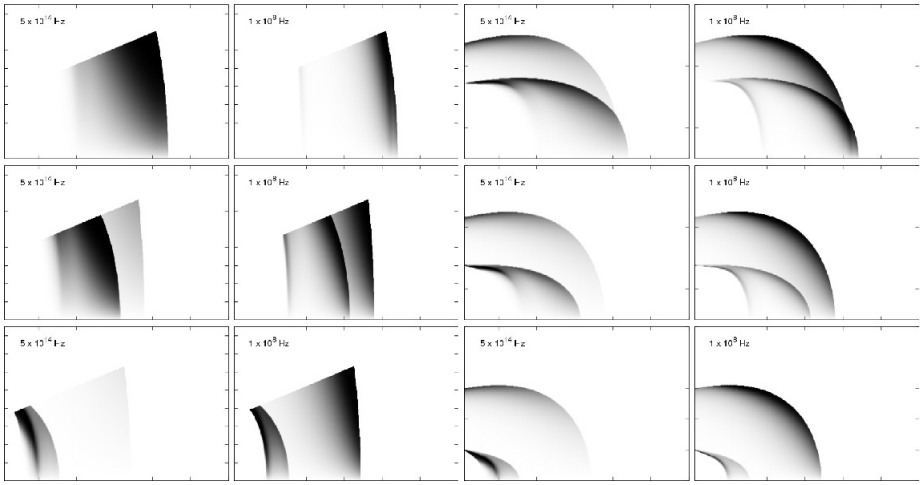

Figure 2.9: Optical (5×10^{14} Hz) and radio (10^8 Hz) emission images of the two-shell system during the flaring activity for case 2 and jet opening angle 2 degrees (top figures) and 20 degrees (bottom figures). The horizontal axis scales from 2×10^{17} to 5×10^{17} cm and the vertical from 2×10^{13} to 8.5×10^{15} cm for the 2 degrees jet and from 2×10^{13} to 2.5×10^{16} cm for the 20 degrees jet. For each subfigure the bottom images correspond to $t_{obs} = 0.23$ days, which is the time the sudden rise of the flux is observed, the middle ones to the weak decay at $t_{obs} = 0.28$ days corresponding to the propagation of the forward shock into the BM medium, and the top ones to the fast decay at $t_{obs} = 0.35$ days, once the merger has completed.

contributing area to the emission is transferred to lower emission angles, we do not observe this behaviour. Instead as described in section 3.2, in the radio frequency the jet is optically thick due to ssa mechanism and the merger can be seen only when the collision has almost completed. This difference in behaviour between optical and radio, manifests itself as a sharp rise in the radio light curve and a plateau at the flare in the optical light curve (see also Fig. 2.7).

From the emission images in fig. 2.9 and for a jet with an opening angle 20 degrees we derive the conclusion that for higher frequencies (optical, X-rays), for which the main contributing region to the observed flux shifts to higher emission angles on the jet, a double ring shaped image should appear in GRB late afterglow observations. In this type of image the inner ring carries information from the forward shock emission of the second shell, whereas the outer ring is determined from the emission at earlier stages of the forward shell. For radio frequencies where the observed flux arrives mainly from emission angles close

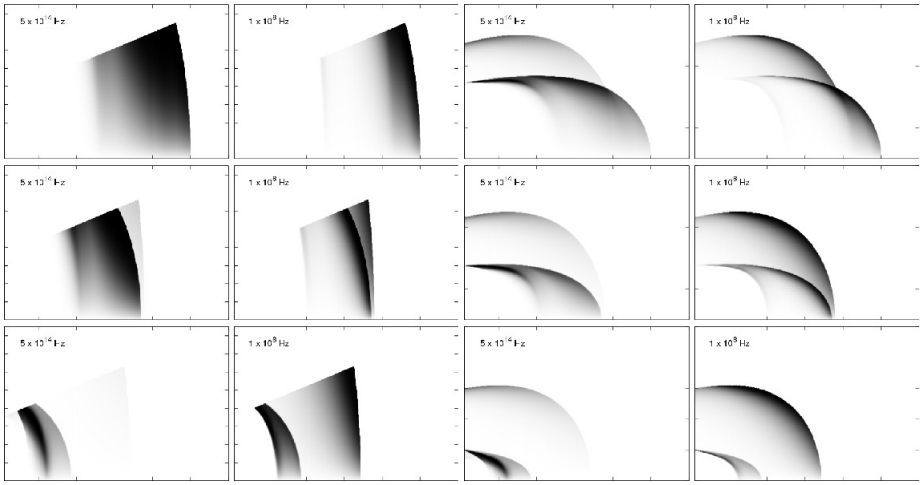

Figure 2.10: Optical (5×10^{14} Hz) and radio (10^8 Hz) emission images of the two-shell system during the flaring activity for case 4 and jet opening angle 2 degrees (top figures) and 20 degrees (bottom figures). The horizontal axis scales from 2×10^{17} to 5×10^{17} cm and the vertical from 2×10^{13} to 8.5×10^{15} cm for the 2 degrees jet and from 2×10^{13} to 2.5×10^{16} cm for the 20 degrees jet. For each subfigure the bottom images correspond to $t_{obs} = 0.23$ days, which is the time the sudden rise of the flux is observed, the middle ones to the weak decay at $t_{obs} = 0.28$ days corresponding to the propagation of the forward shock into the BM medium, and the top ones to the fast decay at $t_{obs} = 0.35$ days, once the merger has completed.

to the jet axis, the distinct contribution of the two shells can only be observed after the merger has completed.

2.5 Discussion and Conclusions

We performed high resolution numerical simulations of late collisions between two ultra relativistic shells and produced optical and radio light curves and emission images for a spherical explosion case and different opening angles of a hard-edged jet. The AMR technique allowed us to reach high resolution and properly resolve the shocks developed during the merger of the shells.

The simulations have shown that different values of the Lorentz factor and energy of the second shell can significantly change the characteristics of the

variability on the light curves. We demonstrate that for small opening angles, for which the flux is not smeared out by early emission time contribution, a flare appears at the light curve. The onset of the flare is found to be strongly dependent on the strength of the forward and reverse shock of the second shell and to become stronger the higher the Lorentz factor and energy of the second shell are. For case 4 in which the Lorentz factor and energy of the second shell are the highest in our simulations, the relative increase of the flux in respect to the underlying afterglow is $\Delta F/F = 3.95$ for the optical and $\Delta F/F = 1.04$ for the radio. The timescale of the variation of the flare is $\Delta T/T = 1.08$ and $\Delta T/T = 1.90$ respectively. The shape of the flare is understood through the dynamical simulations and the different stages at the light curve are associated with different parts of the collision process. We show that the difference in shape between the optical and radio flare as well as the time difference observed between them is a direct result of the ssa mechanism and the angle dependence of the emission. We predict that this type of behaviour should appear in late afterglow observations as a two-ring feature in spatially resolved optical emission images, although for the time being the resolution required would be unrealistic. Athough a detailed numerical approach is required to fit observational data with the numerical results, a straightforward comparison was made between case 4 of our simulations and the optical flare observed in the afterglow of GRB 060206 showing strong resemblance in the magnitude and time variation of the flare. New low-frequency facilities such as ALMA are expected to provide enough data to compare with the radio light curves as well. The details which determine the jet collimation as the jet propagates into the circumburst medium are currently not well understood. In this work we have used the same opening angle for both shells and we defer analysis of a scenario with different opening angles to future work. Such a study would require detailed simulations in 2D.

We have not explicitly discussed X-ray flares, although for these the largest amount of observational data is available. The X-ray emission is influenced by electron cooling (i.e. lies above the cooling break in the synchrotron spectrum) and is therefore also more sensitive to the details of particle acceleration than optical and radio emission. Especially in the case of multiple shocks, it becomes difficult to implement an approach to radiation that correctly captures all relevant physics in a simple parametrization.

X-ray flares appear in general in smaller timescales compared to the optical ones ($\Delta T/T \sim 0.1$ days) and in theory can be approached within the frameworks of the current model by applying a thinner and faster second shell maintaining unaltered the viability of the general concept that late time engine activity leads to a flare in the light curve.

Chapter 3

On the external shock refreshment mechanism of the GRB afterglow phase

3.1 Preface

Earlier, in essence one-dimensional numerical smulations of the deceleration stage of a gamma-ray burst (GRB) jet have provided us with a good description of the dynamics occuring during the afterglow phase and made possible the exploration of the jet emission mechanisms through the reconstruction of synthetic multi-wavelength light curves. In this work we present a follow-up two-dimensional special relativistic hydrodynamical simulation of the deceleration of a finite angle GRB jet in a uniform medium. In contrast with previous work which handle relatively large opening angles, here we examine the extreme case of a narrow 2 degrees ($\theta_0 = 0.035$ rad) half-opening angle jet which is still ultra-relativistic with Lorentz factor $\Gamma \sim 1/\theta_0$. We examine in two dimensions the shock refreshment mechanism by employing a second ultra-relativistic shell which initially propagates at the same Lorentz factor behind the external shock and present the dynamical effects on the evolution of the jet that arise from the interaction of the two shells. We find an angular dependency of the dynamical properties of the jet and associated collision time due to extraction of energy in the transverse direction at the position of the external shock. We comment on the resulting emission and predict a discrepancy between on-axis and off-axis light curves.

3.2 Introduction

Following the launch of the *Swift* Gamma-Ray Burst (GRB) mission [31] our understanding of the processes forming the γ-rays and the afterglow radiation has greatly increased. The prompt emission of long GRBs is now widely recognized as the result of the collapse of a rapidly rotating massive star into a black hole [130], [57] while the afterglow has been attributed to synchrotron radiation produced during the deceleration phase of the GRB jet. The dynamics of this part of the outflow is constrained mainly by the type of external medium (wind-type, uniform, etc.) and described properly by the Blandford-McKee self-similar solution [10]. Several distinct light curve features however, brought to light by recent multi-wavelength observations, changed our understanding of the underlying processes during the deceleration phase. Especially, rebrightenings and flares that appear in the afterglow light curves [107], [14] indicate that an activity of the central engine is taking place at times after the initial burst has occurred. The diversity in the characteristics of these events suggests that more than one physical mechanism is responsible for their appearance. Thus, very sharp rebrightenings which appear over an underlying afterglow are likely to be the result of internal collisions of ultra-relativistic shells due to a delayed activity of the central engine [45]. Others demonstrate less sharp features and show differences in the pre and post-flare slopes of the light curve. This implies a refreshment of the external shock, more likely due to energy injection from a following explosion [51, 37]. High resolution 1D-hydrodynamical simulations [124] have shown that two-shell type collisions during the afterglow phase can reproduce strong rebrightenings of the latter type. Furthermore, for small opening angles of the underlying jet, strong flares have been reproduced for both optical and radio frequencies.

An essential assumption to that model is that the lateral spreading of the jet during the deceleration is insignificant. In that case 1D models of the dynamics suffice, even for quantifying finite opening angle jet afterglows. Analytical models have shown that significant spreading is expected during the deceleration phase of the external shock [91]. Unfortunately, high resolution 2D numerical simulations of the afterglow phase are computationally very expensive due to the high resolution which is required to resolve properly the shocks arising in the shell and therefore few attempts in this direction have been made so far [142], [64], [134], [21], [20]. As shown in [142], in contrast to the analytical models, the sideways expansion of a jet with an opening angle 20 degrees and initial Lorentz factor 20 is a very slow process and starts appearing at times greater than a typical afterglow timescale. Similarly, and in agreement with the previous work, [64] showed that a rarefaction wave propagating in the transverse direction into the external shell slows down the spreading in the angular direction by

gradually extracting energy from the outer to the innermost regions of the jet.

New analytical models are trying to fill in the gap between theoretical expectations and numerical simulations. In the model proposed by Granot and Piran 2012, [38] the analytical solution remains valid also in the mildly relativistic region, where the morphology of the explosion deviates from its initial spherical shape. As shown in that work, a jet with a very narrow initial half-opening angle which is still ultra-relativistic at $\Gamma = 1/\theta_0$ will present a phase of rapid exponential lateral expansion.

In a recent numerical simulation presented by De Colle,[21] and [20], the expansion of a jet with a moderate half-opening angle ($\theta_0 = 0.2$ rad) in a stratified as well as a uniform external medium is taken into account. Here the lateral spreading appears to be faster before the jet break for the stratified medium case and slower for the uniform one, while the situation is reversed at times after the jet break. As expected, since more time is needed in order for the same mass to be swept-up in the stratified medium case, the jet break in the afterglow light curves appears significantly smoother.

We perform novel high resolution 2D numerical simulations of two shells colliding in the afterglow phase.We intentionally focus on jetted, multiple shell scenarios with opening angles of a few degrees, in line with inferred geometric parameters. We study a two shell scenario in order to explore the effects on the dynamical characteristics of the flow deriving from energy injection to the external shock.

3.3 Numerical strategy

In this model we study a flow that is still ultra-relativistic at Lorentz factor $\Gamma \sim 1/\theta_0$ for half opening angle $\theta_0 \ll 1$ radian and is constantly supplied with energy from a following shell propagating at near distance behind it. Unlike previous studies following the longterm evolution of an external shock in the interstellar medium (ISM), we mainly focus our attention on the dynamics occuring in an early stage of the afterglow while the forward shock of the second shell propagates through the previously shocked medium and collides with the self-similarly expanding external shock. Therefore, high resolution is applied throughout all the computational domain trying to capture all the details associated with the overall dynamics and particularly that of the interaction between the two shells. As global refinement criteria of the simulation we use the comoving density and Lorentz factor of the fluid. During the initial time steps the highest refinement is forced locally at the external shock front in order to avoid numerical diffusion which has been observed at the early stages of such simulations.

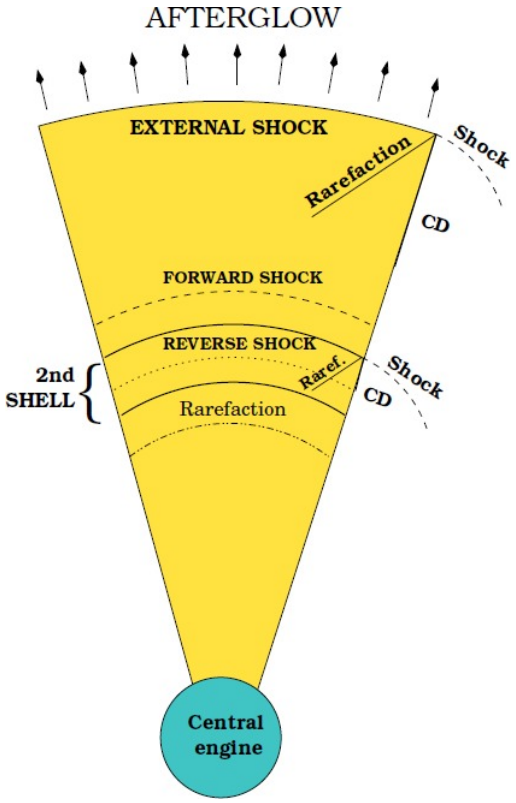

Figure 3.1: Two-shell collision model. After the initial explosion of the central object produces the gamma-rays, the external shock decelerates into the circumburst medium giving rise to the afterglow radiation via synchrotron emission. A few seconds later a following explosion of the progenitor produces a second shell which propagates into the previously shocked medium. The forward shock which is formed during the deceleration of the second shell, continuously supplies the system with energy and eventually catches up with the external shock, while a reverse shock propagating into the second shell transforms part of the kinetic energy of the shell into thermal energy. In this schematic representation the different waves and shocks that appear in our simulation and contribute to the overall dynamics are indicated for the different regions on the jet.

The simulation described in this chapter has been performed with the parallel Adaptive Mesh Refinement version of the Versatile Advection Code (MPI-AMRVAC) [43] We follow the same strategy as described in our earlier model in [124]. The Blandford and McKee (BM) self-similar approximation is adopted to describe the deceleration phase of the external shock in a uniform ISM, with particle number density $n_0 = 1\text{cm}^{-3}$. The following shell is taken as cold and ultra-relativistic placed at distance $\Delta R = 10^{14}$cm behind the BM shell. The two shells have initially the same narrow half opening angle of 2 degrees around the jet axis. The initial Lorentz factor of the external BM shock is 23, which translates to a fluid Lorentz factor right behind the shock of $23/\sqrt{2}$. The same value is adopted for the Lorentz factor of the second shell. The initial thickness of the second shell is $\delta = c\Delta t = 3 \times 10^{14}$cm, implying a duration for the second ejection event of $\Delta t = 10000$ s. The energy content of the two explosions is each taken as $E = 10^{52}$erg. A schematic view on the initial configuration, with the most prominent expected wave signals indicated, is shown in Figure 3.1.

Unlike the method applied in Vlasis et al. 2011 where the polytropic index is considered constant and takes the ultra-relativistic value $\Gamma_p = 4/3$, here we adopt a Synge-type polytropic equation with varying polytropic index (see [59] and [66] for a detailed description). The external BM shock and the forward shock of the second shell remain relativistic throughout the simulation whereas the reverse shock of the second shell starts as relativistic and turns Newtonian in later stages. This behavior necessitates the use of a varying polytropic index equation of state which takes into account both relativistic and Newtonian regions and is given by

$$p = \left(\frac{\Gamma_p - 1}{2}\right) \rho \left(\frac{e}{m_p} - \frac{m_p}{e}\right), \tag{3.1}$$

where $e = m_p + e_{th}$ is the specific internal energy including rest mass, with proton mass m_p and e_{th} is the specific thermal energy. Therefore, for chosen polytropic index $\Gamma_p = 5/3$ we achieve a locally varying effective polytropic index which takes the values between 4/3 and 5/3 and is given by

$$\Gamma_{eff} = \Gamma_p - \frac{\Gamma_p - 1}{2}\left(1 - \frac{m_p^2}{e^2}\right). \tag{3.2}$$

We adopt a spherical grid of size $[0.01, 1] \times 10^{19}$ cm and 4816 cells in the radial direction and angular size $[0, \pi/2]$ radians and 28 cells in the angular direction at the coarsest level of refinement. We use maximum 10 levels of refinement leading to an effective resolution of 2.46579×10^6 and 14336 cells in the radial and angular direction respectively. At the highest refinement level this resolution translates as a cell of size $\Delta r = 4.05 \times 10^{12}$cm and $\Delta\theta = 10.95 \times 10^{-5}$rad.

Table 3.1: All 2D GRB jet simulations to date.

	Meliani & Keppens 2010	*de Colle et al.* 2012	*Zhang & MacFadyen* 2009	*Wygoda et al.* 2011	*Vlasis et al.* 2012
Domain (r,θ)	$[0.048, 4.8] \times 10^{18}$ cm $[0, \pi/4]$ rad	$[0, 1.1] \times 10^{19}$ cm $[0, \pi/2]$ rad	$[0, 1.1] \times 10^{19}$ cm $[0, \pi/2]$ rad	$[0, 1.1] \times 10^{19}$ cm $[0, \pi/2]$ rad	$[0.01, 1] \times 10^{19}$ cm $[0, \pi/2]$ rad
AMR levels	13	15	16	-	10
Max. resolution (Δr,$\Delta\theta$)	4.23×10^{12}cm 6.98×10^{-6}rad	6.71×10^{12}cm 2.4×10^{-5}rad	5.6×10^{13}cm 9.6×10^{-5}rad	5.6×10^{13}cm 9.6×10^{-5}rad	4.05×10^{12}cm 10.95×10^{-5}rad
Time coverage (days)	245	372	5.5×10^4	4×10^4	200
Γ_0	25	28	28	28	23
$\Gamma_0\theta_0$	8.72	5.65	4	4	0.8
a_{res}	~ 0.032	~ 0.014	~ 0.12	~ 0.12	~ 0.010
Number of cells contained in 0.035 rad	5097	1458	365	365	320

As discussed earlier, several recent two-dimensional simulations have focused on the fluid properties of a decelerating blast wave using extremely high resolution and adapting highly sophisticated numerical schemes to achieve numerical accuracy and at the same time optimize the computational cost of the simulations. In all cases the quantity which appears to be the hardest to resolve is the initial BM shell, due to its very thin structure together with the high jump in the pressure and density in front of the shock. As shown in de Colle et al. 2012 [20] assuming the width Δ of the BM shell in which a fraction f of the total energy is contained, one can parametrize the numerical resolution in terms of a parameter α_{res},

$$\Delta r_{min} = \alpha_{res} \frac{R_0}{\Gamma_{sh}^2(R_0)}, \tag{3.3}$$

where Δr_{min} is the smallest resolution element in the radial direction. In Table 3.3 we include all the important initial flow parameters of all two-dimensional simulations to date together with the value of the "numerical resolution parameter" α_{res}. It can be seen that with the careful choice of the resolution and the initial physical parameters, our simulation compares favorably with the resolution argument raised in [20].

3.4 Results

In this section the results of our simulation are presented. First, we describe the global evolution of the afterglow jet and discuss in detail the different processes which occur throughout regions of the external shock and second shell and the interaction between them and the surrounding medium. Second, we discuss in more detail the merger event and indicate that the collision process takes place with a strong angular dependency. Last, we show an energetic analysis of the two-shell system during the different evolutionary stages of the jet and compare our results with previous single shell models.

3.4.1 Global evolution of the jet

In Fig. 3.2 and 3.3 we show snapshots from the dynamical evolution of the afterglow jet while it propagates through the ISM and the collision process between the forward shock of the second shell and the external shock, hereafter denoted as FS and ES respectively. The ES is normally evolving according to the BM self-similar evolution, augmented with dynamics occuring from its conical initial edge.

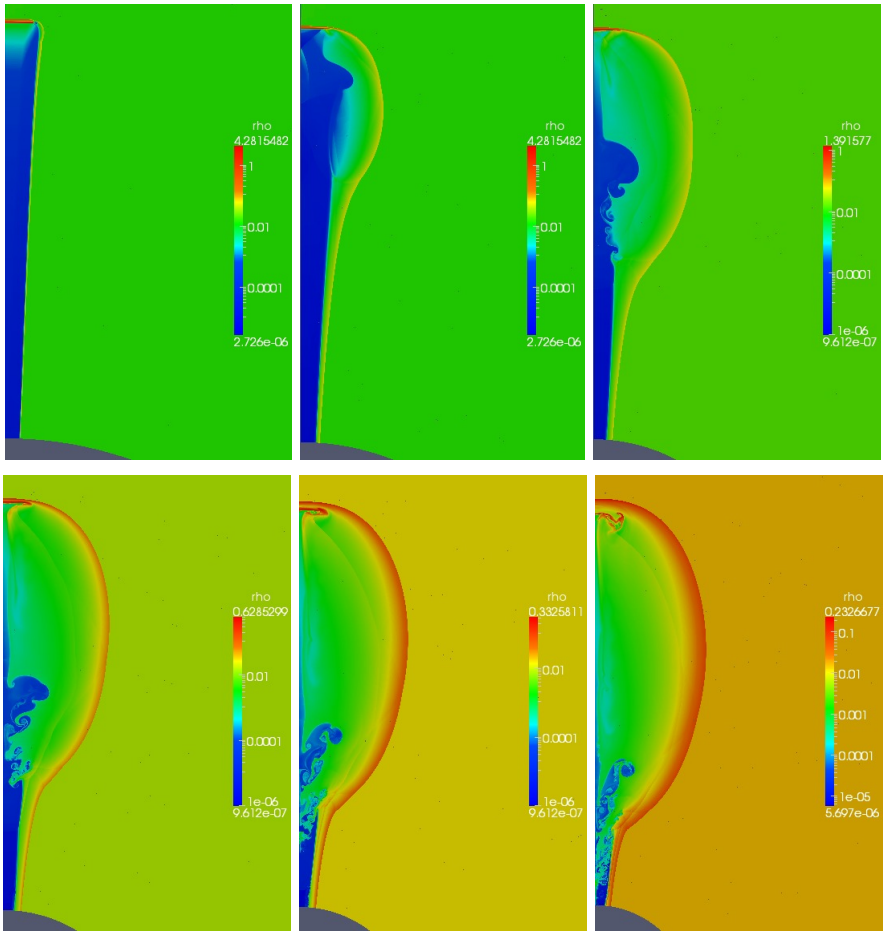

Figure 3.2: Global evolution of the jet. Our simulation covers a time period from $t_e = 79$ days (top left figure) to $t_e = 200$ days (bottom right figure) after the initial explosion. The plotted parameter is the number density in the comoving frame of the jet. Time t_e corresponds to the local emission time.

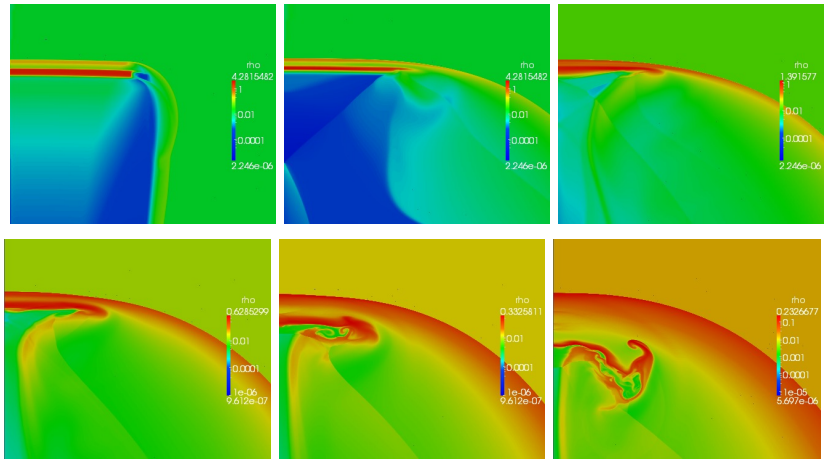

Figure 3.3: Zoom in the region of the two shells for the sequence of snapshots shown in Fig. 3.2 following the period before, during and after the collision.

As seen through the snapshots, taken at local emission times $t_e = 79, 102, 127, 148, 171$ and 200 days, the initially simple structure of the two-shell system undergoes severe modifications during the simulation. Our simulation starts 79 days (local emission time) after the initial explosion has occured. Initially, the propagation of the external shock through the interstellar medium gives rise to a rarefaction wave that propagates towards the axis of the jet and a discontinuity away from the jet separating shocked and unshocked regions. As indicated in the schematic Fig. 3.1, this is inevitably due to the finite opening angle configuration creating a local Riemann problem type setup at the corner point. At the region of the second shell, which is taken initially cold and more dense than the BM medium, a forward shock (FS) is formed which propagates through the BM shocked medium. At the same time a reverse shock (hereafter RS) develops which traverses the second shell. Similarly as before a contact discontinuity appears separating the shocked BM matter and the RS shocked shell region. Away from the jet, another shock appears between the second shell and the surrounding medium as well as a rarefaction wave and a contact discontinuity, in a fashion similar to the one described for the external shock. At the back of the second shell, a rarefaction wave propagates, originating from the interaction of the innermost boundary of the shell with the surrounding BM medium. The low density and Lorentz factor in which this rarefaction wave propagates, makes any expected observational signatures from that region to be insignificant. A schematic representation of the above description is given in Fig. 3.1.

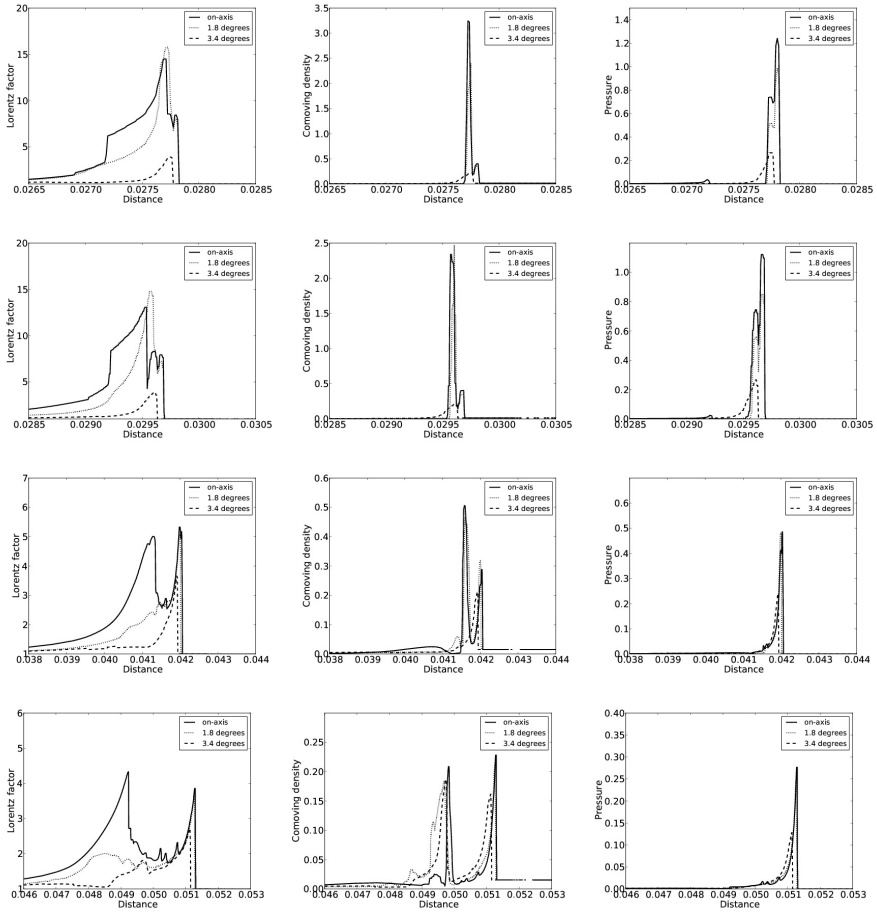

Figure 3.4: Lorentz factor, comoving density and pressure at local emission times $t_e = 106$ days when the reverse shock (RS) is still traversing the second shell (top figures), $t_e = 114$ days when the RS has just crossed the inner boundary of the second shell close to the axis, $t_e = 160$ days when the forward shock (FS) and external shock (ES) are nearly merged on-axis but have already merged for higher angles on the jet (middle figures) and $t_e = 197$ days when FS and ES have completely merged (bottom figures). The radial variations of the properties are taken for on-axis variation (solid line) and for two angles on the jet, 1.8 degrees (dotted line) and 3.4 degrees (dashed line). We notice a clear angular dependency of the Lorentz factor in the second shell. As explained in subsection 3.4.2, the RS undergoes faster deceleration for higher angles on the jet due to the interaction with the rarefaction wave originating from the ES. As a result, inside the second shell, the regions which are close to the axis are traversed by the RS at earlier times compared to those near the edges of the jet and therefore loose their kinetic energy faster (at time $t_e = 114$ days the Lorentz factor of the fluid is higher for 1.8 degrees compared to near on-axis). Distance is scaled at 10^{19} cm.

There are two dynamically important time scales in the model that describe the merger process. First, the time t_c of the collision between the FS of the second shell and the ES. As we discuss later on in the text, t_c is strongly influenced by the appearance of the laterally moving rarefaction wave originating from the ES, which leads to an angular dependency. Second, the time t_{rs} at which the reverse shock crosses the innermost boundary of the second shell. The strength of the shock depends on the interaction of the second shell with the surrounding BM medium and thus analogously as before, t_{rs} is found to vary with the angle on the jet. The shear velocities at the interface of the contact discontinuity make these locations liable to become Kelvin-Helmholtz unstable. However, the instabilities arising from that interaction occur in matter which ended up being colder than the surrounding medium and have a very small Lorentz factor. At later times they dominate the region close to the base of the jet, unable to keep up with the rapidly expanding merged system.

In Fig. 3.3 we plot a zoom of the comoving density at the region of the refreshed external shock for times before, during, and after the merger has completed. At emission time $t_e \simeq 200$ days (bottom right image) we distinguish three dynamically important regions. First, we note the combined external shock which after the collision has finished, continues to decelerate in the ISM. At the time shown, it corresponds to a thin shell with local Lorentz factor ~ 4 and overall particle density 40 cm^{-3}. Second, we identify the remainder of the second shell, still dense but significantly decelerated and underpressured. A third region behind the second shell is distinguished where the reverse shock propagates with a high Lorentz factor. The reverse shock is only remaining at the vicinity of the jet-axis and has disappeared at higher angles. There is a noteworthy variation of the properties of the jet in the angular direction indicating different radial deceleration rates for different angles through the jet.

3.4.2 The angular dependency of the merger

The initial conical shape of the jet experiences structural modifications during the early phases of the expansion. The rarefaction wave originating at the edge of the ES with the surrounding medium, propagates towards the axis in the transverse direction and extracts energy from the edge of the jet. As a result, the region close to the edge at the vicinity of the ES, decelerates faster and the explosion deviates from its initial spherical symmetry. At early times, as the second shell propagates through the wake of the external shock, it remains cold and therefore no sideways expansion is observed. In Fig. 3.4 we plot the Lorentz factor, comoving density and pressure of the system for different angles on the jet covering the evolutionary stages before, during and after the merger. As expected, for $t_e = 106$ days, the Lorentz factor and pressure at 1.8 degrees

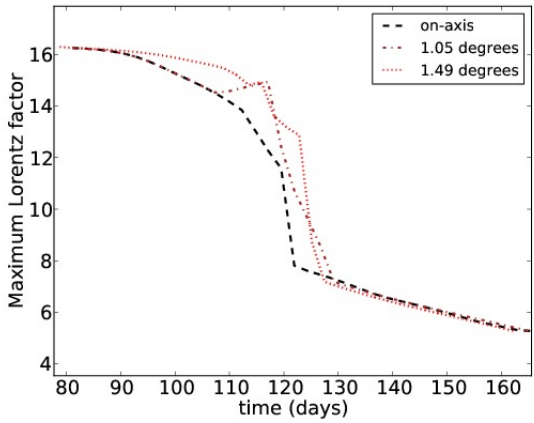

Figure 3.5: Evolution of the maximum Lorentz factor at angles 0.2 degrees (dashed line), 1.05 degrees (dashed-dotted line) and 1.49 degrees (dotted line) away from the axis. We notice that the transition to a lower Lorentz factor, indicating the crossing of the reverse shock from the second shell, occurs later for higher angles on the jet.

on the jet at the position of the ES are smaller compared to on-axis as a result of the extraction of energy from the rarefaction wave from the jet edge.

This event has a strong influence on the collision time, t_c. While the external shock decelerates and looses its spherical symmetry, the forward shock from the second shell undergoes little alteration from spherical shape. It approaches and collides therefore initially with the outermost regions of the external shock and last on axis. As seen in Fig. 3.4 for time $t_e = 160$ days, the collision has already occured for 1.8 degrees angle but not yet on axis. At approximately $t_e = 170$ days the collision has completed for all the angles on the jet.

Our model is set up so that initially the external shock and the second shell have the same Lorentz factor. At first, the external shock starts decelerating while sweeping up matter from the ISM. At the same time the forward shock from the second shell starts catching up with the external shock while the reverse shock traverses the second shell. The motion of the reverse shock is followed by a loss in the kinetic energy and a gain in the internal energy of the shocked fluid. That causes moderate expansion at early times originating from the second shell. However, the reverse shock is not strong enough to thermalize the second shell considerably and at later times, when it has crossed the second shell completely, no significant additional expansion of the shell is observed.

In a similar way as before, the propagation of the RS within the second shell and the crossing time t_{rs} present an angular dependency. The reason for that is that the strength of the shock depends on the interaction of the second shell with the shocked BM medium. Therefore, at the vicinity of the axis where the pressure of the ambient medium is high, the reverse shock is strong. Accordingly, close to the edge of the jet where the first shell has moderately expanded, the pressure is lower and thus the reverse shock appears to be weaker. As a consequence the RS exits the second shell faster close to the axis compared to high angles within the initial boundaries of the jet. In Fig. 3.4 we see that at $t_e = 114$ days the reverse shock has already crossed the inner boundary of the second shell while for 1.8 degrees angle on the jet it still remains inside. Similarly, the pressure at the second shell appears higher at the vicinity of the axis compared to 1.8 degrees angle, as a result of the propagation of the RS.

In Fig. 3.5 we show the evolution of the maximum Lorentz factor with time, for on axis variation and for angles 1.05 and 1.49 degrees, both taken within the initial opening angle of the jet. As expected, we see that the crossing of the RS from the inner boundary of the second shell is delayed for high angles on the jet compared to on axis. In Fig. 3.5 this is indicated as the sudden transition to a lower Lorentz factor occuring approximately at $t_{rs} = 95$ days for on axis and $t_{rs} = 120$ days for 1.49 degrees angle on the jet. After the RS exits the second shell, it looses fast almost all of its kinetic energy while propagating in a very low density environment. At that stage of the simulation, the maximum Lorentz factor of the system corresponds to the forward shock of the second shell which now catches up with the external shock while constantly supplying the system with energy.

3.4.3 Energetic analysis of the collision

The evolution of the jet opening angle with respect to time is shown in Fig. 3.6. We notice that the boundary of the jet in which 90% of the energy is included increases rapidly until $t_e \sim 120$ days. That indicates that as long as the jet decelerates rapidly while the reverse shock propagates into the second shell (see Fig. 3.5), the spreading of the jet is fast. After that time the maximum Lorentz factor corresponds to the FS of the second shell and the spreading of the jet appears to slow down. Until the end of our simulation the boundary of the jet does not exceed 3.5 degrees.

In Fig. 3.7 we plot the angular distribution of the energy throughout the evolution of the merger. The plotted quantity is $dE/d\Omega$. For early times, most of the energy of the fluid stays within the initial opening angle of the jet while even for later times and after the collision process has finished the

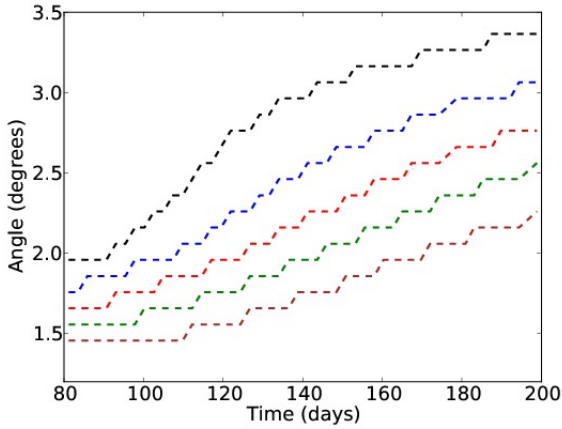

Figure 3.6: Evolution of the jet opening angle with respect to time. As long as the jet decelerates fast the spreading increases rapidly. At local emission time $t_e = 120$ days we notice the transition to slower expansion of the jet which coincides with the time t_{rs} at which the RS crosses the inner boundary of the second shell. As the jet opening angle, we define the angle on the jet which contains 90% (black line), 80% (blue line), 70% (red line), 60% (green line) and 50% (brown line) of the initial energy.

lateral spreading of the jet appears to be small. The compression efficiency of the various shocks is quantified using the effective polytropic index, Γ_{eff} which takes values between the relativistic, 4/3 and Newtonian, 5/3 extremes. In Fig. 3.9 we plot the Γ_{eff} at $t_e = 150$ days after the explosion, a few days before the forward shock of the second shell catches up with the external shock. We note that the ES is highly efficient in thermalizing the swept up ISM matter, $\Gamma_{eff} \simeq 1.35$ for the swept up matter at the vicinity of the external shock. Close to the jet axis the matter is heated to relativistic temperatures due to the propagation of the external shock and the forward shock of the second shell, while for angles closer to the edge of the jet, the fluid is Newtonian, $\Gamma_{eff} \simeq 1.5$. The reverse shock, while crossing the second shell transforms kinetic energy into thermal energy but appears inefficient to compress the fluid to relativistic temperatures, since locally $\Gamma_{eff} \simeq 1.6$.

As mentioned earlier in the text, during the propagation of the jet the contact discontinuity becomes unstable. The shear velocity between the shocked and unshocked fluid gives rise to Kelvin-Helmholtz (KH) instabilities which at late times dominate the region at the base of the jet. At time $t_e = 148$ days these regions appear to be heated to relativistic temperatures as seen in Fig. 3.9. In

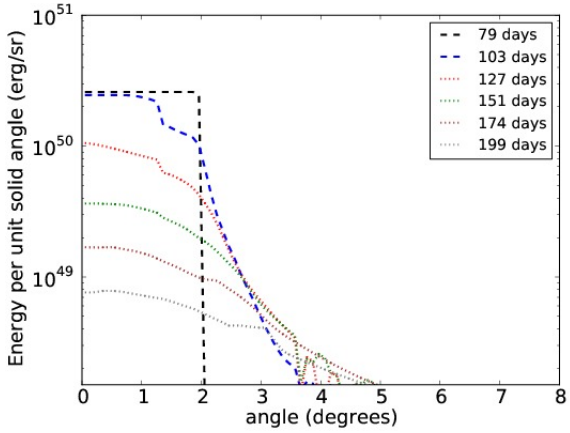

Figure 3.7: Energy density distribution with the angle for different emission times. The initial time of the simulation is taken at local emission time $t_e = 79$ days. Confinement of the energy is still retained even at late times of the simulation, $t_e \simeq 200$ days, long after the FS has merged with the ES and the RS has crossed the inner boundary of the second shell.

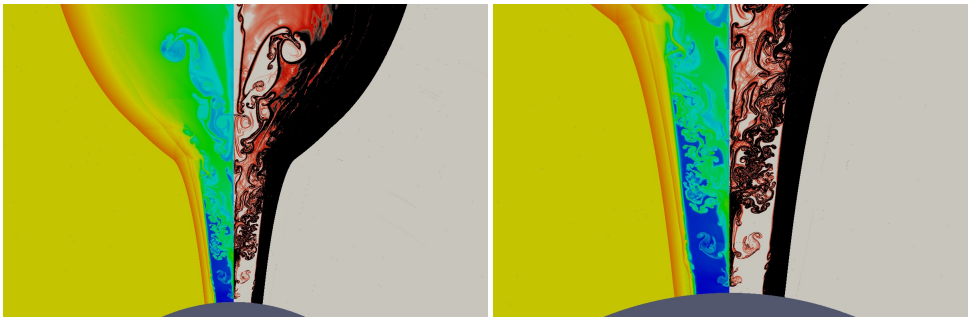

Figure 3.8: Zoom in on the base of the jet showing the comoving density and a Schlieren plot of the density at local emission time $t_e \simeq 200$ days. The KH instabilities are omnipresent throughout the simulation and at late times end up dominating the base of the jet.

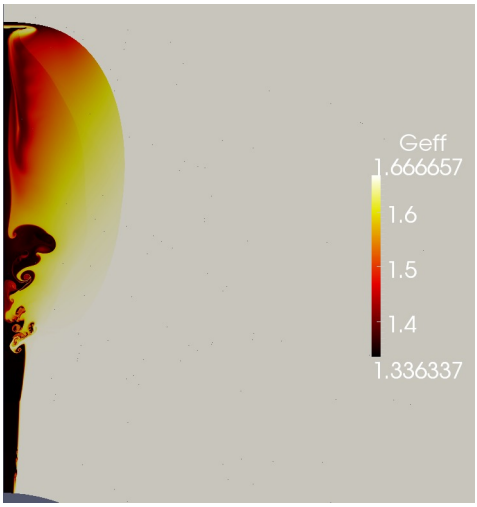

Figure 3.9: Effective polytropic index of the jet's various regions at local emission time $t_e \simeq 150$ days. Strong heating is observed at the spine of the jet. At the position of the external shock near the vicinity of the axis the matter appears to be heated to relativistic temperatures.

Fig. 3.8 we show the density at that region as well as a Schlieren plot which quantifies an exponentially stretched gradient of the proper density, here taken as $\exp[-2.525(|\nabla\rho| - 0.02)]$ at time $t_e = 200$ days. Although the mixing and turbulent features are clearly omnipresent, a result also seen in the recent work by Zhang and MacFadyen, [142] and de Colle et al.[21], this dynamics has little consequence in the emission from the GRB event, as the emission is all occuring at the ES/FS region where the pressure and Lorentz factor are high.

3.4.4 Light curves from a 1D simulation

In a similar way to chapter 2, we carry out a 1D dynamical simulation using the same initial conditions as in the 2D simulation presented in this chapter. From that we construct synthetic light curves in order to anticipate the emitting properties of such a dynamical system. The main difference with case 1 of the simulations presented in chapter 2 lies in the choice of a thicker second shell which is adopted here for numerical reasons ($\Delta t = 10^4$s compared to 10^3s in chapter 2).

The optical (5×10^{14}Hz) and radio (10^8Hz) light curves shown in Fig. 3.10,

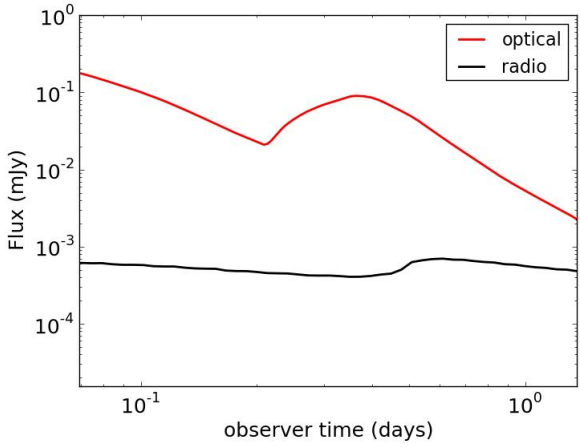

Figure 3.10: Optical and radio light curves constructed from a 1D dynamical simulation assuming initial conditions similar to the ones of the 2D dynamical simulation described in this chapter. The optical rebrightening appears less sharp compared to the ones presented in chapter 2 due to the greater thickness of the second shell. Due to self-absorption the rebrightening in the radio appears only after the collision process between the two shells has ended.

demonstrate a similar behavior to the one observed in chapter 2. As soon as the forward and reverse shock are created due to the interaction of the second shell with the BM medium, a rebrightening appears in the optical light curve since the jet is optically thin in that frequency. The optical flux continues to increase during the propagation of the forward shock inside the shocked medium of the external shell. At $t_{obs} = 0.37$ days, the forward shock collides with the external shock and the growth of the optical flux seizes. As described in section 2.4.4 the behavior in radio is considerably different. Due to self-absorption the jet is optically thick for radio frequencies and the result of the collision becomes visible only after the merger has ended, thus the peak in the radio flux shows up exactly at the time of collision.

Comparing with the light curves presented in chapter 2 for dynamical simulations with similar initial setup (case 1), the flare here appears to be less sharp. That is due to the fact that it takes longer for the reverse shock to traverse the thicker second shell. The collision time however, which depends on the deceleration rate of the external shock and the strength of the forward shock, remains the same as before $\simeq 0.37$ days in the observer's frame or $\simeq 200$ days local emission time. In addition to that, comparing the on-axis collision time from the 2D

simulation to the one found here, we notice that in the former case the on-axis collision happens sooner ($t_c = 170$ days for the 2D simulation). This is due to the appearance of a rarefaction wave which propagates in the lateral direction inside the external shell and results in a faster deceleration of the external shock. A comparison between this light curve and light curves constructed directly from the 2D simulation (on-axis and off-axis) will shed light on the effects that the collision process has on the emitting properties of the jet.

3.5 Conclusions

Numerical models have proposed that realistic light curves of the afterglow can be calculated by 1D hydrodynamic simulations. However, in order to derive the conical emission of the jet from a spherically symmetric expanding shock, these models require that the spreading of the jet is small. As presented in [124], strong variability in the afterglow can be reproduced by 1D simulation models. In the previous chapter we studied the effects on the light curves by injecting energy to the external shock and demonstrated that strong rebrightenings can appear in the afterglow as long as the sideways expansion of the jet is neglected.

In that direction, previous 2D numerical simulations have shown that lateral spreading of the jet is a slow process as long as the jet is still relativistic and grows faster when the jet decelerates to non relativistic Lorentz factor. Here we studied the dynamical effects arising from energy injection in the external shock of a jet which is still ultra-relativistic when $\Gamma \sim 1/\theta_0$. We find that although some novel characteristics are introduced to the problem, no significant alteration of the spreading of the jet is observed due to the presence of the second shell. In particular, small expansion is observed from the second shell due to the heating from the reverse shock which becomes insignificant when the reverse shock exits the second shell. The propagation of the rarefaction wave in the transverse direction at the position of the external shell introduces an angular variation of the characteristics of the problem and has an influence on the collision time t_c between the forward shock of the second shell and the external shock, and the crossing time of the reverse shock from the second shell t_{rs}. More specifically, t_c varies from local emission time $t_e = 120$ days to $t_e = 165$ days, where the first value represents collision at high angles on the jet and the latter one on axis. Similarly t_{rs} varies from $t_e = 95$ days close to the axis to $t_e = 120$ days near the edge of the jet. In terms of the emission that we expect from the jet we predict that this behaviour will affect the light curves in two ways. First, despite being small, the expansion of the jet will result in a moderate flattening of the flare since off-axis matter which has been heated by the external shock is expected to contribute to the emission. Second, the time of

the collision which in 1D models indicated the appearance of the rebrightening in the radio and the end of the plateau phase in the optical, appears to be angular dependent. Therefore, strong differences are expected between on-axis and off-axis light curves at different wavelengths.

Chapter 4

GRB jet propagation through a circumstellar bubble

4.1 Preface

It has recently been established that the circumburst medium of a GRB strongly influences the shape of afterglow light curves. So far, numerical simulations in 2D have taken into account either constant density or analytic wind-like external medium, while more realistic density profiles obtained from fully time-dependent circumstellar evolution modeling have been used only in 1D. In this work we use the code MPI-AMRVAC to perform one-dimensional and two-dimensional numerical simulations of a GRB jet propagating in the circumstellar bubble formed around a fastly rotating Wolf-Rayet (WR) star. For that we initially perform a 2D simulation of the evolution of the circumstellar medium around a massive star and use the product of that simulation as the initial condition to initiate the jet simulation. To properly describe the latter one we perform 1D and 2D dynamical simulations and construct optical and radio light curves for the 1D case. We prescribe to the jet a two-shell structure as described in detail in Vlasis et al. (2010) [124], in which the forward shell follows the spherically symmetric Blandford and McKee self-similar approximation, while the second one is taken as cold and ultra-relativistic. For the 1D simulation we examine in detail the dynamical properties of the collision of the two shells as well as the behavior of the jet during the transition of the forward shock through the termination shock of the bubble. We construct optical and radio light curves and investigate the occurance of rebrightenings in the afterglow resulting from

the merging process of the two shells and the transition from the termination shock. We conclude that the collision of the shells as well as the transition of the forward shock through the termination shock of the bubble can cause a rebrightening of the light curves and discuss under which conditions these effects can be more profound. For the 2D case we adopt a moderate initial opening angle of 5 degrees for both shells and present here preliminary results of this ongoing simulation. We notice the growth of an instability in the transverse direction of the external shock at the earliest stages of the propagation of the jet and compare it with a previously observed instability of similar type from Meliani and Keppens (2011) [64].

4.2 Introduction

Numerical simulations have been employed extensively in the recent years in order to understand the properties of a GRB jet which propagates through its surrounding medium. 1D numerical simulations of hydrodynamic or magnetized ejecta [74], [116], [71], [124], were able to provide us with a detailed examination of the propagation of the jet while precise reconstruction of multiwavelength light curves and spectra has shed light on the connection of the dynamical aspects of the fluid with the observational features of GRBs. While these simulations have the advantage of extremely high resolution due to the employment of AMR techniques, they do however neglect effects that arise from the sideways expansion which takes place during the transition of the jet to lower Lorentz factor ($\Gamma \leq 1/\theta$) and sub-relativistic speed. In that direction dynamical simulations in 2D [64], [142], [134], have been performed focusing on the lateral expansion of the jet while it propagates in an external medium of constant density. The results of these simulations show a rather slow expansion which challenges the prediction of fast expansion from analytical estimations [91],[100].

In the recent years however it became clear that the medium in which a GRB jet propagates, can significantly influence the dynamical properties of the flow and thus shape the light curves profoundly. After it quickly became apparent that the variability observed in light curves and spectra could not be explained in means of jet propagation in a constant density medium, more realistic density profiles consistent with the collapsar model and the SN-GRB association model have been exploited to do so. Motivated by this, Mimica and Giannios [70] employed a 1D numerical simulation of a jet propagating in the medium created by the collision of the winds of O and WR stars and created light curves showing a flattening of the curve at the transition of the jet from the unshocked to the shocked wind region. In [74] and [116] it is investigated the possibility of strong flares and rebrightenings which appear in a broad range of GRB light curves

to be the result of a jet encountering density jumps during its propagation at the circumburst medium. Extending these calculations in 2D, but using a more simplified medium structure, [21] studied the jet propagation in a constant and wind-like medium, taking into account effects arising from the lateral spreading of the jet during the early ultra-relativistic phase and the transition to sub-relativistic speed at the Sedov length. These simulations showed a clear discrepancy between the different cases and the jet break and lateral spreading of the jet were found to depend strongly on the jet's surrounding medium. In this work we follow an even more realistic approach and simulate in 1D and 2D the propagation of a two-shell GRB jet with moderate initial opening angle, into the circumstellar bubble of a WR star in an attempt to estimate the properties of the jet while it passes through the various regions of the bubble.

This chapter is structured as follows. In Section 4.3 we describe the hydrodynamic numerical simulation of the evolution of the circumstellar medium around a massive star which undergoes a phase of near critical rotation. We give in detail the initial conditions of the medium around the star and discuss the necessary treatments we do to make sure the results of the simulation are suitable for the initialization of the jet. In Section 4.4 we describe a long-run 1D simulation of the jet crossing the terminal shock of the circumstellar bubble and produce optical and radio light curves. In Section 4.5 we present preliminary results of our 2D high-resolution numerical simulation in which the early phase of the jet's propagation and the growth of a dynamical instability in the transverse direction is extensively discussed.

4.3 Simulation of the circumstellar bubble

Several numerical considerations have to be taken into account before initiating the circumstellar bubble simulation which have to do with the thin shell structure of the GRB jet shock front which we are going to initiate at the free region of the resulting wind, and the characteristics of the chosen grid type. Since the rotation of a star is by nature a problem of spherical geometry, we chose to set our simulation in a spherical grid. However, it is an intrinsic characteristic of a uniform spherical grid that the cells are more elongated close to the origin and become more square the further we go from the axis (i.e. $d\theta/dr$ grows with radius). At the same time, the BM shell that we use in order to describe the morphology of the jet, has to be resolved properly in that region and for that extremely high resolution is necessary. We have to make sure therefore, before initiating the circumstellar bubble simulation that the resulting cells in the vicinity of the BM shell will have a more or less square shape (i.e. $dr \simeq d\theta$)

in order to avoid numerical diffusion which otherwise will appear in the jet's shock front.

We choose therefore a spherical grid of size $[0.009, 4.3] \times 10^{19}$cm and 800 cells in the radial direction and $[0, \pi/2]$ radians and 40 cells in the angular direction which satisfies our resolution criteria. We use 4 levels of refinement leading to an effective resolution of 6400 cells and 320 cells in the radial and angular direction respectively. This corresponds to a maximum resolution of $[\Delta r, \Delta\theta] = [6.7 \times 10^{15}\text{cm}, 0.005 \quad \text{radians}]$. We use a TVDLF scheme for handling the local Riemann problems (see [113] and chapter 19 of [34] for a detailed description of the algorithm) and a two-step method for time integration. This setup ensures the proper resolution of the shock surfaces that arise in the system as well as the satisfaction of the resolution criterion of the jet, $dr \simeq d\theta$. Another numerical consideration that one has to avoid is the generation of numerical instabilities which often arise in the early phase of a circumstellar wind evolution around a massive star which may affect the accuracy of our simulations. To avoid these problems, a one-dimensional simulation is performed at the early stages of the simulation which allows for high spatial resolution at low computational cost. The product of that 1D simulation is later mapped in two dimensions and provides the initial conditions of our two-dimensional simulation. Even in the case of a fast rotating massive star this scheme can be implemented without loss of generality (for a detailed description of this method as well as some examples on its implementation on star outflows see [120] [119] and [30]) since the thin outer shell which is driven by the thermal pressure of the bubble retains rigidly its spherical shape for times longer than our simulation. On the other hand, the termination shock, which as we show later on this chapter undergoes a strong alteration from its spherical shape, is actively influenced by the strong rotational velocity field of the wind at early stages of the simulation.

4.3.1 Initial conditions

In the frame of the collapsar model for long GRBs, low metallicity massive stars are considered as the most probable progenitors for such events. Yoon et al. [137] investigated in a numerical manner the chemical properties of such massive stars and assembled a set of common characteristics which should be satisfied by possible long GRB progenitor candidates. In particular, a low metallicity threshold of $Z \leq 0.004$ has to be satisfied, which is however subject to uncertainties in the calculation of the mass loss rate from massive stars. In that work, Yoon et al. presented simulations of massive star evolution models at four different metallicities ($Z = 0.004, 0.002, 0.001, 0.00001$) adopting the quasi-chemically homogeneous scenario ([132] [136]) and computed the number

of GRBs as a function of the metallicity and redshift. The result is that near 50% of all GRBs appear at redshift above $z = 4$ while most supernovae occur below $z = 2$. That gives an average GRB/SN ratio predicted by that model equal to 1/200 while at small redshift this ratio drops down to 1/2500.

As an input for the hydrodynamic circumstellar wind study we use one of the stellar evolution models from Yoon et al. [137] for a $16M_{\odot}$ massive star with a metallicity of $Z = 0.001$. According to Woosley [130], the collapsar scenario requires a massive helium star with a rapidly spinning core as a progenitor. Recent models however of rotating stars including magnetic fields have demonstrated that it is difficult for the cores of single stars to retain enough angular momentum to produce a GRB from a collapsar [106], [58]. Yoon & Langer [135] showed that at low metallicity, a quasi-chemically-homogeneous evolution of a rapidly rotating massive star can lead to the formation of a rapidly rotating helium star without the need to remove the hydrogen envelope, avoiding in this way the mass-loss induced spin-down of the core.

The selected model covers a time period of 5.3×10^5years and gives an estimation of the mass loss rate and the rotation frequency of the star. The result of this simulation can be seen in Figure 4.1. For a long time period the star rotates slowly with a consequent moderate mass loss rate of constant value $2 \times 10^{-6}\mathrm{M}_{\odot}/\mathrm{yr}$. At approximately 3×10^4years the star rotates almost critically, increasing enormously the mass loss rate by 2 orders of magnitude. This phase lasts for only a short period of the star's life and after 2×10^4years after the critical rotation has ended the star has slowed down to a rotational frequency smaller than before, $\Omega = 0.15$, and has recovered a moderate mass loss rate. The temporal evolution of the mass loss rate and instantaneous rotational speed, as quantified in Fig. 4.1, forms the basic ingredient for the simulation of the evolution of the circumstellar bubble, the method and results of which we describe next.

4.3.2 Numerical method

Although the dynamical properties of the mass-loss rate from luminous blue variable (LBV) stars is yet far from being properly understood, it is assumed that it should be radiatively driven due to the large luminosity of the underlying star. This mechanism was initialy introduced by Castor, Abbott and Klein in 1976 [17] in order to describe the radiation force on material in O star atmospheres and has been widely used since then in order to describe radiatively driven flows. In our simulation we use the same equations for describing the lateral dependence of the stellar wind quantities as the ones initially introduced in 2002 by Dwarkadas and Owocki [25] in order to model radiatively-driven outflows

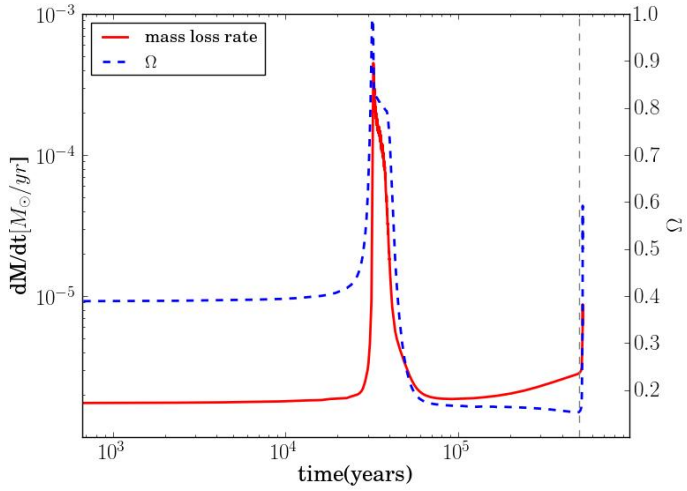

Figure 4.1: Mass loss rate (averaged in the latitudinal direction) and $\Omega = \omega/\omega_c$ for the massive star taken into account in the stellar evolution model. Here, time t corresponds in years after the initiation of the 2D simulation which is taken at $t_0 = 18.1 \times 10^6$ years. Near critical rotation is achieved at time $t \simeq 3.2 \times 10^4$ years. At the same time the mass loss rate is increasing significantly. A second strong rotational behavior with a subsequent mass loss is expected at time 5.26×10^5 years, as seen at outmost right. The dashed vertical line right before that phase indicates the time of the GRB jet initiation shortly before the second period of fast rotation of the star is reached.

from LBV stars. For this type of stars the wind is strongly influenced by the strong rotation of the star. That yields an effective gravity $g_{eff}(\theta)$ which is the true Newtonian gravity, namely $g \equiv GM/R^2$, with M,R the stellar mass and radius, reduced by the radial component of the centrifugal acceleration,

$$g_{eff}(\theta) = g(1 - \Omega^2 \sin^2 \theta). \tag{4.1}$$

The parameter Ω is defined as $\Omega \equiv \omega/\omega_c$ where ω is the frequency of the star's angular rotation and the critical frequency ω_c is given by $\omega_c \equiv (g/R)^{1/2}$. For LBV stars it is assumed that the radiative flux is not uniformly distributed over the stellar surface but changes with the latitude. According to the classical analysis of Zeipel (1924) [125], the radiative flux $F(\theta)$ of a rigidly rotating gaseous mass is proportional to the effective gravity. It is straightforward to see that near the equator where the gravity is centrifugally reduced the radiative flux is expected to be smaller compared to the poles. This effect has a

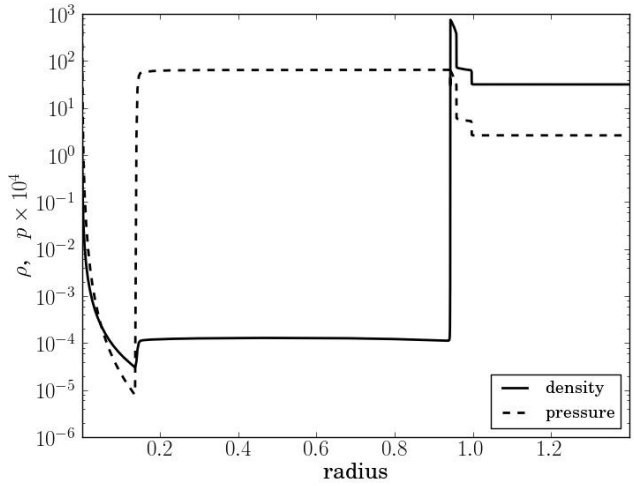

Figure 4.2: Initial density (solid line) and normalized pressure (dashed line) of the circumstellar medium during the initialization of the two-dimensional simulation. Starting from the origin we have the freely expanding wind, the wind termination shock, the hot bubble of shocked wind material, the thin shell driven by the thermal pressure of the bubble and the interstellar medium. Distance is normalized at 3.07×10^{19}cm.

predominant effect on the shape of the stellar wind and is often referred to as *gravity-darkening*. Given that, the mass-loss rate $\dot{m}(\theta)$ scales with the latitude as

$$\frac{\dot{m}(\theta)}{\dot{m}(0)} = \frac{F(\theta)}{F(0)} = 1 - \Omega^2 \sin^2 \theta, \tag{4.2}$$

where $\dot{m}(0)$ and $F(0)$ is the mass-loss rate and radiative flux at the pole respectively. The wind velocity at distances far away from the star at angle θ is given by

$$\frac{u_\infty(\theta)}{u_\infty(0)} = \left(1 - \Omega^2 \sin^2 \theta\right)^{1/2}, \tag{4.3}$$

where $u_\infty(0)$ is the velocity at the pole ($\theta = 0$).

Knowing the mass loss rate $\dot{m}(\theta)$ from the stellar evolution model allows us to calculate the density of the wind in a similar way as before,

$$\rho(\theta) = \frac{\dot{m}(0)}{4\pi u_\infty(0) R^2} \left(1 - \Omega^2 \sin^2\theta\right)^{1/2}, \tag{4.4}$$

where the quantity $\dot{m}(0)/4\pi u_\infty(0)R^2$ represents the density at the pole.

4.3.3 Results

For the greatest period of its life the star is rotating with $\Omega = 0.4$. This value remains constant until $t \simeq 3.2 \times 10^4$ years where the star begins rotating critically. As mentioned earlier in the text, for numerical reasons and in order to have the maximum possible resolution at the earliest phase of our simulation, we initiate a 1D simulation for the first years of the evolution of the circumstellar bubble before the first fast rotational period is achieved. This simulation lasts until $t_0 = 18.1 \times 10^6$ years after which we initiate the 2D simulation. The result of this simulation is shown in Fig. 4.2 and presents the formation of a circumstellar bubble around the massive star. From left to right we notice the free-wind region, the termination shock, the hot bubble of the shocked wind material and the thin outer shell of shocked interstellar medium matter. This result is used as our initial conditions for the two-dimensional simulation starting around 3×10^4 years before the near critical rotation phase is achieved. The dynamical behavior of the circumstellar medium is shown in Figures 4.4 to 4.8. We notice that from early stage the termination shock loses perfect spherical symmetry as expected from [120] and takes an elliptical shape close to the poles.

At critical rotation (Fig. 4.8), the star loses in a very fast rate most of its mass while the thermal pressure close to the thin external shell is increasing due to compression of the hot shocked wind material. Again we notice an aspherical shape of the rapidly expanding matter which can be explained from the dependence of the mass-loss rate with the latitude θ given by 4.2. Close to the equatorial plane where the effective gravity is small the radiative flux and consequently the mass-loss rate will be reduced compared to the poles.

The shape and position of the termination shock is essentially determined by the balance between the ram pressure of the free wind and the thermal pressure of the shocked wind material. Critical rotation causes a rapid change of this balance. This results in a fast propagation of the termination shock within the bubble and a strong deformation of its shape. Eventually the termination shock becomes unstable, the wind breaks through and collides with the thin shell of

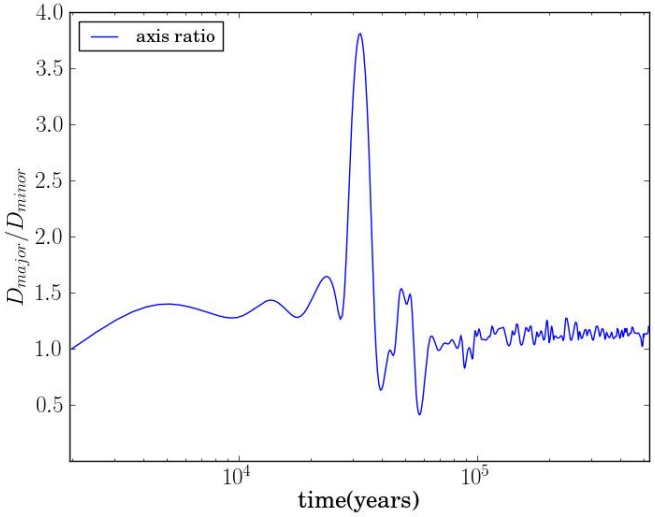

Figure 4.3: Time evolution of the ratio of the lengths of the major and minor axis of the elliptical terminal shock. At early times before critical rotation, the terminal shock retains an elliptical shape with the major axis lying on the rotational axis of the star. During critical rotation strong variability is observed and the terminal shock propapagates fast from the poles. At later times the terminal shock regains elliptical shape until the end of our simulation.

the shocked ISM. The latter one is too dense to let the colliding matter break through and as a result the shocked wind is reflected back towards the inner regions of the bubble. For a short period after the collision with the external shock the termination shock is strongly variable Fig. 4.5 (left) and pulsates radially before stabilizing in an ellipsoid form, Fig. 4.5 (right).

In Fig. 4.3 we show the time evolution of the ellipsoid of the termination shock. We quantify this by means of the ratio D_{major}/D_{minor} of the major over the minor axis of the ellipse. Throughout this calculation we assume that the major axis of the termination shock is always lying on the rotational axis of the star while the minor one is lying on the equator, thus values of the ratio below unity indicate a switch between the two axis of the ellipse. We notice that throughout the entire period before critical rotation which is characterized by a mass loss rate of $2 \times 10^{-6} \mathrm{M}_{\odot}/\mathrm{yr}$, the termination shock remains strongly elliptical with the major axis of the ellipse being on average 1.4 times greater than the minor and always lying on the rotational axis of the star ($D_{major}/D_{minor} > 1$). During the fast rotational period of the star where the mass loss rate gets the maximum

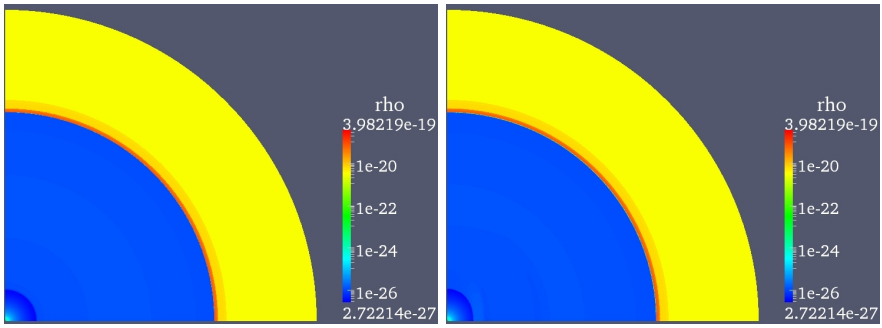

Figure 4.4: Density of the circumstellar bubble at the initial state (left) and at time $t_e = 2000$ years (right) after the initiation of the simulation. In the radial direction we notice at the end of the free-wind region the termination shock and the thin shell of shocked interstellar matter at the end of the shocked wind medium (see Fig. 4.2 for a 1D cut and for the characteristic scales of the system). The termination shock appears to lose its spherical symmetry soon after the initialization of the simulation while the external shell remains unaltered throughout the entire time of our calculations.

value of $6 \times 10^{-4} \mathrm{M}_{\odot}/\mathrm{yr}$, the termination shock becomes strongly variable and for the time period between 3.2×10^4 and 10^5 years the major and minor axis of the ellipse switch places several times ($D_{major}/D_{minor} < 1$). After this strongly disordered phase and as the star slows down the termination shock settles down to its previous elliptical shape. However now, after the star has been strongly decelerated (an average rotational frequency of that period is $\Omega = 0.16$) the elliptical termination shock is characterized by a smaller average ratio between the two axis of the ellipse ($D_{major}/D_{minor} \simeq 1.2$). This behavior lasts until the second fast rotational period of the star is reached, the time at which we stop the simulation and initiate the GRB jet.

4.4 1D simulation of a GRB jet propagation

In order to anticipate and validate the results from the 2D simulation we perform a high-resolution 1D simulation where we apply the same initial conditions as in the 2D case. For that we exploit a 1D cut along the radius of the bubble at $\pi/4$ which we set as the initial condition for that simulation. As mentioned in chapter 2, extremely thin structures like a BM shell require very high resolution at the initialization of the simulations in order to be properly resolved. We handle that issue by applying extra refinement for the first time-steps at the

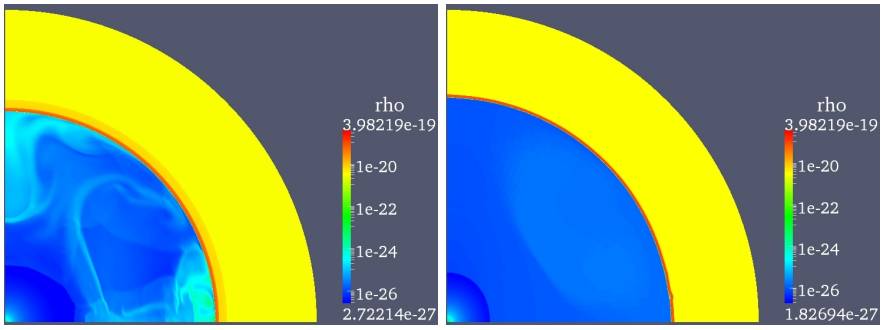

Figure 4.5: Density in the circumstellar bubble soon after the critical rotation is achieved (left) and at time 5.2×10^5years (right) when we stop the simulation. The strong aspherical shape of the termination shock soon after the critical rotation is due to the fastest propagation of the wind close to the poles during the reflection from the thin shell of shocked ISM. Strong turbulence is observed in the shocked wind. On the right we notice the ellipsoid shape of the termination shock at the end of the simulation in which we will initiate the GRB jet.

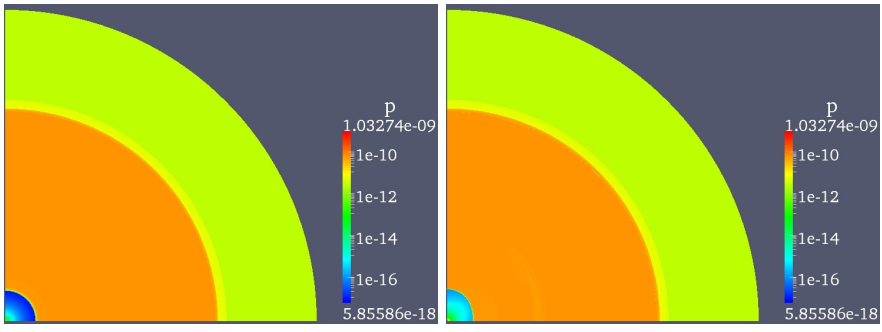

Figure 4.6: Pressure in the circumstellar bubble at the initial state (left) and at time $t = 2000$ years (right) after the initiation of the simulation.

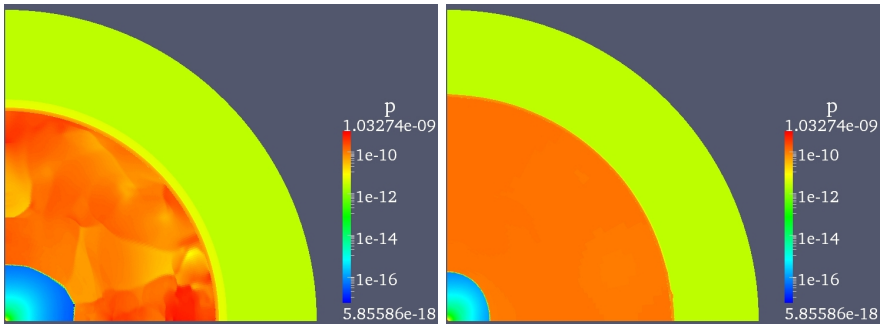

Figure 4.7: Pressure in the circumstellar bubble soon after the critical rotation is achieved (left) and at time 5.2×10^5 years (right). The turbulent phase soon after the critical rotation of the star gives place to a quiet phase which lasts throughout the whole period covered from our simulation and is finished at the time when the second critical phase of the star is achieved.

region of the BM shock. We still however experience an increase of the Lorentz factor from $\Gamma = 16.2$ to $\Gamma = 23$ due to numerical diffusivity at the earliest stages of the simulation. We argue that the effects that might rise on the light curves from such a change on the Lorentz factor can be safely considered insignificant since this increase happens only at a region in front of the external shock which is characterised by very small density and pressure. It is however noticeable that this arises in a density profile with $k = 2$ simulation to a greater extend compared to the $k = 0$ simulations presented in chapter 1. This allows us to assume that such a numerical issue shows up due to the increase of the density jump with time while considering a wind density medium around the jet. The purpose of this simulation is to investigate the case of energy injection in a more realistic environment than the ones already tested in the literature. The dynamical simulation is described in the following section where we focus on the collision process between the two shells as well as the transition of the merged shell from the termination shock. In section 4.4.3 we produce optical and radio light curves and investigate the effects on the light curves arising from the different dynamical stages of the system.

4.4.1 Initial setup

The initial condition of the simulation is shown in Fig. 4.9. It consists of the two-shell structure (cold ultra-relativistic shell - Blandford & McKee shell) build-in the medium extracted from the circumstellar bubble simulation as described earlier in the chapter. From left to right we recognize the cold ultra-relativistic

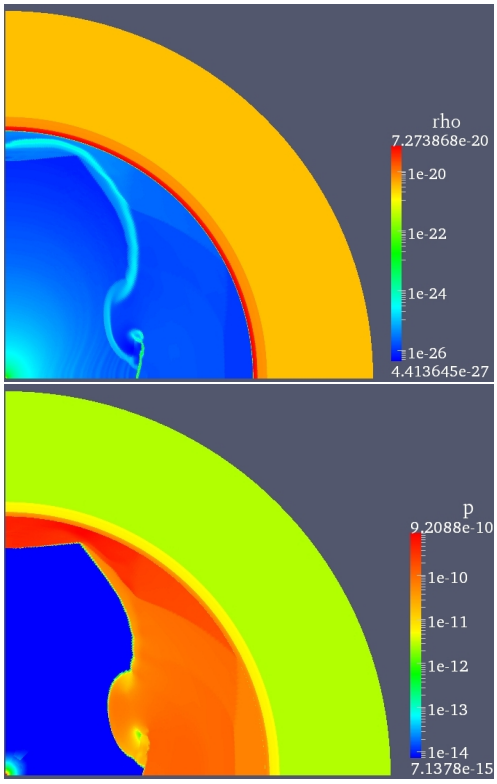

Figure 4.8: Density (top) and pressure (bottom) in the circumstellar bubble immediately after the period of critical rotation has passed at time 3.9×10^4 years. The strong non-spherical shape of the expanding termination shock is explained in terms of the equation 4.2 due to gravity-darkening in the equatorial plane and the subsequent reduction of the mass-loss in that region. High pressure is observed close to the thin outer shell of shocked ISM due to compression of the expanding wind in favor of the regions close to the pole.

shell with initial Lorentz factor $\Gamma_{sh} = 23/\sqrt{2}$ propagating at a distance 10^{14}cm behind the BM shell set at Lorentz factor $\Gamma_0 = 23$. Initially the jump in the density between the second shell and the BM medium is $\sim 10^3$ and the jump in the pressure $\sim 10^{-4}$.

The second shell is taken sufficiently colder compared to its shocked surrounding medium in order to avoid spreading due to the high thermal energy. In front of the BM shell we encounter the free wind region of the star. The density in that region follows a power-law $\rho \propto r^{-k}$ with $k = 2$. The initial density jump between the BM shell and the free wind is 10^3 while the pressure jump is $\sim 10^8$. The free wind region ends at the terminal shock which is at distance 6.7×10^{18}cm from the source. The medium of the circumstellar bubble is characterized by a moderate jump in the fluid properties across the termination shock (the density jump is ~ 6 while the pressure jump is ~ 5). Next we encounter the shocked wind material which extends up to distance 3.11×10^{19}cm from the central star and ends at a thin shell structure formed from the shocked ISM matter.

4.4.2 Dynamic description of the simulation

As described in detail in Chapter 2 the initial state of a two-shell setup requires mainly solving the Riemann problem forming at the discontinuous regions of the flow. Similarly to the case described in Vlasis et al. 2012 [124], at the surface between the second shell and the BM shocked medium we have the formation of a forward shock propagating inside the shocked BM matter, a reverse shock propagating through the second shell and a contact discontinuity appearing in between the two shocks. The forward shock of the second shell starts propagating through the BM medium while re-heating the encountered matter and thus increasing the internal energy of that region. At the same time the propagation of the reverse shock across the second shell leads to the transformation of its kinetic energy into thermal and to the drastic deceleration of the shell. The collision process between the two shells starts at the initiation of the simulation when the forward shock of the second shell is formed and lasts until $t_e = 6.33 \times 10^7$sec, time at which the forward shock collides with the external BM shock.

At this simulation we focus on the transition of the merged shell through the termination shock and during its propagation in the shocked medium and try to investigate potential signatures on the light curves. In our simulation this transition happens at time $t = 2.18 \times 10^8$sec at which time a small increase in the pressure is observed. The global behavior of the pressure and the density is presented in figure 4.10. Initially the pressure decreases as a power-law with little effect arising from the collision of the two shells. Ths same behavior is

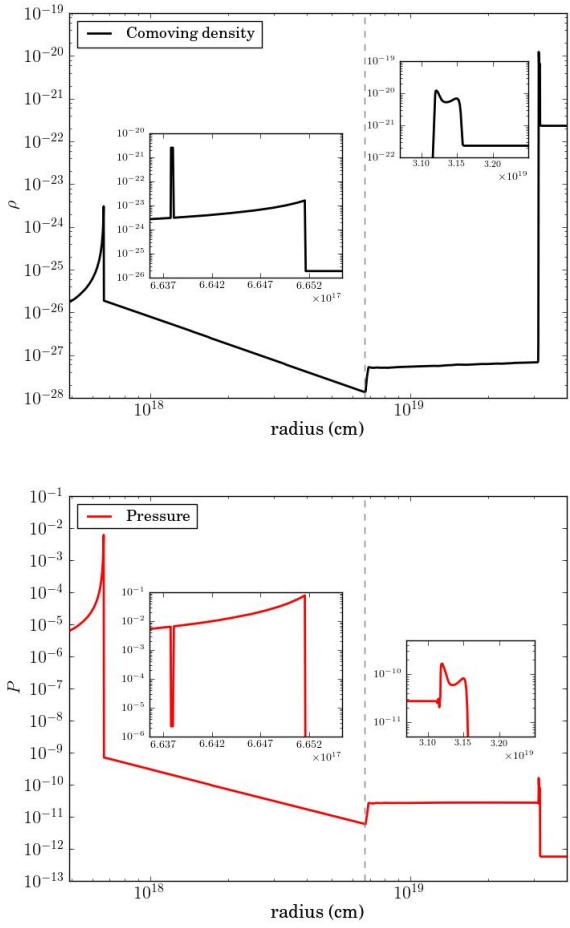

Figure 4.9: Comoving density (left) and pressure (right) at the initial state of the 1D simulation at emission time $t_e = 2.2 \times 10^7$sec. From left to right we encounter the two ejecta (BM shock and cold ultra-relativistic shell - left subplot) the free streaming wind, the termination shock at distance 6.7×10^{18}cm followed by the shocked wind material, the thin shell of shocked ISM matter (right subplot) and the unperturbed ISM.

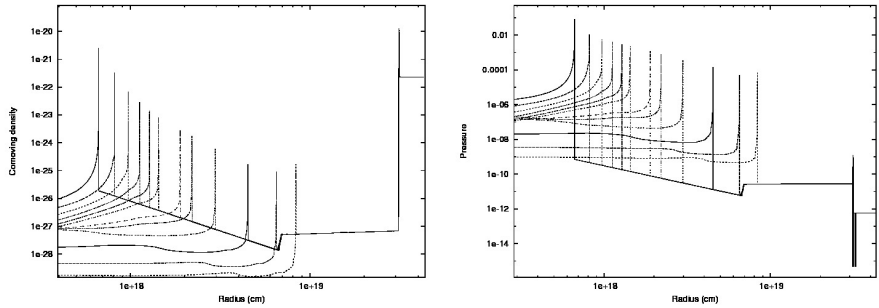

Figure 4.10: Global density (left) and pressure (right) in the circumstellar bubble, from the initiation of the simulation until time 4.8×10^8sec soon after the merged shock has crossed the termination shock. Both pressure and density drop as power-law until the transition through the termination shock. At that time a small increase of the fluid pressure and density is observed resulting to a concurrent minor increase in optical and radio photon flux (Fig. 4.11).

observed at the density as well. The reason for that is that throughout our simulation the BM shock dominates the pressure and little effect is noticed when the forward shock of the second shell catches up. This power-law decrease seizes to exist when the merged shock crosses the termination shock after which the pressure and density slightly increase. After the crossing of the termination shock the pressure starts decreasing again but at a smaller rate since the shock now propagates in the constant density medium of the shocked wind material.

4.4.3 Light curves

In this section we produce optical (5×10^{14}Hz) and radio light curves (10^8Hz) for the times under consideration in our simulation. As described in detail in Chapter 2 and shown in Vlasis et al. ([124]) we use the numerical code developed by van Eerten and Wijers [118] which solves the radiative transfer equations for a large number of rays traversing the fluid. We consider synchrotron radiation to be the dominant emitting mechanism at the shock surfaces. With similar arguments as the ones used in Chapter 2 and shown in detail in Appendix A we can neglect inverse Compton emission from our calculations without loss of generality. For simplicity we neglect electron cooling effects. We do however account for the effects arising from ssa mechanism which has an important influence on our results as we have already established in chapter 2.

Similarly to our previous calculations we assume that a fraction of the internal energy gathered behind the shock front is used in accelerating the electrons

and another part in generating and multiplying the magnetic field. Given this assumption we are able to fix the values of ϵ_B and ϵ_E to 0.01 and 0.1 respectively and assume a power-law distribution for the accelerated electrons with $p = 2$. The fraction ξ_N of the electrons accelerated to this power-law is set at 0.1. Then as shown in [118] the flux of the observed photons is given by eq. 2.4 (see Introduction and Chapter 2 for a more detailed analysis).

In Figure 4.11 we plot optical (left) and radio (right) light curves covering the time period starting from $t_{obs} = 0.2$ days and ending at $t_{obs} = 10$ days when the merged shell has crossed the termination shock. As in the case of the 1D simulations presented in Chapter 1, we notice also here a similar behavior with the flare initiation occuring at time $t_{obs} = 0.65$ days at the optical light curves. This increase of the flux corresponds to the formation of the forward shock between the second shell and the shocked BM material and lasts for the time it takes for it to catch up with the BM shock. In these light curves the received flux is calculated after taking into account a spherically symmetric scenario and two collimated outflows of 5° and 2° described by the hard-edged structure as presented in Chapter 2. It is clear that for a hard-edged jet of 2° the increase of the flux is much stronger than in the spherical explosion and the 5° case. As discussed extensively in Chapter 1 in the case of the spherical explosion this is due to early time contribution from high emission angles which conceals the effects of the forward shock formation.

It is important to notice that although the interaction of the two shells appears to significantly influence the light curves, this is not the case for the transition of the merged shock from the termination shock of the circumstellar bubble. For the 2° and 5° jet a small deviation from the normal decline of the flux is observed at $t_{obs} = 3$ days. As expected from the discussion above this change becomes less obvious for the spherical explosion. Similarly, for the radio light curves a strong flare-like behavior is observed for the smaller opening angle case and a rather smooth transition is observed while the merged shell crosses the termination shock. As seen in Chapter 1, a time difference between the peak of the flare in the optical and in the radio is observed as a result of the synchrotron self-absorption mechanism.

Immediately after the transition of the merged shell from the termination shock of the bubble, a change of the slope appears in both the optical and radio light curves. This is due to the propagation of the shell inside a more dense medium (transition from $k = 2$ to $k = 0$) which forces the shell to decelerate faster than before causing the appearance of a *termination break* in the light curves. As seen in Fig. 4.11 for both optical and radio light curves, this *termination break* appears earlier the smaller the opening angle is, in a fashion similar to the *jet break* observed in the simulations performed in chapter 2. A detailed discussion on the behavior of *jet breaks* can be found in van Eerten et al. (2011) [117].

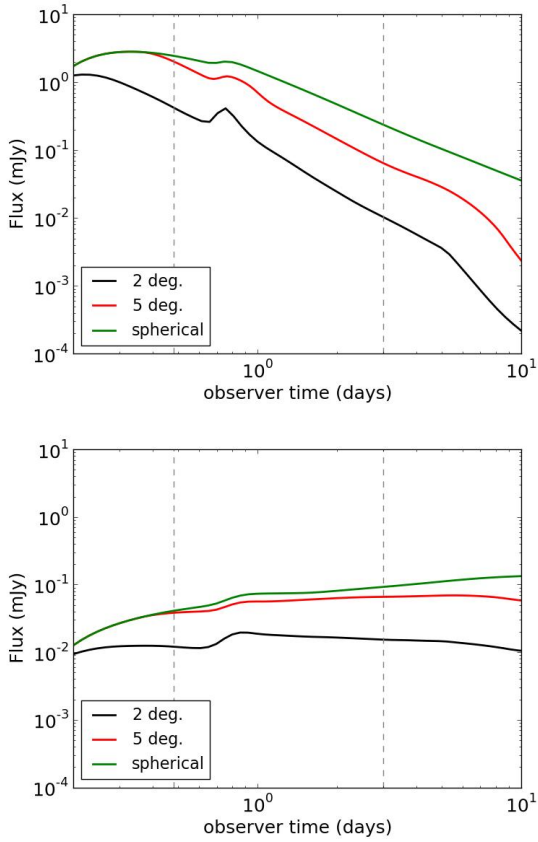

Figure 4.11: Optical (5×10^{14}Hz, top figure) and radio (10^{8}Hz, bottom figure) light curves for an isotropic explosion, and for the case of a 2° (black line) and a 5° (red line) half opening angle hard-edged jet. Both hard-edged jet light curves exhibit a bump at $t_{obs} = 0.64$ days as a result of the collision process between the two shells. At $t_{obs} = 3$ days a slight increase of the flux occurs while the merged shock crosses the termination shock. For the case of an isotropic explosion a more flattened light curve is observed with small influence from the collision of the shells and insignificant alteration due to the crossing from the termination shock. The two vertical lines denote the expected *jet break* time for the 5° case (left line) and the crossing of the merged shell from the termination shock (right line).

A theoretical estimation of the *jet break* for the 5° hard-edged case calculated using eq. 2.20 is denoted by the left vertical line in Fig. 4.11.

Albeit the small influence that the termination shock has on the light curves in that particular case, we can safely make the assumption that a stronger termination shock (meaning one that has a higher density and pressure jump) which is predicted by standard stellar evolution models can have a greater impact on the light curves. In addition since the position of the termination shock, as discussed earlier in the text, is mainly influenced by the balance of the ram pressure of the wind and the thermal pressure of the shocked material in the bubble we can postulate that according to the initial position of the jet compared to the termination shock the collision of the merged shell can happen earlier than the time in the simulated case. That means that a stronger shock (which is expected at earlier times) will have a stronger effect on the light curves while crossing the termination shock and can possibly generate a flare-like behavior similar to the one observed during the collision phase of the two shells. Similarly a star evolving in a higher density medium will give rise to a circumstellar bubble of a significant smaller size in which the termination shock and the thin shell of shocked ISM are closer to the star thus favoring the scenario of an earlier interaction between the GRB jet and the circumstellar bubble.

4.5 Preliminary results from a high resolution 2D simulation of a GRB jet

The jet is initially set at distance $R_{sh} = 6.65 \times 10^{17}$ cm from the star in the free wind region of the circumstellar bubble and has a moderate initial opening angle, $\theta_0 = 0.087$ rad, assuming a common rotation axis for the two shells. Similarly to the model described in [124] the first shell is described by the Blandford and McKee self-similar approximation [10], hereafter denoted as BM, while the second shell is taken initially as cold and ultrarelativistic and is initiated at distance 10^{14}cm behind the BM shock and has a width of $\Delta R = 10^{14}$cm. The Lorentz factor Γ and isotropic energy E_{iso}, have initially the same value for the two shells, $\Gamma_0 = 23$ and $E_{iso} = 10^{53}$erg. The initial condition at the vicinity of the two shells is shown in Fig. 4.12. At the initiation of the simulation we enforce strong refinement at the vicinity of the two shells and derefine behind and ahead of that region in order to reduce the computational cost of the simulation. The GRB jet is initiated into the grid of the circumstellar bubble. Hence similar as before the grid of our simulation is $[800 \times 40]$ cells in the lowest refinement level corresponding to a physical domain of size $[0.01, 4.3] \times 10^{19}$cm. We use 15 refinement levels leading to an effective resolution of 1.3×10^7 cells in

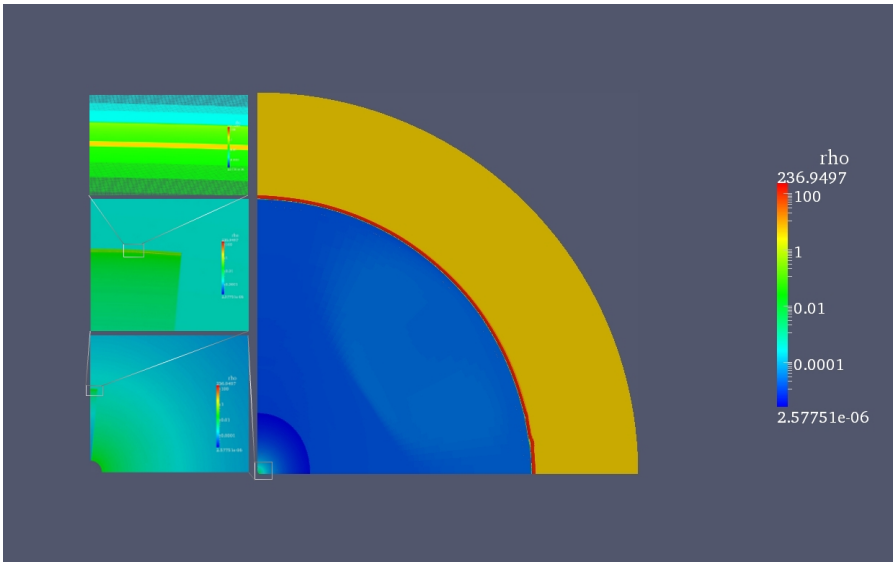

Figure 4.12: Initiation of the GRB jet into the circumstellar bubble. The plotted quantity is the comoving density of the fluid normalized to the proton mass. On the right we show the circumstellar bubble and on the left a close-up on the region of the jet. On the top left subplot we show the grid structure at the vicinity of the two shells. The highest refinement (15 levels) is enforced close to the two shells while we derefine behind and ahead of that region in order to reduce the computational cost.

the radial and 6.6×10^5 cells in the angular direction. In maximum resolution this corresponds to a cell of size $\Delta R = 3.3 \times 10^{12}$cm and $\Delta\theta = 2.3 \times 10^{-6}$. As we see from Table 3.3 in Chapter 3 in this simulation we achieve resolution which hitherto had not been accomplished. This allows for a careful study of the properties of the decelerating blast wave as well as a detailed analysis of the Riemann problem at the boundaries of the second shell which as we have seen can influence predominantly the dynamics of the collision process between the two shells as well as give rise to distinct signatures on the light curves.

4.5.1 Results

We initiate the simulation at time $t = 2.2 \times 10^7$sec after the initial explosion from the star. As described in Chapter 3 the initial phase of the jets propagation consists of the formation of a forward shock propagating into the BM shocked

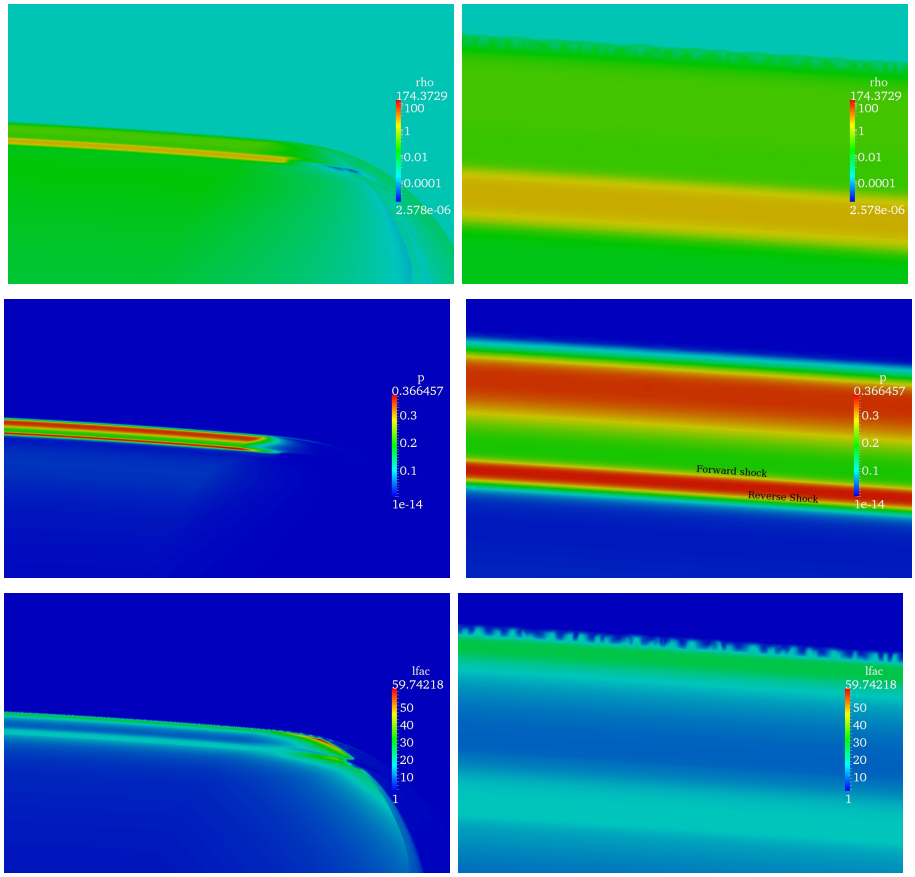

Figure 4.13: Comoving density (top), pressure (middle) and Lorentz factor (bottom) of the GRB jet at time $t_e = 2.4 \times 10^7$sec soon after the initiation of the simulation. A close-up at the vicinity of the two shells (right pictures) reveals a transiently growing instability at the region of the forward shock.

medium and a reverse shock traversing the second shell. As seen in Fig. 4.13 at time $t = 2.4 \times 10^7$sec the result of the propagation of these two shocks is the strong increase of the pressure at the relevant regions (middle images). At the same time the initial pressure difference between the $\theta = 5^\circ$ border of the jet and the surrounding medium results in a small spreading of the jet in the sideways direction. This behavior however is localized in a small area characterized by very low density and pressure and is not expected to affect in any way the dynamics of the jet or influence local emission calculations and constructed light curves.

In Meliani and Keppens 2010 [64], the expansion of a single blast wave is examined in a similar resolution as in this work. As presented in that work, during the early phase of the deceleration of a blast wave an instability appears at the shock front provided that the motion of the shock remains relativistic. There, the instability is described as the relativistic analogue of the classical *Vishniac* instability [121], of a thin spherical shock against dynamic and effective gravitational perturbations.

In the classical case it is established that short-term shock fragmentation is expected when a shock is propagating in a density gradient due to perturbations induced by the difference in pressure between the two sides of the shock surface. In that way, shocked material is confined in the post-shock, dense area in front of the shell, in a region which is small in comparison to the radius of the shell [121]. In that case the shock is found to be surprisingly stable in the presence of this instability. Similarly, in our simulation we notice that in the shocked region of the free-wind circumstellar matter where the density decreases as a power-law, right in front of the external shock an instability appears which is well confined in a region of width approximately 10% of the shell's radius. A close-up of this instability is shown in Fig. 4.14. In that figure we also plot the overlying grid, indicating that the maximum resolution is enforced on the region of the shock, something which is necessary in order to capture the small structures of the instability which would otherwise be overlooked.

We estimate that approximately 60000 CPU hours are still needed until the two-dimensional simulation reaches the stage of the one-dimensional one and follow the propagation of the GRB jet throughout the collision process and the crossing over the termination shock of the bubble.

4.6 Conclusions

This chapter is part of an ongoing research project where the complete process of the propagation of a relativistic blast wave into a circumstellar bubble is

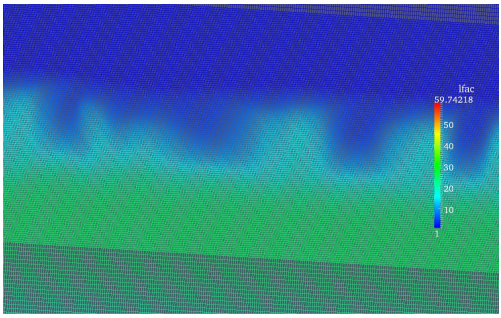

Figure 4.14: Close-up at the fluid's Lorentz factor at the region of the extenal shock where the instability appears. At that region the highest resolution (15 levels) is enforced.

examined. For that we initially carry out a hydrodynamic simulation of the evolution of a circumstellar medium around a fast rotating star and initiate the jet at the free-wind region of the star. For the jet we employed a two-shell structure as it was introduced in Vlasis et al. 2011 [124] in order to investigate the possibility of generation of flares in the light curves originating from the collision process between the two shells as well as from the transition of the merged shell over the termination shock of the bubble. For that we run two relativistic hydro simulations. First, a one-dimensional simulation covering the full time period between the initiation of the merging process between the two shells and lasting until the merged shell has crossed over the termination shock of the bubble. For that simulation we produce optical and radio light curves for a spherical scenario and two hard-edged jets and indicate the appearance of significant flaring activity predominantly in the optical, which is attributed to the collision process between the two shells. On the other hand, the crossing from the terminal shock does not appear to significantly influence the light curves, apart from a smooth increase on the optical photon flux and only for the hard-edged jet scenario, mainly due to the small pressure jump and the fact that the merged shock by that time has been considerably decelerated. We argue that a collision of the merged shell with a stronger terminal shock occuring in earlier time of its propagation, might show a notable flux increase on the light curves. Second, we produce a two-dimensional simulation with the same initial conditions as in the 1D case employing an unprecedented spatial resolution of the decelerating blast wave. In the early phase of the simulation we notice the appearance of an instability at the region in front of the external shock similar to the Vishniac-type instability seen in Meliani and Keppens 2010 [64]. Further understanding of the processes forming this instability is required in addition to a complete two-dimensional simulation covering the full period

of the propagation of the jet within the circumstellar bubble. Comparisons of the light curves obtained from the full 2D simulation with those assuming 1D aspects will need to quantify any effect of the shock fragmentation on the early light curves, and see whether flaring aspects are altered by lateral spreading on multi-dimensional dynamics when crossing the termination shock.

Chapter 5

Conclusion

The propagation of a decelerating relativistic blast wave presents great scientific interest from both theoretical and numerical point of view. The pioneering work of Blandford and McKee in 1978 and the introduction of the self-similar solutions, simplified a very difficult task at the time which was to find solutions of the special relativistic hydrodynamic equations in the case of a relativistic blast wave. Little topics in the broader field of *Gamma-Ray bursts* have been so thoroughly studied in the past few years and that is due to the great importance this phenomena have in understanding the few observational data we have from these exotic but distant and sparse events in the universe. In that direction several attempts have been made in order to establish a connection between the dynamical properties of an expanding blast wave and the observational data. Despite the progress that has been made in analytical studies of these events the manipulation of numerical simulations has proven to be invaluable.

This thesis consists of three individual research projects described in chapters 2, 3 and 4 where the dynamical properties of a decelerating blast wave in one and two-dimensions was discussed in detail, along with a connection between dynamics and radiation at the afterglow phase of the GRB.

In Chapter 2 we introduced the one-dimensional two-shell collision model at the GRB afterglow phase. According to this model the strong flaring activity observed in multiwavelength afterglow light curves can be the result of energy injection at the external shock of the blast wave at late times of its propagation. To test that model we performed 1D numerical simulations of a decelerating blast wave described by the Blandford and McKee self-similar solution followed by a cold ultra-relativistic shell ejected by the central engine which acts as the supply of energy in our model. We used unprecedented resolution in order to

properly resolve the Riemann problem arising in the second shell, a strategy that proved to be extremely valuable, despite the associated computational cost. Strong heating of the external shell is found to occur due to the propagation of the forward shock of the second shell inside the shocked external shell matter, while a similar process is taking place in the second shell due to the traverse of the reverse shock. We studied four different cases with varying Lorentz factor and energy for the two shells in order to test the association between dynamical behavior and emitted radiation for such a system. For that we constructed optical and radio light curves and emission images from the radiative regions of the blast wave using a numerical code specifically designed to accompany our dynamical simulations. The result was that strong flaring activity was observed (mainly in the optical and less in radio light curves) and it appeared more intense in the case where the highest Lorentz factor and energy were employed. In these calculations we tested the *synchrotron self-absorption* mechanism and the effects it has in our calculations. The radio light curves were found to be largely influenced by *ssa* which reduced the overall photon flux in the radio by a factor of 5. In addition, a time difference between the appearance of the optical and radio flare was observed due to the fact that the system is optically thick to synchrotron emission below the self-absorption frequency. Moreover, the increase in the observed flux appeared to be stronger in the case when a jetted outflow was used in order to reconstruct the emission, rather than a spherical explosion, which was explained in terms of contribution from high emission angles on the jet concealing the effects of the merger process.

Recent numerical simulations have questioned the large lateral expansion anticipated from analytical models for a relativistic jet in its afterglow phase. This inconsistency triggered our interest in confirming these numerical results for the case of a decelerating jet which is injected with energy. In a fashion similar to the one described earlier we performed two-dimensional simulations of a decelerating 2° half-opening angle jet and studied the spreading occuring in early phase of the deceleration of the jet due to the injection of energy from the accompanying shell. The results of this simulation, described in Chapter 3, confirmed the small spreading which was observed in previous two-dimensional simulations despite the presence of the collision happening between the two shells. However, a strong angular dependency of the dynamical properties of the jet is observed throughout the time period covered in our simulation which we postulate to have a strong effect on the light curves. More precisely, the collision between the two shells occurs first at high angles on the jet and at later times close to the axis indicating that a strong difference between on-axis and off-axis light curves should be anticipated for the same event.

In a more realistic approach, but only in one-dimension so far, numerical simulations have been performed describing the propagation of a GRB jet inside

the circumstellar bubble of a rotating star. Massive stars are now considered as the most likely progenitors for long GRBs. These kind of simulations therefore, present great interest in understanding the behavior of the blast wave while it expands inside the medium of its own progenitor. In that direction we decided to perform a complete set of simulations starting from the evolution of the circumstellar medium around the fast rotating progenitor and then in a second simulation to initiate the jet inside that medium. The first simulation showed that the termination shock of the circumstellar bubble appears strongly aspherical and has an ellipsoid shape with the major axis of the ellipse lying on the rotation axis of the star. The thin outer shell of the shocked interstellar matter however, appears to retain its spherical shape even when great pressure from the shocked wind is imposed during the critical rotation of the star. To investigate the dynamical and observational properties of the jet propagation inside this bubble we performed two simulations. A one-dimensional one which was carried out until the merged shock crossed the termination shock of the bubble and a two-dimensional one which is still in progress and for which the initial phase is presented in this thesis. For the one-dimensional simulation we calculated optical and radio light curves in a fashion similar to the one described in Chapter 1, and showed that the transition of the merged shock after the collision process between the two shells has ended iver the termination shock of the bubble has a rather insignificant result on the light curves. We argue that this is due to the fact that the termination shock is weak compared to the jet and determine the conditions under which such a tranition can account for a significant alteration of the observed flux. In the two-dimensional simulation we test the Vishniac-type instability that was first observed in relativistic blast waves from Meliani and Keppens 2010, and notice a similar behavior in our simulations as well. The instability starts to grow soon after the initiation of the simulation and covers a small region extending in front of the external shock in the post-shocked free-wind region of the circumstellar bubble. The evolution of the jet in later times will show us more about this instability and its behavior when the forward shock of the second shell catches up with the external shock.

Numerical investigation of GRB afterglows is a continuously growing branch in the field of high energy astrophysics. It has assisted significantly in understanding the nature of these exotic events but also triggered a significant step forward in the development of state of the art numerical codes and shock capturing schemes applicable in every aspect of numerical astrophysics. The complexity of the event and the multiscale character of the problem demands highly efficient algorithms in order to achieve maximal resolution without loss of generality. In the near future we plan to work on the direction of expanding the research presented in the four chapters of this thesis. One-dimensional dynamical simulations of high numerical accuracy such as the ones presented in chapter 2 can be used in order to fit the continuously growing amount of data

from light curves obtained by late ground based and space missions. Flares and rebrightenings explained by both external and internal shock collision models can be simulated and compared with observations in order to explain the complex variability observed in the afterglow. Furthermore restrictions in the physical properties of the source can be obtained by applying our model in late afterglow observations. A more pragmatic approach of the problem, such as the ones discussed in chapter 3 and 4, requires the use of multiple simulations of different physical characteristics as well as synthetic reconstruction of light curves from two-dimensional data. We intend to test our assumption of angular dependency of the shell-collision process as well as the effects arising from the propagation of the GRB jet in a circumstellar bubble in 2D by constructing and comparing on-axis and off-axis light curves.

Appendix A

Approximations in the radiation calculation

A.1 Slow cooling regime

The spectrum during the afterglow phase of a GRB is well described by synchrotron radiation emitted during the deceleration phase of a relativistic blast wave as described in chapter 2. Studied in detail, initially by Sari, Piran and Narayan [101] and later by Granot and Sari [40] which accounted for the effects arising from synchrotron self absorption, the shape of the spectrum is found to consist of several power-law segments joined together at the characteristic break frequencies. For the case examined in chapter 2 these are (1) the peak frequency ν_m corresponding to the emission from the electrons with the minimum Lorentz factor γ_m (2) the cooling frequency ν_c of an electron with cooling time equal to the dynamical time of the system and (3) the self-absorption frequency ν_{sa} below which synchrotron emission is reabsorbed from the emitting electrons.

Standard models assume that energy losses are negligible and do not influence the dynamics of the blast wave allowing therefore for an adiabatic description of the system. Electron cooling however has a predominant influence on the shape of the afterglow spectrum. Depending on how fast electrons cool down, compared to the dynamical time of the system, we distinguish two limiting cases: the *fast cooling* where all the energy of the electrons is radiated during the dynamical time of the system and the *slow cooling* where only high energy electrons are affected by the cooling. In the first case, the radiative efficiency of the shock is high and subsequently the structure of the downstream region

is highly determined by electron cooling. In the latter one, electrons which are close to the minimal Lorentz factor γ_m are not affected by cooling and the energy distribution remains unaltered. Hence it becomes clear that for the *slow cooling* regime, effects arising from electron cooling can be safely neglected allowing for significant simplification of the radiation calculations.

In our simulations we make sure that for times and frequencies under consideration we are always in the *slow cooling* regime. From Table 2 in [40] we calculate the break frequencies using the following formulas,

$$\nu_{sa} = 1.24 \frac{(p-1)^{3/5}}{(3p+2)^{3/5}} 10^9 (1+z)^{-1} \bar{\epsilon}_e^{-1} \epsilon_B^{1/5} n_0 E_{52}^{1/5}, \tag{A.1}$$

$$\nu_m = 3.73\,(p-0.67)\,10^{15} (1+z)^{1/2} E_{52}^{1/2} \bar{\epsilon}_e^2 \epsilon_B^{1/2} t_{days}^{-3/2}, \tag{A.2}$$

$$\nu_c = 6.37(p-0.46) 10^{13} e^{-1.16p} (1+z)^{-1/2} \epsilon_B^{-3/2} n_0^{-1} E_{52}^{-1/2} t_{days}^{-1/2}, \tag{A.3}$$

where p is the slope of the electron distribution, $\bar{\epsilon}_e = \epsilon_e\,(p-2)\,/\,(p-1)$ and the energy is normalized according to $E_{52} = E \times 10^{52}$ergs. z is the redshift, ϵ_E and ϵ_B are the fractions of the energy behind the shock going to particle acceleration and the generation of the magnetic field respectively, n_0 is the number density of the interstellar medium, and t_{days} is the observed time in days. The radiation calculations performed in this work are made for optical (5×10^{14} Hz) and radio (10^8 Hz) frequencies and span a time period from 0.001 to 10 days in the observer's frame of reference. Given this and using the values of the parameters ϵ_e and ϵ_B given in chapter 2 we can compute the values of the break frequencies throughout our simulation. We find that the self-absorption frequency satisfies $\nu_c >> \nu_{sa}$ and that ν_m and ν_c are bound by the following limiting values:

$$10^{10} Hz < \nu_m < 10^{16} Hz,$$

$$10^{17} Hz < \nu_c < 10^{20} Hz.$$

This ensures that we are constantly in the slow cooling regime and therefore can safely neglect synchrotron cooling while constructing optical and radio light curves.

A.2 Inverse Compton (IC) vs Synchrotron emission

A.2.1 Relative flux contribution

We discuss here the relative contributions of Inverse Compton (IC) scattering and synchrotron radiation in the shape of radio and optical light curves and spectra. In our calculations we have neglected effects arising from the Inverse Compton (IC) scattering of the emitted photons and have assumed that the dominant emitting mechanism is synchrotron radiation. Although in general this is true for all decelerating shocks in the late afterglow, this is not always the case for the early afterglow phase. Therefore, before neglecting the IC contribution from the radiation calculations one has to make sure of the relevant strength between IC and synchrotron emission. For that we follow the same strategy as described in [97]. The spectrum of IC scattering depends on both the incident flux and the energy distribution of the electrons. Considering a power-law distribution for the scattering electrons $N(\gamma)$ and an incident flux $\tilde{f}_{\nu_s}$ at the shock front, the emissivity of the IC component is given by (see [94] for a detailed derivation)

$$j_\nu^{IC} = 3\sigma_T \int_{\gamma_m}^{\infty} d\gamma N(\gamma) \int_0^1 dx g(x) \tilde{f}_{\nu_s}(x), \tag{A.4}$$

where $x \equiv \nu / \left(4\gamma^2 \nu_s\right)$ and the function $g(x) = 1 + x + 2x \ln x - 2x^2$ handles the angular dependency of the cross section for scattered electrons. Then the flux components of the IC and synchrotron radiation are given respectively by

$$f_\nu^{IC} = j_\nu^{IC} \frac{(4/3)R^3}{4\pi D^2}, \tag{A.5}$$

$$f_{\nu_s} = \tilde{f}_{\nu_s} \frac{4\pi R^2}{4\pi D^2}, \tag{A.6}$$

where R is the size of the shocked region and D is the distance to the observer. Rewritting A.5 after replacing the emissivity and substituting the synchrotron flux, we get the IC flux in relation to the synchrotron flux,

$$f_\nu^{IC} = R\sigma_T \int_{\gamma_m}^{\infty} d\gamma N(\gamma) \int_0^{x_0} dx f_{\nu_s}(x), \tag{A.7}$$

where the approximation $g(x) = 1$ for $0 < x < x_0$ was made. The value x_0 is determined by energy conservation, i.e. by setting $\int_0^1 x g(x) dx = \int_0^{x_0} x dx$.

For the slow cooling regime described in the previous section ($\nu_{sa} << \nu_m << \nu_c$) this equation yields (see [97] and [101] for a more detailed derivation)

$$f_\nu^{IC}(\nu_m^{IC}) \simeq 4\sigma_T R n_0 f_{\nu_s}(\nu_m^s) x_0 \frac{(p-1)(p+1/3)}{(p-1/3)(p+1)^2}, \tag{A.8}$$

where $f_\nu^{IC}(\nu_m^{IC})$ and $f_{\nu_s}(\nu_m^s)$ are the values of the flux at the peak of the IC and synchrotron component respectively and n_0 is the ambient density. The relative strength of the two mechanisms can then be written in the form

$$\frac{f_{max}^{IC}}{f_{max}^s} \sim \sigma_T n R. \tag{A.9}$$

For the value of the circumburst density used throughout our simulations $n = 1cm^{-3}$ and the radius of the shock $R = 10^{17} - 10^{18}$cm this value remains for the entire simulation well below unity ensuring that synchrotron emission will dominate over Inverse Compton for the entire run of the simulation.

A.2.2 Inverse Compton cooling vs synchrotron cooling

Apart from the direct contribution of en extra emission component, Inverse Compton also affects the overall spectrum by dominating the electron cooling and thus reducing the amount of electrons available for synchrotron radiation. Since electrons lose energy through both synchrotron and synchrotron self-Compton mechanism it is important to calculate the relative contribution in electron cooling of the two emitting mechanisms before dismissing Inverse Compton from our calculations. As described in [97] and [94] this property is quantified by the Compton-Y parameter given by the ratio of emitted power of the two mechanisms,

$$Y = \frac{P_{IC}}{P_{syn}} = \frac{(4/3)\sigma_T \gamma^2 \beta^2 U_{ph}}{(4/3)\sigma_T \gamma^2 \beta^2 U_B} = \frac{U_{ph}}{U_B} = \frac{U_{syn}}{U_B}, \tag{A.10}$$

where U_B is the energy density of the magnetic field, and U_{ph} is the energy density of the photons available for inverse compton scattering. In the case of synchrotron self-Compton this is given by the energy density of synchrotron radiation U_{syn}. Assuming that only a fraction η of the total electron energy is radiated away through both synchrotron and Inverse Compton emission, we can calculate the energy density of synchrotron radiation as a fraction of the energy density of all the accelerated electrons U_e via, $U_{syn} = \eta U_e/(1+Y)$. Assuming that part of the total thermal energy behind the shock front is used to accelerate

the electrons and the rest to amplify the magnetic field we can introduce the fractions, $\epsilon_e = U_e/e_{th}$ and $\epsilon_B = U_B/e_{th}$ and rewrite equation A.10 as follows,

$$Y = \frac{\eta\epsilon_e}{\epsilon_B(1+Y)}. \tag{A.11}$$

Solving the quadratic equation yields,

$$Y = \frac{-1 \pm \sqrt{1+4\eta\epsilon_e/\epsilon_B}}{2} \simeq \begin{cases} \frac{\eta\epsilon_e}{\epsilon_B}, & \text{if } \frac{\eta\epsilon_e}{\epsilon_B} \ll 1, \\ \left(\frac{\eta\epsilon_e}{\epsilon_B}\right)^{1/2}, & \text{if } \frac{\eta\epsilon_e}{\epsilon_B} \gg 1. \end{cases} \tag{A.12}$$

It becomes clear that if $\eta\epsilon_e/\epsilon_B \ll 1$, electron cooling due to Inverse Compton scattering can be neglected. However, estimates based on observations suggest that $\epsilon_B < \epsilon_e$, with a ratio $\epsilon_e/\epsilon_B \sim 10$ as used in our simulations. In that case in order to safely neglect Inverse Compton cooling we have to make sure that η is sufficently small (by definition $\eta \leq 1$). For the slow cooling regime, which we showed to be the case for our simulations, η is defined as $\eta = (\gamma_c/\gamma_m)^{2-p} = (\nu_c/\nu_m)^{-(p-2)/2}$. For the range of the break frequencies computed in A.1 we have $0.017 < \eta < 0.1$ throughout the time period described in the simulations allowing therefore with little loss of generality to neglect effects from Inverse Compton electron cooling.

We have to note however that accounting for higher than the optical frequencies (such as X-rays or gamma-rays) requires the inclusion of Inverse Compton scattering since it affects predominantly the shape of both light curves and spectra.

Bibliography

[1] Abdo, A. A., Ackermann, M., Ajello, M., Allafort, A., Antolini, E., Atwood, W. B., Axelsson, M., Baldini, L., Ballet, J., Barbiellini, G., and et al. Fermi Large Area Telescope First Source Catalog. *188* (June 2010), 405–436. pages 4

[2] Abdo, A. A., Ackermann, M., Ajello, M., Atwood, W. B., Axelsson, M., Baldini, L., Ballet, J., Band, D. L., Barbiellini, G., Bastieri, D., and et al. Fermi/Large Area Telescope Bright Gamma-Ray Source List. *183* (July 2009), 46–66. pages 4

[3] Abdo, A. A., Ackermann, M., Arimoto, M., Asano, K., Atwood, W. B., Axelsson, M., Baldini, L., Ballet, J., Band, D. L., Barbiellini, G., and et al. Fermi Observations of High-Energy Gamma-Ray Emission from GRB 080916C. *Science 323* (Mar. 2009), 1688–. pages 4

[4] Antonelli, L. A., Testa, V., Romano, P., Guetta, D., Torii, K., D'Elia, V., Malesani, D., Chincarini, G., Covino, S., D'Avanzo, P., Della Valle, M., Fiore, F., Fugazza, D., Moretti, A., Stella, L., Tagliaferri, G., Barthelmy, S., Burrows, D., Campana, S., Capalbi, M., Cusumano, G., Gehrels, N., Giommi, P., Lazzati, D., La Parola, V., Mangano, V., Mineo, T., Nousek, J., O'Brien, P. T., and Perri, M. The multiwavelength afterglow of GRB 050721: a puzzling rebrightening seen in the optical but not in the X-ray. *456* (Sept. 2006), 509–515. pages 13

[5] Atwood, W. B., Abdo, A. A., Ackermann, M., Althouse, W., Anderson, B., Axelsson, M., Baldini, L., Ballet, J., Band, D. L., Barbiellini, G., and et al. The Large Area Telescope on the Fermi Gamma-Ray Space Telescope Mission. *697* (June 2009), 1071–1102. pages 4

[6] Band, D., Ford, L., Matteson, J., Lestrade, J. P., Teegarden, B., Schaefer, B., Cline, T., Briggs, M., Paciesas, W., and Pendleton, G. BATSE spectroscopy detector calibration. *Experimental Astronomy 2* (Sept. 1992), 307–330. pages 2

[7] Band, D., Matteson, J., Ford, L., Schaefer, B., Palmer, D., Teegarden, B., Cline, T., Briggs, M., Paciesas, W., Pendleton, G., Fishman, G., Kouveliotou, C., Meegan, C., Wilson, R., and Lestrade, P. BATSE observations of gamma-ray burst spectra. I - Spectral diversity. *413* (Aug. 1993), 281–292. pages 4

[8] Barbier, L. M., Barthelmy, S., Cummings, J., Gehrels, N., Krimm, H., Markwardt, C., Mushotzky, R., Parsons, A., Sakamoto, T., Tueller, J., Fenimore, E., Palmer, D., Skinner, G., and Swift-BAT Team. Swift-BAT: Transient Source Monitoring. In *American Astronomical Society Meeting Abstracts* (Dec. 2005), vol. 37 of *Bulletin of the American Astronomical Society*, p. 1187. pages 3

[9] Berger, E., Kulkarni, S. R., Pooley, G., Frail, D. A., McIntyre, V., Wark, R. M., Sari, R., Soderberg, A. M., Fox, D. W., Yost, S., and Price, P. A. A common origin for cosmic explosions inferred from calorimetry of GRB030329. *426* (Nov. 2003), 154–157. pages 3

[10] Blandford, R. D., and McKee, C. F. Fluid dynamics of relativistic blast waves. *Physics of Fluids 19* (Aug. 1976), 1130–1138. pages 20, 22, 33, 38, 60, 97

[11] Bloom, J. S., Kulkarni, S. R., and Djorgovski, S. G. The Observed Offset Distribution of Gamma-Ray Bursts from Their Host Galaxies: A Robust Clue to the Nature of the Progenitors. *123* (Mar. 2002), 1111–1148. pages 6

[12] Bloom, J. S., Prochaska, J. X., Pooley, D., Blake, C. H., Foley, R. J., Jha, S., Ramirez-Ruiz, E., Granot, J., Filippenko, A. V., Sigurdsson, S., Barth, A. J., Chen, H.-W., Cooper, M. C., Falco, E. E., Gal, R. R., Gerke, B. F., Gladders, M. D., Greene, J. E., Hennanwi, J., Ho, L. C., Hurley, K., Koester, B. P., Li, W., Lubin, L., Newman, J., Perley, D. A., Squires, G. K., and Wood-Vasey, W. M. Closing in on a Short-Hard Burst Progenitor: Constraints from Early-Time Optical Imaging and Spectroscopy of a Possible Host Galaxy of GRB 050509b. *638* (Feb. 2006), 354–368. pages 3

[13] Boella, G., Butler, R. C., Perola, G. C., Piro, L., Scarsi, L., and Bleeker, J. A. M. BeppoSAX, the wide band mission for X-ray astronomy. *122* (Apr. 1997), 299–307. pages 2

[14] Burrows, D. N., Falcone, A., Chincarini, G., Morris, D., Romano, P., Hill, J. E., Godet, O., Moretti, A., Krimm, H., Osborne, J. P., Racusin, J., Mangano, V., Page, K., Perri, M., Stroh, M., and Swift XRT Team. X-ray flares in early GRB afterglows. *Royal Society of London Philosophical Transactions Series A 365* (May 2007), 1213–1226. pages 60

[15] Burrows, D. N., Romano, P., Falcone, A., Kobayashi, S., Zhang, B., Moretti, A., O'Brien, P. T., Goad, M. R., Campana, S., Page, K. L., Angelini, L., Barthelmy, S., Beardmore, A. P., Capalbi, M., Chincarini, G., Cummings, J., Cusumano, G., Fox, D., Giommi, P., Hill, J. E., Kennea, J. A., Krimm, H., Mangano, V., Marshall, F., Mészáros, P., Morris, D. C., Nousek, J. A., Osborne, J. P., Pagani, C., Perri, M., Tagliaferri, G., Wells, A. A., Woosley, S., and Gehrels, N. Bright X-ray Flares in Gamma-Ray Burst Afterglows. *Science 309* (Sept. 2005), 1833–1835. pages 15, 32

[16] Cannizzo, J. K., Gehrels, N., and Vishniac, E. T. A Numerical Gamma-Ray Burst Simulation Using Three-Dimensional Relativistic Hydrodynamics: The Transition from Spherical to Jetlike Expansion. *601* (Jan. 2004), 380–390. pages 19

[17] Castor, J. I., Abbott, D. C., and Klein, R. I. Radiation-driven winds in Of stars. *195* (Jan. 1975), 157–174. pages 83

[18] Cavallo, G., and Rees, M. J. A qualitative study of cosmic fireballs and gamma-ray bursts. *183* (May 1978), 359–365. pages 8

[19] Chupp, E. L., Cline, T. L., Evans, W. D., Fenimore, E., Gorenstein, P., Grindlay, J., Lamb, D. Q., Lewin, W. H. G., Lingenfelter, R. E., Matteson, J. L., Ramaty, R., Ricker, G. R., Share, G., Teegarden, B., and Woosley, S. E. The High Energy Transient Explorer (HETE). In *American Institute of Physics Conference Series* (May 1984), S. E. Woosley, Ed., vol. 115 of *American Institute of Physics Conference Series*, pp. 709–714. pages 3

[20] De Colle, F., Granot, J., López-Cámara, D., and Ramirez-Ruiz, E. Gamma-Ray Burst Dynamics and Afterglow Radiation from Adaptive Mesh Refinement, Special Relativistic Hydrodynamic Simulations. *746* (Feb. 2012), 122. pages 60, 61, 65

[21] De Colle, F., Ramirez-Ruiz, E., Granot, J., and Lopez-Camara, D. Simulations of Gamma-Ray Burst Jets in a Stratified External Medium: Dynamics, Afterglow Light Curves, Jet Breaks, and Radio Calorimetry. *751* (May 2012), 57. pages 19, 60, 61, 74, 81

[22] Della Valle, M., Chincarini, G., Panagia, N., Tagliaferri, G., Malesani, D., Testa, V., Fugazza, D., Campana, S., Covino, S., Mangano, V., Antonelli, L. A., D'Avanzo, P., Hurley, K., Mirabel, I. F., Pellizza, L. J., Piranomonte, S., and Stella, L. An enigmatic long-lasting γ-ray burst not accompanied by a bright supernova. *444* (Dec. 2006), 1050–1052. pages 3

[23] Dermer, C. D. Rapid X-Ray Declines and Plateaus in Swift GRB Light Curves Explained by a Highly Radiative Blast Wave. *664* (July 2007), 384–396. pages 7

[24] Drenkhahn, G., and Spruit, H. C. Efficient acceleration and radiation in Poynting flux powered GRB outflows. *391* (Sept. 2002), 1141–1153. pages 7

[25] Dwarkadas, V. V., and Owocki, S. P. Radiatively Driven Winds and the Shaping of Bipolar Luminous Blue Variable Nebulae. *581* (Dec. 2002), 1337–1343. pages 83

[26] Falcone, A. D., Burrows, D. N., Lazzati, D., Campana, S., Kobayashi, S., Zhang, B., Mészáros, P., Page, K. L., Kennea, J. A., Romano, P., Pagani, C., Angelini, L., Beardmore, A. P., Capalbi, M., Chincarini, G., Cusumano, G., Giommi, P., Goad, M. R., Godet, O., Grupe, D., Hill, J. E., La Parola, V., Mangano, V., Moretti, A., Nousek, J. A., O'Brien, P. T., Osborne, J. P., Perri, M., Tagliaferri, G., Wells, A. A., and Gehrels, N. The Giant X-Ray Flare of GRB 050502B: Evidence for Late-Time Internal Engine Activity. *641* (Apr. 2006), 1010–1017. pages 32

[27] Fruchter, A. S., Levan, A. J., Strolger, L., Vreeswijk, P. M., Thorsett, S. E., Bersier, D., Burud, I., Castro Cerón, J. M., Castro-Tirado, A. J., Conselice, C., Dahlen, T., Ferguson, H. C., Fynbo, J. P. U., Garnavich, P. M., Gibbons, R. A., Gorosabel, J., Gull, T. R., Hjorth, J., Holland, S. T., Kouveliotou, C., Levay, Z., Livio, M., Metzger, M. R., Nugent, P. E., Petro, L., Pian, E., Rhoads, J. E., Riess, A. G., Sahu, K. C., Smette, A., Tanvir, N. R., Wijers, R. A. M. J., and Woosley, S. E. Long γ-ray bursts and core-collapse supernovae have different environments. *441* (May 2006), 463–468. pages 6

[28] Fryxell, B., Olson, K., Ricker, P., Timmes, F. X., Zingale, M., Lamb, D. Q., MacNeice, P., Rosner, R., Truran, J. W., and Tufo, H. FLASH: An Adaptive Mesh Hydrodynamics Code for Modeling

Astrophysical Thermonuclear Flashes. *131* (Nov. 2000), 273–334. pages 26

[29] Galama, T., Groot, P. J., Van Paradijs, J., Kouveliotou, C., Robinson, C. R., Fishman, G. J., Meegan, C. A., Sahu, K. C., Livio, M., Petro, L., Macchetto, F. D., Heise, J., Int Zand, J., Strom, R. G., Telting, J., Rutten, R. G. M., Pettini, M., Tanvir, N., and Bloom, J. The Decay of Optical Emission from the gamma-Ray Burst GRB970228. *387* (May 1997), 479. pages 12

[30] Garcia-Segura, G., Mac Low, M.-M., and Langer, N. The dynamical evolution of circumstellar gas around massive stars. I. The impact of the time sequence Ostar - LBV - WR star. *305* (Jan. 1996), 229. pages 82

[31] Gehrels, N., Chincarini, G., Giommi, P., Mason, K. O., Nousek, J. A., Wells, A. A., White, N. E., Barthelmy, S. D., Burrows, D. N., Cominsky, L. R., Hurley, K. C., Marshall, F. E., Mészáros, P., Roming, P. W. A., Angelini, L., Barbier, L. M., Belloni, T., Campana, S., Caraveo, P. A., Chester, M. M., Citterio, O., Cline, T. L., Cropper, M. S., Cummings, J. R., Dean, A. J., Feigelson, E. D., Fenimore, E. E., Frail, D. A., Fruchter, A. S., Garmire, G. P., Gendreau, K., Ghisellini, G., Greiner, J., Hill, J. E., Hunsberger, S. D., Krimm, H. A., Kulkarni, S. R., Kumar, P., Lebrun, F., Lloyd-Ronning, N. M., Markwardt, C. B., Mattson, B. J., Mushotzky, R. F., Norris, J. P., Osborne, J., Paczynski, B., Palmer, D. M., Park, H.-S., Parsons, A. M., Paul, J., Rees, M. J., Reynolds, C. S., Rhoads, J. E., Sasseen, T. P., Schaefer, B. E., Short, A. T., Smale, A. P., Smith, I. A., Stella, L., Tagliaferri, G., Takahashi, T., Tashiro, M., Townsley, L. K., Tueller, J., Turner, M. J. L., Vietri, M., Voges, W., Ward, M. J., Willingale, R., Zerbi, F. M., and Zhang, W. W. The Swift Gamma-Ray Burst Mission. *611* (Aug. 2004), 1005–1020. pages 3, 60

[32] Gehrels, N., Ramirez-Ruiz, E., and Fox, D. B. Gamma-Ray Bursts in the Swift Era. *47* (Sept. 2009), 567–617. pages 4

[33] Gehrels, N., Sarazin, C. L., O'Brien, P. T., Zhang, B., Barbier, L., Barthelmy, S. D., Blustin, A., Burrows, D. N., Cannizzo, J., Cummings, J. R., Goad, M., Holland, S. T., Hurkett, C. P., Kennea, J. A., Levan, A., Markwardt, C. B., Mason, K. O., Meszaros, P., Page, M., Palmer, D. M., Rol, E., Sakamoto, T., Willingale, R., Angelini, L., Beardmore, A., Boyd, P. T.,

Breeveld, A., Campana, S., Chester, M. M., Chincarini, G., Cominsky, L. R., Cusumano, G., de Pasquale, M., Fenimore, E. E., Giommi, P., Gronwall, C., Grupe, D., Hill, J. E., Hinshaw, D., Hjorth, J., Hullinger, D., Hurley, K. C., Klose, S., Kobayashi, S., Kouveliotou, C., Krimm, H. A., Mangano, V., Marshall, F. E., McGowan, K., Moretti, A., Mushotzky, R. F., Nakazawa, K., Norris, J. P., Nousek, J. A., Osborne, J. P., Page, K., Parsons, A. M., Patel, S., Perri, M., Poole, T., Romano, P., Roming, P. W. A., Rosen, S., Sato, G., Schady, P., Smale, A. P., Sollerman, J., Starling, R., Still, M., Suzuki, M., Tagliaferri, G., Takahashi, T., Tashiro, M., Tueller, J., Wells, A. A., White, N. E., and Wijers, R. A. M. J. A short γ-ray burst apparently associated with an elliptical galaxy at redshift z = 0.225. *437* (Oct. 2005), 851–854. pages 3

[34] Goedbloed, J. P., Keppens, R., and Poedts, S. *Advanced Magnetohydrodynamics With applications to Laboratory and Astrophysical Plasmas*. 2010. pages 82

[35] Goodman, J. Are gamma-ray bursts optically thick? *308* (Sept. 1986), L47–L50. pages 8

[36] Granot, J., Miller, M., Piran, T., Suen, W. M., and Hughes, P. A. Light Curves from an Expanding Relativistic Jet. In *Gamma-ray Bursts in the Afterglow Era* (2001), E. Costa, F. Frontera, and J. Hjorth, Eds., p. 312. pages 33

[37] Granot, J., Nakar, E., and Piran, T. Astrophysics: refreshed shocks from a γ-ray burst. *426* (Nov. 2003), 138–139. pages 60

[38] Granot, J., and Piran, T. On the lateral expansion of gamma-ray burst jets. *421* (Mar. 2012), 570–587. pages 61

[39] Granot, J., Piran, T., and Sari, R. Synchrotron Self-Absorption in Gamma-Ray Burst Afterglow. *527* (Dec. 1999), 236–246. pages 43

[40] Granot, J., and Sari, R. The Shape of Spectral Breaks in Gamma-Ray Burst Afterglows. *568* (Apr. 2002), 820–829. pages 49, 50, 107, 108

[41] Huang, Y. F., Cheng, K. S., and Gao, T. T. Modeling the Optical Afterglow of GRB 030329. *637* (Feb. 2006), 873–879. pages 3

[42] Ioka, K., Kobayashi, S., and Zhang, B. Variabilities of Gamma-Ray Burst Afterglows: Long-acting Engine, Anisotropic Jet, or Many Fluctuating Regions? *631* (Sept. 2005), 429–434. pages 32

[43] Keppens, R., Meliani, Z., van Marle, A. J., Delmont, P., Vlasis, A., and van der Holst, B. Parallel, grid-adaptive approaches for relativistic hydro and magnetohydrodynamics. *Journal of Computational Physics 231* (Feb. 2012), 718–744. pages xii, 26, 27, 63

[44] Keppens, R., Nool, M., Tóth, G., and Goedbloed, J. P. Adaptive Mesh Refinement for conservative systems: multi-dimensional efficiency evaluation. *Computer Physics Communications 153* (July 2003), 317–339. pages 33

[45] King, A., O'Brien, P. T., Goad, M. R., Osborne, J., Olsson, E., and Page, K. Gamma-Ray Bursts: Restarting the Engine. *630* (Sept. 2005), L113–L115. pages 32, 60

[46] Klebesadel, R. W., Strong, I. B., and Olson, R. A. Observations of Gamma-Ray Bursts of Cosmic Origin. *182* (June 1973), L85. pages 2

[47] Klotz, A., Gendre, B., Stratta, G., Galli, A., Corsi, A., Preger, B., Cutini, S., Pélangeon, A., Atteia, J. L., Boër, M., and Piro, L. Early emission of rising optical afterglows: the case of GRB 060904B and GRB 070420. *483* (June 2008), 847–855. pages 13

[48] Kobayashi, S., Piran, T., and Sari, R. Can Internal Shocks Produce the Variability in Gamma-Ray Bursts? *490* (Nov. 1997), 92. pages 7

[49] Kouveliotou, C., Meegan, C. A., Fishman, G. J., Bhat, N. P., Briggs, M. S., Koshut, T. M., Paciesas, W. S., and Pendleton, G. N. Identification of two classes of gamma-ray bursts. *413* (Aug. 1993), L101–L104. pages 4

[50] Krühler, T., Greiner, J., McBreen, S., Klose, S., Rossi, A., Afonso, P., Clemens, C., Filgas, R., Yoldaş, A. K., Szokoly, G. P., and Yoldaş, A. Correlated Optical and X-Ray Flares in the Afterglow of XRF 071031. *697* (May 2009), 758–768. pages 13

[51] Kumar, P., and Piran, T. Some Observational Consequences of Gamma-Ray Burst Shock Models. *532* (Mar. 2000), 286–293. pages 60

[52] Lazzati, D., Rossi, E., Covino, S., Ghisellini, G., and Malesani, D. The afterglow of GRB 021004: Surfing on density waves. *396* (Dec. 2002), L5–L9. pages 32

[53] Levesque, E. M., Kewley, L. J., Graham, J. F., and Fruchter, A. S. A High-metallicity Host Environment for the Long-duration GRB 020819. *712* (Mar. 2010), L26–L30. pages 6

[54] Lu, Y., Huang, Y. F., and Zhang, S. N. A Tidal Disruption Model for the Gamma-Ray Burst of GRB 060614. *684* (Sept. 2008), 1330–1335. pages 4

[55] Lyutikov, M., and Blandford, R. Electromagnetic explosions in Gamma-Ray Bursts. In *AAS/High Energy Astrophysics Division #7* (Mar. 2003), vol. 35 of *Bulletin of the American Astronomical Society*, p. 622. pages 7

[56] Lyutikov, M., and Blandford, R. Gamma Ray Bursts as Electromagnetic Outflows. *ArXiv Astrophysics e-prints* (Dec. 2003). pages 10, 11

[57] MacFadyen, A. I., and Woosley, S. E. Collapsars: Gamma-Ray Bursts and Explosions in "Failed Supernovae". *524* (Oct. 1999), 262–289. pages 6, 60

[58] Maeder, A., and Meynet, G. Stellar evolution with rotation and magnetic fields. I. The relative importance of rotational and magnetic effects. *411* (Dec. 2003), 543–552. pages 83

[59] Mathews, W. G. The Hydromagnetic Free Expansion of a Relativistic Gas. *165* (Apr. 1971), 147. pages 28, 63

[60] Maxham, A., and Zhang, B. Modeling Gamma-Ray Burst X-Ray Flares Within the Internal Shock Model. *707* (Dec. 2009), 1623–1633. pages 15

[61] Medvedev, M. V., and Loeb, A. Generation of Magnetic Fields in the Relativistic Shock of Gamma-Ray Burst Sources. *526* (Dec. 1999), 697–706. pages 27, 43

[62] Meegan, C. A., Fishman, G. J., Wilson, R. B., Horack, J. M., Brock, M. N., Paciesas, W. S., Pendleton, G. N., and Kouveliotou, C. Spatial distribution of gamma-ray bursts observed by BATSE. *355* (Jan. 1992), 143–145. pages 2

[63] Melandri, A., Mundell, C. G., Kobayashi, S., Guidorzi, C., Gomboc, A., Steele, I. A., Smith, R. J., Bersier, D., Mottram, C. J., Carter, D., Bode, M. F., O'Brien, P. T., Tanvir, N. R., Rol, E., and Chapman, R. The Early-Time Optical Properties of Gamma-Ray Burst Afterglows. *686* (Oct. 2008), 1209–1230. pages 13

[64] Meliani, Z., and Keppens, R. Dynamics and stability of relativistic gamma-ray-bursts blast waves. *520* (Sept. 2010), L3. pages 19, 30, 33, 60, 80, 100, 101

[65] Meliani, Z., Keppens, R., Casse, F., and Giannios, D. AMRVAC and relativistic hydrodynamic simulations for gamma-ray burst afterglow phases. *376* (Apr. 2007), 1189–1200. pages 19, 33, 34

[66] Meliani, Z., Sauty, C., Tsinganos, K., and Vlahakis, N. Relativistic Parker winds with variable effective polytropic index. *425* (Oct. 2004), 773–781. pages 63

[67] Meszaros, P., and Rees, M. J. Optical and Long-Wavelength Afterglow from Gamma-Ray Bursts. *476* (Feb. 1997), 232. pages 34

[68] Metzger, M. R., Djorgovski, S. G., Kulkarni, S. R., Steidel, C. C., Adelberger, K. L., Frail, D. A., Costa, E., and Frontera, F. Spectral constraints on the redshift of the optical counterpart to the γ-ray burst of 8 May 1997. *387* (June 1997), 878–880. pages 3

[69] Mignone, A., Bodo, G., Massaglia, S., Matsakos, T., Tesileanu, O., Zanni, C., and Ferrari, A. PLUTO: A Numerical Code for Computational Astrophysics. *170* (May 2007), 228–242. pages 26

[70] Mimica, P., and Giannios, D. Gamma-ray burst afterglow light curves from realistic density profiles. *418* (Nov. 2011), 583–590. pages 80

[71] Mimica, P., Giannios, D., and Aloy, M. A. Deceleration of arbitrarily magnetized GRB ejecta: the complete evolution. *494* (Feb. 2009), 879–890. pages 33, 80

[72] Molinari, E., Vergani, S. D., Malesani, D., Covino, S., D'Avanzo, P., Chincarini, G., Zerbi, F. M., Antonelli, L. A., Conconi, P., Testa, V., Tosti, G., Vitali, F., D'Alessio, F., Malaspina, G., Nicastro, L., Palazzi, E., Guetta, D., Campana, S., Goldoni, P., Masetti, N., Meurs, E. J. A., Monfardini, A., Norci, L., Pian, E., Piranomonte, S., Rizzuto, D., Stefanon, M., Stella, L., Tagliaferri, G., Ward, P. A., Ihle, G., Gonzalez, L., Pizarro, A., Sinclaire, P., and Valenzuela, J. REM observations of GRB 060418 and GRB 060607A: the onset of the afterglow and the initial fireball Lorentz factor determination. *469* (July 2007), L13–L16. pages 13

[73] Morris, D. C., Burrows, D. N., Hill, J. E., Kennea, J., Racusin, J., Wood, P., Mangels, C., Klar, R., Angelini, L., and Tamburelli, F. Temperature dependent calibration products of the SWIFT x-ray telescope. In *Society of Photo-Optical Instrumentation Engineers (SPIE) Conference Series* (Jan. 2005), O. H. W. Siegmund, Ed., vol. 5898 of *Society of Photo-Optical Instrumentation Engineers (SPIE) Conference Series*, pp. 441–449. pages 3

[74] Nakar, E., and Granot, J. Smooth light curves from a bumpy ride: relativistic blast wave encounters a density jump. *380* (Oct. 2007), 1744–1760. pages 32, 80

[75] Narayan, R., Paczynski, B., and Piran, T. Gamma-ray bursts as the death throes of massive binary stars. *395* (Aug. 1992), L83–L86. pages 32

[76] Nousek, J. A., Kouveliotou, C., Grupe, D., Page, K. L., Granot, J., Ramirez-Ruiz, E., Patel, S. K., Burrows, D. N., Mangano, V., Barthelmy, S., Beardmore, A. P., Campana, S., Capalbi, M., Chincarini, G., Cusumano, G., Falcone, A. D., Gehrels, N., Giommi, P., Goad, M. R., Godet, O., Hurkett, C. P., Kennea, J. A., Moretti, A., O'Brien, P. T., Osborne, J. P., Romano, P., Tagliaferri, G., and Wells, A. A. Evidence for a Canonical Gamma-Ray Burst Afterglow Light Curve in the Swift XRT Data. *642* (May 2006), 389–400. pages 32

[77] O'Brien, P., Osborne, J., and Mason, K. Gamma-ray bursts and Swift. *Astronomy and Geophysics 46*, 3 (June 2005), 030000–3. pages 3

[78] O'Brien, P. T., Willingale, R., Osborne, J., Goad, M. R., Page, K. L., Vaughan, S., Rol, E., Beardmore, A., Godet, O., Hurkett, C. P., Wells, A., Zhang, B., Kobayashi, S., Burrows, D. N., Nousek, J. A., Kennea, J. A., Falcone, A., Grupe, D., Gehrels, N., Barthelmy, S., Cannizzo, J., Cummings, J., Hill, J. E., Krimm, H., Chincarini, G., Tagliaferri, G., Campana, S., Moretti, A., Giommi, P., Perri, M., Mangano, V., and LaParola, V. The Early X-Ray Emission from GRBs. *647* (Aug. 2006), 1213–1237. pages xi, 13

[79] O'Shea, B. W., Nagamine, K., Springel, V., Hernquist, L., and Norman, M. L. Comparing AMR and SPH Cosmological Simulations. I. Dark Matter and Adiabatic Simulations. *160* (Sept. 2005), 1–27. pages 26

[80] Paczynski, B. Gamma-ray bursters at cosmological distances. *308* (Sept. 1986), L43–L46. pages 8

[81] Paczynski, B. Are Gamma-Ray Bursts in Star-Forming Regions? *494* (Feb. 1998), L45. pages 6

[82] Paczynski, B., and Xu, G. Neutrino bursts from gamma-ray bursts. *427* (June 1994), 708–713. pages 8

[83] Pedersen, H., Jaunsen, A. O., Grav, T., Ostensen, R., Andersen, M. I., Wold, M., Kristen, H., Broeils, A., Naeslund, M., Fransson, C., Lacy, M., Castro-Tirado, A. J., Gorosabel, J., Rodriguez Espinosa, J. M., Perez, A. M., Wolf, C.,

Fockenbrock, R., Hjorth, J., Muhli, P., Hakala, P., Piro, L., Feroci, M., Costa, E., Nicastro, L., Palazzi, E., Frontera, F., Monaldi, L., and Heise, J. Evidence for Diverse Optical Emission from Gamma-Ray Burst Sources. *496* (Mar. 1998), 311. pages xi, 13

[84] Perna, R., Armitage, P. J., and Zhang, B. Flares in Long and Short Gamma-Ray Bursts: A Common Origin in a Hyperaccreting Accretion Disk. *636* (Jan. 2006), L29–L32. pages 32

[85] Piran, T. Gamma-ray bursts and the fireball model. *314* (June 1999), 575–667. pages 9

[86] Piran, T. The physics of gamma-ray bursts. *Reviews of Modern Physics 76* (Oct. 2004), 1143–1210. pages 4, 32

[87] Proga, D., MacFadyen, A. I., Armitage, P. J., and Begelman, M. C. Axisymmetric Magnetohydrodynamic Simulations of the Collapsar Model for Gamma-Ray Bursts. *599* (Dec. 2003), L5–L8. pages 10

[88] Proga, D., and Zhang, B. The late time evolution of gamma-ray bursts: ending hyperaccretion and producing flares. *370* (July 2006), L61–L65. pages 32

[89] Rees, M. J., and Meszaros, P. Relativistic fireballs - Energy conversion and time-scales. *258* (Sept. 1992), 41P–43P. pages 7

[90] Rees, M. J., and Meszaros, P. Unsteady outflow models for cosmological gamma-ray bursts. *430* (Aug. 1994), L93–L96. pages 7, 9, 32

[91] Rhoads, J. E. The Dynamics and Light Curves of Beamed Gamma-Ray Burst Afterglows. *525* (Nov. 1999), 737–749. pages 60, 80

[92] Romano, P., Moretti, A., Banat, P. L., Burrows, D. N., Campana, S., Chincarini, G., Covino, S., Malesani, D., Tagliaferri, G., Kobayashi, S., Zhang, B., Falcone, A. D., Angelini, L., Barthelmy, S., Beardmore, A. P., Capalbi, M., Cusumano, G., Giommi, P., Goad, M. R., Godet, O., Grupe, D., Hill, J. E., Kennea, J. A., La Parola, V., Mangano, V., Mészáros, P., Morris, D. C., Nousek, J. A., O'Brien, P. T., Osborne, J. P., Parsons, A., Perri, M., Pagani, C., Page, K. L., Wells, A. A., and Gehrels, N. X-ray flare in XRF 050406: evidence for prolonged engine activity. *450* (Apr. 2006), 59–68. pages 32

[93] Ruderman, M. Theories of gamma-ray bursts. In *Seventh Texas Symposium on Relativistic Astrophysics* (Oct. 1975), P. G. Bergman,

E. J. Fenyves, and L. Motz, Eds., vol. 262 of *Annals of the New York Academy of Sciences*, pp. 164–180. pages 9

[94] Rybicki, G. B., and Lightman, A. P. *Radiative processes in astrophysics*. 1979. pages 109, 110

[95] Rykoff, E. S., Aharonian, F., Akerlof, C. W., Ashley, M. C. B., Barthelmy, S. D., Flewelling, H. A., Gehrels, N., Göğüş, E., Güver, T., Kiziloğlu, Ü., Krimm, H. A., McKay, T. A., Özel, M., Phillips, A., Quimby, R. M., Rowell, G., Rujopakarn, W., Schaefer, B. E., Smith, D. A., Vestrand, W. T., Wheeler, J. C., Wren, J., Yuan, F., and Yost, S. A. Looking Into the Fireball: ROTSE-III and Swift Observations of Early Gamma-ray Burst Afterglows. *702* (Sept. 2009), 489–505. pages 13

[96] Sahu, K. C., Livio, M., Petro, L., Macchetto, F. D., van Paradijs, J., Kouveliotou, C., Fishman, G. J., Meegan, C. A., Groot, P. J., and Galama, T. The optical counterpart to gamma-ray burst GRB 970228 observed using the Hubble Space Telescope. *387* (May 1997), 476–478. pages 12

[97] Sari, R., and Esin, A. A. On the Synchrotron Self-Compton Emission from Relativistic Shocks and Its Implications for Gamma-Ray Burst Afterglows. *548* (Feb. 2001), 787–799. pages 50, 109, 110

[98] Sari, R., and Piran, T. Cosmological gamma-ray bursts: internal versus external shocks. *287* (May 1997), 110–116. pages 7, 9

[99] Sari, R., and Piran, T. Variability in Gamma-Ray Bursts: A Clue. *485* (Aug. 1997), 270. pages 7, 12

[100] Sari, R., Piran, T., and Halpern, J. P. Jets in Gamma-Ray Bursts. *519* (July 1999), L17–L20. pages 80

[101] Sari, R., Piran, T., and Narayan, R. Spectra and Light Curves of Gamma-Ray Burst Afterglows. *497* (Apr. 1998), L17. pages 32, 107, 110

[102] Schmidt, W. K. H. Distance limit for a class of model gamma-ray burst sources. *271* (Feb. 1978), 525–527. pages 9

[103] Sedov, L. I. Propagation of strong shock waves. *J. Appl. Math. Mech. 10* (1948), 241–250. pages 20

[104] Shemi, A., and Piran, T. The appearance of cosmic fireballs. *365* (Dec. 1990), L55–L58. pages 9

[105] Soffitta, P., Feroci, M., Piro, L., in 't Zand, J., Heise, J., di Ciolo, L., Muller, J. M., Palazzi, E., and Frontera, F. GRB 980425. *6884* (Apr. 1998), 1. pages 3

[106] Spruit, H. C. Dynamo action by differential rotation in a stably stratified stellar interior. *381* (Jan. 2002), 923–932. pages 83

[107] Stanek, K. Z., Dai, X., Prieto, J. L., An, D., Garnavich, P. M., Calkins, M. L., Serven, J., Worthey, G., Hao, H., Dobrzycki, A., Howk, C., and Matheson, T. "Anomalous" Optical Gamma-Ray Burst Afterglows Are Common: Two z ˜ 4 Bursts, GRB 060206 and GRB 060210. *654* (Jan. 2007), L21–L24. pages 32, 49, 60

[108] Stanek, K. Z., Matheson, T., Garnavich, P. M., Martini, P., Berlind, P., Caldwell, N., Challis, P., Brown, W. R., Schild, R., Krisciunas, K., Calkins, M. L., Lee, J. C., Hathi, N., Jansen, R. A., Windhorst, R., Echevarria, L., Eisenstein, D. J., Pindor, B., Olszewski, E. W., Harding, P., Holland, S. T., and Bersier, D. Spectroscopic Discovery of the Supernova 2003dh Associated with GRB 030329. *591* (July 2003), L17–L20. pages 3

[109] Stone, J. M., Gardiner, T. A., Teuben, P., Hawley, J. F., and Simon, J. B. Athena: A New Code for Astrophysical MHD. *178* (Sept. 2008), 137–177. pages 26

[110] Taylor, G. The Formation of a Blast Wave by a Very Intense Explosion. I. Theoretical Discussion. *Royal Society of London Proceedings Series A 201* (Mar. 1950), 159–174. pages 20

[111] Thompson, C. A Model of Gamma-Ray Bursts. *270* (Oct. 1994), 480. pages 7

[112] Tinney, C., Stathakis, R., Cannon, R., Galama, T., Wieringa, M., Frail, D. A., Kulkarni, S. R., Higdon, J. L., Wark, R., Bloom, J. S., and Bepposax GRB Team. GRB 980425. *6896* (May 1998), 3. pages 3

[113] Tóth, G., and Odstrcil, D. Comparison of Some Flux Corrected Transport and Total Variation Diminishing Numerical Schemes for Hydrodynamic and Magnetohydrodynamic Problems. *Journal of Computational Physics 128* (Oct. 1996), 82–100. pages 82

[114] Usov, V. V. Millisecond pulsars with extremely strong magnetic fields as a cosmological source of gamma-ray bursts. *357* (June 1992), 472–474. pages 10

[115] van Eerten, H. J., Leventis, K., Meliani, Z., Wijers, R. A. M. J., and Keppens, R. Gamma-ray burst afterglows from transrelativistic blast wave simulations. *403* (Mar. 2010), 300–316. pages 26, 43, 45

[116] van Eerten, H. J., Meliani, Z., Wijers, R. A. M. J., and Keppens, R. No visible optical variability from a relativistic blast wave encountering a wind termination shock. *398* (Sept. 2009), L63–L67. pages 32, 80

[117] van Eerten, H. J., Meliani, Z., Wijers, R. A. M. J., and Keppens, R. Jet simulations and gamma-ray burst afterglow jet breaks. *410* (Jan. 2011), 2016–2024. pages 46, 52, 95

[118] van Eerten, H. J., and Wijers, R. A. M. J. Gamma-ray burst afterglow scaling coefficients for general density profiles. *394* (Apr. 2009), 2164–2174. pages 26, 33, 43, 45, 94, 95

[119] van Marle, A. J., Langer, N., and García-Segura, G. Constraints on gamma-ray burst and supernova progenitors through circumstellar absorption lines. *444* (Dec. 2005), 837–847. pages 82

[120] van Marle, A. J., Langer, N., Yoon, S.-C., and García-Segura, G. The circumstellar medium around a rapidly rotating, chemically homogeneously evolving, possible gamma-ray burst progenitor. *478* (Feb. 2008), 769–778. pages 82, 86

[121] Vishniac, E. T. The dynamic and gravitational instabilities of spherical shocks. *274* (Nov. 1983), 152–167. pages 100

[122] Vlahakis, N., and Königl, A. Relativistic Magnetohydrodynamics with Application to Gamma-Ray Burst Outflows. I. Theory and Semianalytic Trans-Alfvénic Solutions. *596* (Oct. 2003), 1080–1103. pages 10

[123] Vlahakis, N., and Königl, A. Relativistic Magnetohydrodynamics with Application to Gamma-Ray Burst Outflows. II. Semianalytic Super-Alfvénic Solutions. *596* (Oct. 2003), 1104–1112. pages 10

[124] Vlasis, A., van Eerten, H. J., Meliani, Z., and Keppens, R. Two-shell collisions in the gamma-ray burst afterglow phase. *415* (July 2011), 279–291. pages 60, 63, 76, 79, 80, 92, 94, 97, 101

[125] von Zeipel, H. The radiative equilibrium of a rotating system of gaseous masses. *84* (June 1924), 665–683. pages 84

[126] Wang, X., and Loeb, A. Variability of Gamma-Ray Burst Afterglows due to Interstellar Turbulence. *535* (June 2000), 788–797. pages 32

[127] Weibel, E. S. Spontaneously Growing Transverse Waves in a Plasma Due to an Anisotropic Velocity Distribution. *Physical Review Letters 2* (Feb. 1959), 83–84. pages 43

[128] Wijers, R. A. M. J., and Galama, T. J. Physical Parameters of GRB 970508 and GRB 971214 from Their Afterglow Synchrotron Emission. *523* (Sept. 1999), 177–186. pages 6

[129] Wijers, R. A. M. J., Rees, M. J., and Meszaros, P. Shocked by GRB 970228: the afterglow of a cosmological fireball. *288* (July 1997), L51–L56. pages 12

[130] Woosley, S. E. Gamma-ray bursts from stellar mass accretion disks around black holes. *405* (Mar. 1993), 273–277. pages 32, 60, 83

[131] Woosley, S. E., and Bloom, J. S. The Supernova Gamma-Ray Burst Connection. *44* (Sept. 2006), 507–556. pages 32

[132] Woosley, S. E., and Heger, A. The Progenitor Stars of Gamma-Ray Bursts. *637* (Feb. 2006), 914–921. pages 82

[133] Woźniak, P. R., Vestrand, W. T., Wren, J. A., White, R. R., Evans, S. M., and Casperson, D. RAPTOR Observations of Delayed Explosive Activity in the High-Redshift Gamma-Ray Burst GRB 060206. *642* (May 2006), L99–L102. pages 49

[134] Wygoda, N., Waxman, E., and Frail, D. A. Relativistic Jet Dynamics and Calorimetry of Gamma-ray Bursts. *738* (Sept. 2011), L23. pages 30, 60, 80

[135] Yoon, S.-C., and Langer, N. Evolution of rapidly rotating metal-poor massive stars towards gamma-ray bursts. *443* (Nov. 2005), 643–648. pages 83

[136] Yoon, S.-C., and Langer, N. On the evolution of rapidly rotating massive white dwarfs towards supernovae or collapses. *435* (June 2005), 967–985. pages 82

[137] Yoon, S.-C., Langer, N., and Norman, C. Single star progenitors of long gamma-ray bursts. I. Model grids and redshift dependent GRB rate. *460* (Dec. 2006), 199–208. pages 6, 82, 83

[138] Zhang, B. Gamma-Ray Bursts in the Swift Era. *7* (Feb. 2007), 1–50. pages 4, 32

[139] Zhang, B., Fan, Y. Z., Dyks, J., Kobayashi, S., Mészáros, P., Burrows, D. N., Nousek, J. A., and Gehrels, N. Physical Processes Shaping Gamma-Ray Burst X-Ray Afterglow Light Curves: Theoretical Implications from the Swift X-Ray Telescope Observations. *642* (May 2006), 354–370. pages xii, 17, 32

[140] Zhang, B., and Mészáros, P. Gamma-Ray Bursts: progress, problems prospects. *International Journal of Modern Physics A 19* (2004), 2385–2472. pages 32

[141] Zhang, B., Zhang, B.-B., Liang, E.-W., Gehrels, N., Burrows, D. N., and Mészáros, P. Making a Short Gamma-Ray Burst from a Long One: Implications for the Nature of GRB 060614. *655* (Jan. 2007), L25–L28. pages 5

[142] Zhang, W., and MacFadyen, A. The Dynamics and Afterglow Radiation of Gamma-Ray Bursts. I. Constant Density Medium. *698* (June 2009), 1261–1272. pages 19, 33, 37, 60, 74, 80

[143] Zhang, W., and MacFadyen, A. I. RAM: A Relativistic Adaptive Mesh Refinement Hydrodynamics Code. *164* (May 2006), 255–279. pages 26, 30

Curriculum vitae

Alkiviadis Vlasis

Celestijnenlaan 200B
Department of Mathematics
KU Leuven
3001 Leuven, Belgium

Voice: 0494483424
E-mail: Alkis.Vlasis@wis.kuleuven.be

Research interests

Computational fluid dynamics, relativistic phenomena, Magnetohydrodynamics, astrophysical jets, gamma-ray bursts, stellar environment simulations, radiative processes in high energy astrophysics etc.

Education

Graduate Student **November, 2008 - present**
Includes current Ph.D. research, Ph.D. level coursework and supervising/assisting bachelor and master student courses/examinations in KU Leuven, Belgium. Thesis title: Numerical simulations in the afterglow phase of GRBs.

Master Student **September, 2005 - June 2008**
Master in Astronomy Astrophysics and Mechanics in the Physics department of the National and Kapodistrian University of Athens. Master thesis title: Numerical simulations of Young Stellar Objects using the cide PLUTO

Undergraduate Student **September, 2000 - September 2005**
Bachelor student in the Physics department of the National and Kapodistrian University of Athens. Thesis title: Relativistic MHD: the flow velocity as a function of the geometry of the magnetic field.

Publications

Z. Meliani, A. Vlasis, R. Keppens. Numerical simulations of Flares in GRB Afterglow Phase. Proceedings of the 6th international conference held at Valencia, Spain June 13-17, 2011. ASP Conference Series, Vol. 459, p.118

R. Keppens, Z. Meliani, A.J. van Marle, P. Delmont, A. Vlasis, B. van der Holst. Parallel, grid-adaptive approaches for relativistic hydro and magnetohydrodynamics. 2012, Journal of Computational Physics, Volume 231, Issue 3, p. 718-744.

A. Vlasis, Z. Meliani, R. Keppens. Late activity in GRB afterglows. A multidimensional approach. 2012, Memorie della Societa Astronomica Italiana Supplement, v.21, p.190

A. Vlasis, H.J. van Eerten, Z. Meliani, R. Keppens. Two-shell collisions in the gamma-ray burst afterglow phase. 2011, Monthly Notices of the Royal Astronomical Society (MNRAS), Volume 415, Issue 1, pp. 279-291.

A. Vlasis, H.J. van Eerten, Z. Meliani, R. Keppens. Two shell collisions in the GRB afterglow phase. 2011, Memorie della Societa Astronomica Italiana, v.82, p.137

Papers in preparation

A. Vlasis, Z. Meliani, R. Keppens. On the external shock refreshment mechanism of the GRB afterglow phase. *Submitted for publication in MNRAS.*

Additional training and courses

October-December 2010

Participation with evaluation in course series organized specifically for doctoral students. Course title: Introduction to multiscale modelling and simulation Positive evaluation.

13-24 July 2009

Workshop in Computational Astrophysics, "Prospects in Theoretical Physics 2009: Computational Astrophysics". Institute for Advanced Studies (IAS), Princeton, USA.

Conference presentations

April 7-8, 2010 - Bonn, Germany

Steady jets and transient jets. Poster and oral presentation: Two-shell collisions

in the GRB afterglow phase.

May 19-21, 2010 - Nijmegen, The Netherlands
NAC astrophysical conference. Poster presentation: Two-shell collisions in the GRB afterglow phase.

May 16-20, 2011 - Como, Italy
GRBs as probes: from the progenitor's environment to the high redshift Universe. Poster presentation: Multidimensional simulations of energy injection in the afterglow phase of GRBs.

November 2-4, 2011 - Manchester UK
COST meeting, Black holes in a violent Universe. Oral presentation: A multidimensional numerical approach on energy injection in GRB afterglows.

May 7-11, 2012 - Munich Germany
Fermi/Swift Gamma Ray Bursts 2012 Conference. Oral presentation: Multidimensional numerical simulations in the afterglow phase.

Arenberg Doctoral School of Science, Engineering & Technology
Faculty of Science
Department of Mathematics
Centre for mathematical Plasma Astrophysics
Celestijnenlaan 200B box 2400
B-3001 Heverlee

KATHOLIEKE UNIVERSITEIT LEUVEN

ASSOCIATIE K.U.LEUVEN